Electrochemical Reduction of Carbon Dioxide: Product Analysis and Cell Design

Dhruv Trivedi

This dissertation is submitted for the degree of Doctor of Philosophy

December 2021

Department of Chemistry

I dedicate this thesis to my mum, Rohini Trivedi. Your love and support goes unparalleled. I know you are smiling at me from up there.

Rest in peace, I love you forever.

20th November 1956 – 6th May 2021

“What manner of thing is happening here?!”

– Jeremy Clarkson, often quoted during this work.

Declaration

This thesis has not been submitted in support of an application for another degree at this or any other university. It is the result of my own work and includes nothing that is the outcome of work done in collaboration except where specifically indicated. Many of the ideas in this thesis were the product of discussion with my supervisor Dr Kathryn Toghill.

Chapter 4 of this thesis has been published in the following academic publication.

[1] Trivedi, D., Crosse, J., Tanti, J., Cass, A.J. and Toghill, K.E., 2018. The electrochemical determination of formaldehyde in aqueous media using nickel modified electrodes. Sensors and Actuators B: Chemical, 270, pp.298-303.

Dhruv Trivedi

Lancaster University, UK

Abstract

It is now well known that CO_2 is one of the most significant greenhouse gasses causing global warming and detrimental climate changes. One of the 21st century's leading challenges is trying to reduce CO_2 emissions by finding methods to reduce, reuse, and recycle the gas. Making use of the otherwise waste product by conversion to valuable compounds may eventually create a circular process, allowing CO_2 emitting processes to run on their effluent gasses. Electrochemical conversion of CO_2 is a popular method to convert CO_2 to valuable products such as alcohols but is still to this day a very inefficient process. This thesis works towards and details challenges faced in enabling research at the Department of Chemistry, Lancaster University, towards electrochemical reduction of CO_2. Developments are made by setting up product analysis arrays for liquid products (Ion chromatography, NMR) and gaseous products (Gas chromatography, on-line electrochemical mass spectrometry). Cell designs are also conceptualised and optimised for user-friendly, adaptable analysis using different types of electrodes (solid metal and gas diffusion electrodes) and for combined analysis using on-line electrochemical mass spectrometry and on-line gas chromatography. Therefore, a foundation for future experimentation using exciting, new, efficient catalysts is achieved in this work.

Acknowledgements

First, I would like to thank my supervisor Dr Kathryn Toghill (Kass). I am fortunate to have worked with Dr Toghill from my BSc project in 2017, to the end of my PhD, which I am grateful for being offered. My knowledge of electrochemistry and analytical chemistry has grown dramatically since working with Dr Toghill. I can finish this thesis with invaluable knowledge to hopefully one day apply to the world of CO_2 reduction and create an impact. Being the first student in the department to undertake the electrochemical CO_2 reduction challenge, Dr Toghill ensured that I had access to equipment and was always there when help was needed. Resources, in the beginning, were limited, but I am thankful for the funding Dr Toghill obtained to further develop research by bringing in new resources and students. I would like to also thank you for all of the opportunities to attend conferences and workshops. Not every day can a student say that their supervisor was like a good friend; however, I am lucky enough to be able to say that. Kass, it was an absolute pleasure to work with you and help pioneer the development of CO_2 research at Lancaster University.

I would like to extend my gratitude to members of the Toghill group past and present; Dr Behnam Bastani, Dr Craig Armstrong, Dr Declan Bryans, and Dr Ross Hogue. Thank you all for the guidance and wisdom you were able to impart to me. I would also like to thank Beth Murdock and all other members of the group.

Outside of the group, I would like to thank Professor Peter Fielden, Professor Harry Hoster, Dr John Hardy, Dr Nuno Bimbo and Dr Mathias Kjærgård Christensen for their help during the PhD. Thank you, Professor Hoster, for taking me under your wing during Dr Toghill's maternity leave. Thank you, Dr Hardy, for all of your wisdom and support.

I would like to thank my girlfriend, Amee Tanna, for her support and love. You always know the right things to say and have guided me through dark times to bring light back into my life. This gratitude extends to the Tanna Family for their support.

I would like to especially thank Dr Niklas Shahin Nikman for all of his help during this PhD and for becoming an older brother to me. I extend this gratitude to Dr Rob Burrell, Sophie Au-Yong, Dr Cindy Soares and Saruta 'Safe' Deeprasert for keeping me sane.

Finally, thank you to my family for always supporting my work, no matter how hard times have gotten.

Thank you to the Department of Chemistry, Department of Physics and Department of Engineering at Lancaster University and the funding bodies for this work.

Thank you for reading.

Contents

1 INTRODUCTION 1
1.1 Current Issues 1
1.2 Methods to reduce CO_2 2
1.2.1 Capturing CO_2 3
1.2.2 Converting CO_2 3
1.3 Electrochemical Reduction of CO_2 7
1.3.1 Background 7
1.3.2 Metal Catalysts previously studied 8
1.3.3 Cu for ECO_2RR 9
1.4 Challenges Summary 11
1.5 Thesis objectives and overview 13

2 ELECTROCHEMICAL THEORY 14
2.1 Introduction 14
2.2 Electrode Potential 15
2.2.1 Standard potentials 15
2.2.2 Practical Reference Electrodes 17
2.3 Thermodynamics 18
2.3.1 Chemical and Electrochemical Potential 18
2.3.2 The Nernst Equation 20
2.3.3 Thermodynamics for CO_2RR 21
2.4 Dynamic electrochemistry 23
2.4.1 Mass Transport 24
2.4.2 Electrochemical Kinetics 26
2.4.3 Kinetics of CO_2RR 33
2.5 Principles of electrochemical methods 35
2.5.1 Cyclic Voltammetry 35
2.5.2 Linear Sweep Voltammetry 37
2.5.3 Chronopotentiometry and Chronoamperometry 38
2.6 Electrochemical reactor cells 38
2.6.1 Introduction 38
2.6.2 Three-Electrode Cell 39
2.6.3 Bulk electrolysis cells: The H-cell 40
2.6.4 Flow Cell 42
2.7 Summary 45

3 ECO_2RR PRODUCT ANALYSIS 46
3.1 Introduction to Product analysis 46
3.2 Product analysis methods 48
3.2.1 Gas Chromatography (GC) 48
3.2.2 High Performance Liquid Chromatography (HPLC) 53
3.2.3 Ion Chromatography (IC) 54
3.2.4 Nuclear Magnetic Resonance (NMR) 54
3.3 Analysis methods developed 55
3.3.1 Standard Solutions 55
3.3.2 Ion Chromatography 56
3.3.3 NMR 57
3.3.4 Gas Chromatography with BID detector (GC-BID) 59
3.4 Conclusions 64

4 ELECTROCHEMICAL FORMALDEHYDE DETERMINATION 65
4.1 Introduction 65
4.2 Experimental 67
4.2.1 Reagents and Equipment 67
4.2.2 Electrochemical Method 68
4.2.3 Spectrophotometric method 70
4.3 Results and discussion 71
4.3.1 Electrochemical determination 71
4.3.2 Spectrophotometric determination 76
4.3.3 Comparison of both methods with a real-world sample. 78
4.4 Conclusions 82

5 ADAPTABLE DUAL STAGE FLOW CELL WITH ON-LINE ELECTROCHEMICAL MASS SPECTROMETRY (OLEMS) 83
5.1 Introduction 83
5.2 Principles of Operation 84
5.3 Instrumentation and Experimental 87
5.3.1 DEMS Equipment 87
5.3.2 Mass Spectrometry and Product Detection 88
5.3.3 DEMS Calibration 88
5.4 Commercial DEMS Cell 92
5.4.1 Electrochemistry 94
5.5 Results 95
5.5.1 CO_2 Reduction on Copper Electrode 95
5.5.2 DEMS Cell setbacks 99
5.6 Adaptable Flow Cell (AFC) 103
5.6.1 Introduction and Development 103
5.6.2 Dual Stage Flow Cell OLEMS 110
5.6.3 CO_2 Electrolysis Results – Dual Stage Flow Cell Design 113
5.6.4 Discussion on the effectiveness of the Dual Stage Flow Cell 114
5.7 Membrane Inlet MS Probe concept 115
5.8 Conclusions 120

6 CONCLUSIONS 121
6.1 Summary 121
6.2 Retrospectives and Future Work 122

7 REFERENCES 125

8 APPENDICES 134

List of Tables

Table 1.3.1 Metal catalysts studied by Hori *et al.* for the electrochemical reduction of CO_2. Electrode potentials and faradaic efficiencies were reported for each metal.[41-43] 9

Table 2.2.1 Reference electrode potentials *vs.* SHE. [55, 56] 18

Table 2.4.1 - Faradaic Efficiencies of Electrochemical CO_2RR using a Cu electrode. Galvanostatic at 5 $mAcm^{-2}$ at 19°C. [43] 34

Table 3.1.1 - Products which can be formed during the electrochemical reduction of CO_2. [4, 38, 39, 47, 90, 91] 47

Table 4.3.1 - Errors associated with formaldehyde determination (* w.r.t limit of detection). 80

Table 5.5.1 - Faradaic efficiency comparison between Commercial DEMS Cell and Flow Cell. Experiments conducted on both with similar conditions. 98

Table 6.2.1 Ion Chromatography limit of detection at the lower concentration range. 136

Table 6.2.2 - D1 and NS values tested for NMR..... 140

Table 6.2.3 - GC-BID Parameters 142

Table 6.2.4 - Anycubic Photon Resin Printer Settings 143

List of Figures

Figure 1.3.1 – Plausible reaction pathways from adsorbed *CO on Cu for C_1/C_2 products. Green base or box shows major C_2 products. Reproduced from Zhao *et al.* [48] 10

Figure 1.3.2 – Plausible reaction pathway from adsorbed *CO on Cu. Blue base or box to show trace C_2 product formation. Reproduced from Zhao *et al.* [48] 11

Figure 1.3.3 - Plausible reaction pathway from adsorbed *CO on Cu. Yellow base to show minor C_2 products. Reproduced from Zhao *et al.* [48] 11

Figure 2.3.1 – A proposed mechanism for the electrochemical reduction of CO_2 using a copper catalyst in methanol.[57] 22

Figure 2.3.2: Accepted mechanism for electrochemical reduction of CO_2 in aqueous electrolytes. xH represents proton-providing substances.[4] 22

Figure 2.4.1 - Current - Overpotential curves as a representation of the derived Butler-Volmer Equation, with an example system. [54] 29

Figure 2.4.2 - Example Tafel plot to show the anodic and cathodic branches of a current-overpotential curve. [54] 32

Figure 2.5.1 - Typical reversible cyclic voltammogram. Arrows show direction of potential sweep (Left). Potential scheme as a function of time for cyclic voltammogram (right).[4, 54, 59] 36

Figure 2.5.2 - Typical Linear Sweep Voltammogram (left), Potential scheme as a function of time (right).[4, 54, 59] 37

Figure 2.6.1 - Conventional three-electrode cell with a Pt anode, VC cathode and Ag/AgCl reference electrode as an example..... 40

Figure 2.6.2 - Conventional H-Cell setup 41

Figure 2.6.3 - Glass H-cell used for preliminary experiments for ECO_2RR. 42

Figure 2.6.4 - Typical electrochemical flow cell cross section. Red shows anodic electrolyte flow, blue shows cathodic electrolyte flow. Both flows are separated by a PEM. 43

Figure 2.6.5 - Gas-phase flow system. 44

Figure 3.3.1 – Calibration set up diagram for GC-BID. CO_2 and Calibration Gas (CG) cylinders feed into sampling vessel (1), then the mixture is fed to the GC 6 port valve (2) where it fills the 500 μL sample loop (3), before being injected to the main column (4) and being detected by the BID (5). 60

Figure 3.3.2 – Pressure vessel 61

Figure 3.3.3 - Plasma inside BID, window open for inspection. 62

Figure 3.3.4 - Calibration plots obtained for GC-BID. (a) Hydrogen R^2 = 0.993, (b) Carbon monoxide R^2 = 0.998, (c) Methane R^2 = 0.997, (d) Ethylene R^2 = 0.998... 62

Figure 4.2.1 - Ni plated GC (high deposition time)..... 68

Figure 4.2.2 - Formaldehyde detection n=3 data for calibration over linear range of 0.1 to 1 mM. 69

Figure 4.2.3 - Formaldehyde detection n=3 data for calibration over linear range of 0.01 to 0.1 mM 70

Figure 4.3.1 - Conditioning of a nickel modified glassy carbon electrode for 250 scans in 1 M KOH following 60 s deposition of nickel. Scan Rate: 0.2 V/s. Every 30th scan shown..... 71

Figure 4.3.2 - Six consecutive additions of 0.5 mM HCHO to a 10 mL 1 M KOH solution. Scan Rate: 0.2 V/s; Electrode: Ni-GC – 60 s. 72

Figure 4.3.3 - Standard additions of formaldehyde under chronoamperometric conditions, using the Ni-GC electrode under constant, fast stirring. a) Additions of 0.1 mM formaldehyde with the calibration plot alongside. b) Additions of 0.01 mM formaldehyde with corresponding calibration plot alongside. 73

Figure 4.3.4 - Standard additions of formaldehyde under chronoamperometric conditions, using the Ni-GC electrode under constant, fast stirring. Addition of 'unknown' concentration sample of formaldehyde in Milli-Q, followed by three additions of 0.05 mM formaldehyde in Milli-Q water. Modulus of the x-intercept indicates the 'unknown' concentration. 74

Figure 4.3.5 - The catalytic response of the Ni-GC electrode in 1 M KOH to additions of 0.01 mM formaldehyde at 100, 150 and 200 s, followed by additions of methanol and formic acid. 1–methanol 0.01 mM; 2–formic acid 0.01 mM; 3–methanol 0.1 mM; 4–formic acid 0.1 mM; 5–formaldehyde 0.1 mM. 75

Figure 4.3.6 - UV/vis calibration data for the DDL derivatized formaldehyde where n = 3. 77

Figure 4.3.7 - Standard additions of formaldehyde under chronoamperometric conditions, using the Ni-GC electrode under constant, fast stirring. Addition of 'unknown' concentration sample of formaldehyde spiked pond water, followed by three additions of 0.05 mM formaldehyde in Milli-Q® ultrapure water. 79

Figure 5.2.1 - Basic representation of DEMS system..... 85

Figure 5.3.1 - Hiden HPR-40 DEMS system diagram - Image property of Hiden Analytical Ltd. 87

Figure 5.3.2 - MS Calibration plot obtained for hydrogen (m/z = 2). Integrated area of signal response plotted against calculated molarity of gas flowed into the cell over 10 minutes. R^2 = 0.966 90

Figure 5.3.3 - MS Calibration plot obtained for methane (m/z = 15). Integrated area of signal response plotted against calculated molarity of gas flowed into the cell over 10 minutes. $R^2 = 0.936$ 90

Figure 5.3.4 - MS Calibration plot obtained for ethylene (m/z = 26). Integrated area of signal response plotted against calculated molarity of gas flowed into the cell over 10 minutes. $R^2 = 0.993$ 91

Figure 5.3.5 - MS Calibration plot obtained for CO (m/z = 28). Integrated area of signal response plotted against calculated molarity of gas flowed into the cell over 10 minutes. $R^2 = 0.967$ 91

Figure 5.4.1 - Cathodic electrolyte flow diagram. CO_2 sparged electrolyte enters cell (orange) and radially passes over ring electrode. Products (blue) are carried down to the pervaporation chamber, where products can pass the PTFE membrane to DEMS (yellow dashed). The electrolyte then exits the cell (green). 92

Figure 5.4.2 - 3D rendering of cell 93

Figure 5.4.3 - Cross-section of DEMS cell 93

Figure 5.5.1 - MS-LSV overlay of methane and ethylene formed during CO_2 reduction using Commercial DEMS cell. Copper ring working electrode, Pt mesh counter electrode, ‘leak-free’ μ-Ag/AgCl reference electrode, LSV from 0 V to -1.8 V vs Ag/AgCl, 0.2 mVs^{-1} 97

Figure 5.5.2 - Comparison of 'leak-free' μAg/AgCl (left 1 mm O.D., middle 1.6 mm O.D. Innovative Instruments Inc., USA) with conventional, standard Ag/AgCl electrode (right, IJ Cambria, UK). Major difference in size allows flexibility of design with ‘leak-free’ electrodes, but promised longevity was not met for these experiments. 99

Figure 5.5.3 - Copper ring working electrode, post-analysis corrosion. 100

Figure 5.5.4 - Flow through retaining screw size 4 mm. 101

Figure 5.5.5 - Copper ring electrode inside cell, held in place with screw. Wear and ‘rounding’ of the screw can be seen, making it considerably difficult to remove. 101

Figure 5.5.6 - Recess for copper ring working electrode, with copper connecting rod visible. The position of the connecting rod is due to spring underneath. Careful positioning and pressure would need to be applied while electrode is screwed in to ensure connecting rod spring is fully pressed, therefore completing the connection. Connecting rod made from piece of copper wire, size determined through trial and error. 102

Figure 5.6.1 - FDM-3D Printed initial cell concept to observe ease of assembly and scale. Cell body, spacer and current collectors all printed in ABS 104

Figure 5.6.2 - 'Exploded' CAD view of cell and components. 104

Figure 5.6.3 – AFC Plan layout. Top row left to right: Cell body, Spacer, Cell Body. Middle row: Flow-through current collector for Pt Mesh, Pt Mesh, Nafion-115 Membrane, Cu Plate, Current collector for Cu Plate. Lowest row: Gaskets and NPT tube fittings. 105

Figure 5.6.4 – Serpentine flow field current collector (left) to provide even distribution of gas to the GDE. Flow-through flow field current collector (centre) for comparison, used for electrolyte flow through Pt mesh. Dimensions of current collector (right). 106

Figure 5.6.5 – AFC with all ports in use for GDE setup. Ports to the left used for anodic electrolyte flow, ports in spacer for cathodic electrolyte flow, ports to the right for CO_2 flow to GDE. 107

Figure 5.6.6 - Assembled flow cell dimensions. All measurements are in millimetres. 107

Figure 5.6.7 - Spacer dimensions inc. chamber (18.6 x 15 x 12.32 mm, internal volume 3.44 cm^3)..... 108

Figure 5.6.8 - EIS of AFC in standard flow cell configuration. WE =Cu plate, CE = Pt mesh, RE = Ag/AgCl. 0.1 M $KHCO_3$ electrolyte flowing at 1 mL/min. Ohmic resistance around 54.5 Ω. 109

Figure 5.6.9 – Simplified diagram to show set up used for electrochemical reduction of CO_2 using flow cell and bridge interface. Blue line signifies CO_2 sparged $KHCO_3$ anodic electrolyte flow, yellow line signifies CO_2 sparged $KHCO_3$ cathodic electrolyte flow, both at 1 ml/min, negative system regulated by syringe pump. Electrolyte reservoir above cell to deliver electrolyte through gravity feed. Cathodic flow through spacer, interacting with Cu working electrode (WE), then out with products to interface bridge for DEMS before being collected into syringe. Anodic flow through flow field and Pt mesh (CE), then directly to syringe pump. Connections to potentiostat not shown in figure..... 110

Figure 5.6.10 – 'Hiden Single thin layer DEMS Type A-cell' adapted for use as a microfluidic bridge (and pervaporation chamber) to interface the flow cell with the MS inlet. Inside of bridge (middle) shows metal frit MS inlet and sealing gasket. Inside of bridge (right) shows the small chamber for electrolyte flow through and PTFE membrane interface atop the metal frit. Chamber volume 5.5 μL. [147] 111

Figure 5.6.11 - Bridge placed at MS inlet. Cathodic electrolyte inflow pipes attached. 112

Figure 5.6.12 - MS-LSV overlay of methane (A) and ethylene (B) formed during CO_2 reduction using the flow cell method. Copper plate working electrode, Pt mesh counter electrode, Ag/AgCl reference electrode, LSV from 0V to 1.8V vs Ag/AgCl, 0.2 mVs^{-1} 113

Figure 5.7.1 – Conceptual drawing of probe being held in specially designed spacer. Electrolyte flow (blue) exits via the probe interface, allowing dissolved and evolved gasses (orange) to be collected. 116

Figure 5.7.2 – MIMS probe Flow cell layout. Top row left to right: Cell body, Spacer with MIMS Screw-in probe, Cell Body. Middle row: Flow-through current collector for Pt Mesh, Pt Mesh, Nafion-115 Membrane, Cu Plate, Current collector for Cu Plate. Lowest row: Gaskets and NPT tube fittings. 117

Figure 5.7.3 - Overlaid Mass Spectra-Cyclic Voltammogram (MS-CV) to show response of hydrogen during cyclic voltammetry from 0 to -2.3 V (*vs.* Ag/AgCl). Scan rate 0.0025 V/s, 3 scans, average taken. Cu working electrode, Pt Mesh counter electrode, Ag/AgCl reference electrode. CO_2 saturated 0.1M $KHCO_3$ electrolyte, flowing at 1 mL/min. 119

Figure 6.2.1 Ion Chromatography results of the mixed solution after the ramping method was applied 135

Figure 6.2.2 - Overlaid results of 0 to 10 ppm solutions of acetic, formic and oxalic acid (increments of 2 ppm) (a) and the corresponding calibration plots for (b) formic acid (c) acetic acid (d) oxalic acid 136

Figure 6.2.3 – Overlaid Ion Chromatography results of 20 to 100 ppm solutions of acetic, formic and oxalic acid (increments of 20 ppm) (a) and the corresponding calibration plots for (b) formic acid (c) acetic acid (d) oxalic acid 137

Figure 6.2.4 - Full Range IC calibration plots for all acids. 138

Figure 6.2.5 H^1NMR (H_2O + D_2O 90:10, 400MHz): δ 8.24 (1. formic acid / formaldehyde), δ 4.70 (2. methanol / $KHCO_3$ -OH), δ 3.28 (3. formaldehyde), δ 3.26 (4. methanol), δ 2.62 (5. DMSO), δ 1.98 (6. acetic acid). 139

Figure 6.2.6 Methanol peak with interfering formaldehyde peak 139

Figure 6.2.7 Error due to NS - incomplete cycle 141

List of Abbreviations and Acronyms

Acronym / Abbreviation	Definition
%FE	Faradaic Efficiency (%)
ABS	Acrylonitrile Butadiene Styrene
AFC	Adaptable Flow Cell
Ag/AgCl	Silver/Silver-Chloride (reference electrode)
BECCS	Bio-energy with Carbon Capture and Storage
BID	Barrier Discharge Ionisation Detector (Gas Chromatography)
CA	Chronoamperometry
CDR	Carbon Dioxide Reduction (non-chemical definition)
CE	Counter Electrode
CNC	Computer Numerical Control (manufacturing)
CV	Cyclic Voltammetry
DDL	Diacetyldihydrolutidine
DEMS	Differential Electrochemical Mass Spectrometry
DLP	Digital Light Processing
DPV	Differential Pulsed Voltammetry
ECO_2R	Electrochemical Carbon Dioxide Reduction
ECO_2RR	Electrochemical Carbon Dioxide Reduction Reaction
EPDM	Ethylene-propylene diene monomer
EtOH	Ethanol
FC	Flow Cell
FDM	Fused Deposition Modelling
FID	Flame Ionisation Detector (Gas Chromatography)
GC	Gas Chromatography
GC-BID	Gas Chromatography with Barrier Discharge Ionisation Detector
GC-MS	Gas Chromatography with Mass Spectrometry
GDE	Gas Diffusion Electrode
GDL	Gas Diffusion Layer
GT	Gas Tight
HER	Hydrogen Evolution Reaction
HPLC	High Performance Liquid Chromatography
HV-AC	High Voltage Alternating Current
IC	Ion Chromatography
ICP-OES	Inductively Coupled Plasma – Optical Emission Spectrometry

LOD	Limit of Detection
LSV	Linear Sweep Voltammetry
MS-CV	Mass Spectra – Cyclic Voltammogram overlay
MS-LSV	Mass Spectra – Linear Sweep Voltammogram overlay
Ni-GC	Nickel Modified Glassy Carbon
NMR	Nuclear Magnetic Resonance Spectroscopy
NP	Nanoparticle
OCP	Open Circuit Potential
OER	Oxygen Evolution Reaction
OLEMS	On-Line Electrochemical Mass Spectrometry
PEM	Polymer Electrolyte Membrane
PEMFC	Proton Exchange Membrane Flow Cell
PP	Polypropylene
QMS	Quadrupole Mass Spectrometer
RE	Reference Electrode
RHE	Reversible Hydrogen Electrode (reporting standard)
SEM	Secondary Electron Multiplier (DEMS Detector)
SLA	Stereolithography
TCD	Thermal Conductivity Detector (Gas chromatography)
TIC	Total Ion Chromatogram
US EPA	United States Environmental Protection Agency
UV	Ultraviolet
VC	Vitreous Carbon
WE	Working Electrode

List of Appendices

Appendix A: Analysis Methods 135

Appendix B: Cell Design 143

1 Introduction

1.1 Current Issues

The use of fossil fuels such as oil, coal, and natural gas has resulted in some of the most prosperous years, aiding significant human advancement and development eras. Due to this, the world has become very heavily reliant on fossil fuels. They are not only used to produce energy but have also become essential in many manufacturing processes. Nevertheless, fossil fuels come at an environmental price as a resultant product, carbon dioxide (CO_2), a significant contributor to greenhouse gasses. [1-3]

CO_2 is the most common greenhouse gas on the planet. While it is an essential atmospheric gas that plays a crucial role in the growth of plants, facilitating wildlife and biosystems, the balance of CO_2 in the atmosphere has been significantly altered by those prosperous industrial activities resulting in present-day global warming.[4]

CO_2 is produced from both natural sources (such as the ocean, [5] volcanic activity [6] and soils [7]) and anthropogenic sources (such as aviation, [8] sea [9] and terrestrial [10] transport, and industries such as cement production). [11] Annually, around 35 gigatons of CO_2 is produced just through the usage and combustion of fossil fuels. [12]

Due to anthropogenic CO_2 emissions, data from the 'Earth System Research Laboratory' shows that average CO_2 levels in the atmosphere have risen to 412.35 ppm (parts per million) as of August 2021.[13] Since 2017, there has been a global rise in CO_2 by approximately 10 ppm, resulting in adverse effects with regards to (but not limited to) global warming, climate change, sea levels, food production and biodiversity.[13] Current CO_2 levels are the highest they have been in millions of years, [4] and with the rise in emissions, it is predicted to reach around 800 ppm by 2100 if no action is taken. [14-16] Therefore, it is imperative that methods to reduce anthropogenic CO_2 are implemented as soon as possible.

Over the past decade, there has been an increase in methods to reduce anthropogenic CO_2 emissions. One is switching to 'green energy' – essentially renewable energy sources (*e.g.* wind, solar and hydropower). These sources emit almost negligible amounts of CO_2 than the extraction, refining and combustion of fossil fuels. Other measures are also being taken by making buildings, towns, and cities more carbon-neutral and reducing the energy used. Large industries have also made efforts to reduce CO_2 emissions from their manufacturing processes.

The methods mentioned earlier are working to reduce CO_2 emissions; however, the key word is 'emissions'. What about the CO_2 that has already been *emitted*? The reduction of CO_2 produced, and the conversion of CO_2 already produced hand-in-hand can significantly impact the environment. The result will cause a plateau of CO_2 in the atmosphere and potentially may help decrease the levels from which it has risen to in the past decades. Developing and implementing methods to convert CO_2 to valuable materials is now necessary to protect the environment.

1.2 Methods to reduce CO_2

There are multitudes of methods to reduce atmospheric CO_2, known as carbon dioxide removal (CDR) methods. Examples include 'bio-energy with carbon capture and storage' (BECCS), enhanced weathering, biochar, [17] direct air capture, and ocean fertilisation. These can be said to 'recycle' the CO_2. However, two significant approaches consist of capture and global sequestration of CO_2 and converting the CO_2 to short-chain carbon fuels. The latter is desirable in this age of high fuel demand and dependence.

1.2.1 Capturing CO_2

CO_2 can be captured physically and chemically from fuel gas or flue gas. Capturing from fuel gas is known as 'pre-combustion capture' and is generally done to remove the CO_2 from hydrogen-CO_2 mixture gasses. The hydrogen, which results from this, is then supplied to facilitate power-generating devices such as fuel cells. CO_2 captured from flue gas is known as 'post-combustion' capture, which uses adsorbents (such as activated carbon, alumina, metallic oxides and zeolites) to adsorb the CO_2 physically. A third capture technique as an alternative to post-combustion capture is 'oxy-combustion capture', supplying pure oxygen instead of air for combustion. This results in flue gas streams rich with CO_2; however, due to the high costs associated with the process, it is considered almost impractical.[16, 18, 19]

1.2.2 Converting CO_2

There are many methods to convert CO_2; chemical, bio-chemical, enzymatic, photocatalytic and electrochemical. [20] With the current state of technology, the capture, conversion and utilization of CO_2 faces significant hindrances. These include the high costs associated with CO_2 (capture, separation, purification and transportation), the amount of energy required for chemical conversion, and the fact that there are limited investment incentives as the technologies are still in the early development phase. The challenges faced are significant; however, the capture, conversion and utilisation of CO_2 is being recognised more and more and can be said to be some of the most promising research in energy and environmental areas. Following are some examples of the conversion and reduction of CO_2.

1.2.2.1 Chemical Conversion

Examples of chemical processes in the chemical industry include producing salicylic acid from phenol (Eq. 1.2.1) and the synthesis of urea from ammonia and CO_2 (Eq. 1.2.2). Salicylic acid is then used to make Aspirin, and the urea can be used in various fertilisers as well as in making polymer materials. [20]

$$\mathbf{C_6H_5OH + CO_2 \rightarrow C_6H_5(OH)COOH} \qquad 1.2.1$$

$$\mathbf{2\,NH_3 + CO_2 \rightarrow H_2N - CO - NH_2 + H_2O} \qquad 1.2.2$$

Another example of the chemical conversion of CO_2 is methanol synthesis. Known as the CAMERE process (carbon dioxide hydrogenation to form methanol via reverse water-gas shift), stemming from the reverse of the water-gas shift reaction (RWGS). The water-gas shift reaction is the reaction of carbon monoxide and water vapour to produce carbon dioxide. The RGWS is carried out over zinc aluminate ($ZnAl_2O_4$), followed by the removal of water, and then methanol synthesis over $Cu/ZnO/Zr_2O/Ga_2O_3$. This process can produce around 75 megatonnes of methanol per year; however, there are drawbacks: this process requires two different reactors and catalysts. Research using $Cu/ZnO/Al_2O_3$ catalysts has been conducted to bring this to a singular catalyst and reactor process. $Cu/ZnO/Al_2O_3$ is the commercial catalyst for synthesising methanol from CO and hydrogen and shows promising performance; however, the conditions required for this performance include very high pressures (36 MPa for a 10:1 H_2:CO_2 ratio) therefore making the process rather economically challenging. [21]

A notable method of catalytic chemical conversion of gasses in syngas (CO, H_2) is the Fischer-Tropsch process. This process was conceived by Franz Fischer and Hans Tropsch in the 1920s and since then has been developed as a process to supply quantities of hydrocarbon fuels and chemicals.

$$(\mathbf{2n+1})\,\mathbf{H_2} + \mathbf{xCO} \rightarrow \boldsymbol{C_n}\mathbf{H_{(2n+2)}} + \mathbf{xH_2O} \qquad 1.2.3$$

Equation 1.2.3 - Represents the conversion of CO and H_2 to different hydrocarbons [22].

When n=1, the reaction is representative of the formation of methane, as an example. The conditions of a Fischer-Tropsch process are generally well-controlled to amplify the formation of higher value molecular weight hydrocarbons, especially those which can be used as liquid fuels. This process is able to deliver hydrocarbons from methane to paraffins. The catalysts used in this process are based on transition metals of iron, nickel, cobalt and ruthenium. Fischer-Tropsch, however, is dependent on hydrogen. This is a major drawback in the system as most hydrogen is sourced from fossil fuels (methane reforming). Greener hydrogen solutions are becoming more prevalent, but the demand for hydrogen is unsustainable at this current time [22].

1.2.2.2 Photocatalytic Conversion

Due to the oil crisis in the 1970s through to the 1990s, photocatalytic reduction of CO_2 gained great exposure. It was seen as an artificial method of photosynthesis, and since then, there has been extensive research, resulting in systems that can yield valuable compounds. [23] Some of the first work was conducted in 1982 by Jean-Marie Lehn through visible light irradiation of solutions containing Ru (2,2′-bipyridine)$_3^{2+}$, cobalt(II) chloride, and CO_2 in acetonitrile/water/triethylamine. This reaction generated carbon monoxide and water. [24] This work inspired further development and research for the photocatalytic reduction of CO_2, using semiconductor materials, transition metal complexes and enzymes. [25]

A photocatalytic process that uses semiconductors consists of the absorption of light photons equal to or greater energy than the band gap energy (E_{gap}) of a semiconductor catalyst (SCC). This excites electrons and holes to empty conductance and valence bands. The energetic charge carriers then initiate redox reactions to produce the final products.[26] The photogenerated electron and holes may follow different routes and trap at deep or shallow trapping sites. If the electrons do not find any trapping sites or the energy band gap is minimal, the electrons recombine and end up generating thermal energy at the surface of the photocatalyst. This decreases photoactivity; therefore, avoiding recombination is critical. The most desirable and efficient route would be the generated electron-hole being transferred to the adsorbed species on the photocatalyst surface. [26] [27]

To successfully reduce CO_2 with photogenerated electrons, an equal number of holes must be served to prevent charge recombination and increase the electron lifetime. Utilising electron donor reductants results in the holes being rapidly occupied and to supply hydrogen, which is needed to synthesise hydrogenated products. To form hydrogenated products of CO_2 reduction, the hydride reductants require simultaneous oxidation via oxidising agents; [26] however, the oxidation mechanism is beyond the scope of this thesis.

Photocatalysis has proven to be a good method to convert CO_2 into valuable products. Typically, the process requires a photocatalyst, a photosensitiser, and a reductant. The photosensitiser plays the role of producing a chemical change in molecules during photochemical processes. A simplified mechanism consists of the photosensitiser (Ps) adsorbing the radiation from the light source and entering an ‘excited state’ (Ps*) 1.2.4.

The excited state is then quenched by the reductant (R), which results in a reduced photosensitiser molecule (Ps-) and an oxidised reductant molecule (R+) 1.2.5. The reduced photosensitiser then transfers an electron to the catalyst (C) and reduces it (C-) 1.2.6. Reducing the catalyst allows it to bind with the CO_2 and reduce products 1.2.7. [28]

$$Ps + Light\ (h\nu) \rightarrow Ps^* \qquad 1.2.4$$

$$Ps^* + R \rightarrow Ps^- + R^+ \qquad 1.2.5$$

$$Ps^- + C \rightarrow Ps + C^- \qquad 1.2.6$$

$$C^- + CO_2 \rightarrow C + Products \qquad 1.2.7$$

The products obtained generally consist of carbon monoxide (which can undergo further reactions via the Fischer-Tropsch process), formate, and potentially alcohols (such as methanol [29]). The products depend on the photosensitiser and catalysts used, for example, using a copper (I) photosensitiser with an iron (II) catalyst. This photosensitiser-catalyst combination produced carbon monoxide as the main product via visible light irradiation. [30] An example of a semiconductor material catalyst is titanium oxide (TiO_2), a non-toxic, cheap and environmentally friendly material. This was used with aromatic alcohols as reductants to react with CO_2 to create a novel photocatalytic method to synthesise methanol under UV irradiation. [31]

Photocatalytic reduction of CO_2 does display great potential; however, it does not come without its drawbacks. Currently, the major limitation is that it is not the most efficient process concerning CO_2 conversion. It suffers from low catalytic turnovers, limited catalyst lifetime, and restriction to CO and formate as main products. There is a multitude of factors that limit the efficiency, starting with poor charge carrier separation efficiency. Other factors include the low solubility of CO_2 in water (~33 μM per 1 mL water at 100 kPa, room temperature) and the competing reaction of water reduction to hydrogen. [27] If the reactions depend on solar energy, this also poses an issue as it is inconsistent. UV radiation only contributes between 3-6% of the whole solar spectrum [32], and only 43% is in the visible light region [27]. Therefore, being able to harness the energy required would be dependent on location, time, and weather.

1.3 Electrochemical Reduction of CO_2

In comparison to chemical conversion of CO_2, photocatalytic and electrochemical reduction of CO_2 (ECO_2RR) has significantly advanced in the past decades. The electrochemical reduction of CO_2 has appealed to many chemists for many years. Some of the reasons are that it can potentially use renewable energy sources and has the potential to be upscaled very easily. [33] The challenge is the high stability of the CO_2 molecule, such that the energy input necessary to overcome the first reduction step is high. One of the main challenges faced in developing reliable catalysts capable of reducing CO_2 to selected hydrocarbon products for usage as fuels.

The dream is to create a CO_2 neutral cycle, where there is a balance of CO_2 produced and used, turning what is currently a greenhouse gas waste product into a precursor for usable chemicals and fuels. [34] Electrocatalytic conversion of CO_2 is gaining this recognition, with positives such as the process providing a low-cost source of protons without first generating H_2, reaction conditions are amiable (temperature and pressure) and supporting electrolytes are generally aqueous and fully recyclable. The reaction can be driven using renewable electricity; therefore, no CO_2 is produced in the process. Further advantages include that the electrochemical systems are compact, modular, and can be scaled up.

1.3.1 Background

Some of the earliest work on electrochemical reduction of CO_2 dates back to 1954, with the reduction of CO_2 using mercury electrodes conducted by Teeter and Rysselberghe.[35] Since then, numerous papers have been published on the topic over the decades. Many of the earlier papers reported that the only product in the cathodic reaction of CO_2 at metal electrodes was formate.[36] The metals used in many of these studies consisted of mercury, gold, lead, zinc, cadmium, tin and indium, and the experiments were conducted in aqueous inorganic salt solutions. However, these works did not factor in gas analysis and focused primarily on liquid-phase products. In 1985 it was reported by Frese Jr. and Leach that reduction of CO_2 over Teflon-supported ruthenium electrodes yielded carbon monoxide (CO), methane (CH_4) and methanol (CH_3OH).[37]

Frese Jr. and Leach's publication was one of the first papers to report gaseous substances as major products when reducing CO_2 in metal electrode systems with aqueous electrolytes.[37]

This led to further interest as much of the new research in subsequent years showed that it was possible to form CH_4, CH_3OH, CO, formaldehyde (HCHO) and formic acid (HCOOH) from the electrochemical reduction of CO_2 with the use of various electrodes. Transition metal complexes, in particular, were reported to produce CO effectively.[36]

Also, in 1985, Hori *et al.* conducted a comprehensive analysis of gaseous and dissolved products for the electrochemical reduction of CO_2.[36] This was carried out on a range of metals. Their report showed that cadmium, indium, tin and lead catalysts produced formate (HCOO-) predominantly and that gold and silver yielded mainly CO. The most interesting findings consisted of the result obtained when using copper, which yielded methane in a notable amount. The experimental conditions were also very reasonable, as it was conducted at ambient room temperature using a 1.0 M potassium hydrogen carbonate ($KHCO_3$) electrolyte. It was reported to take between 30 to 60 minutes and give a faradaic efficiency of 40% for methane. [36] This is said to be ground-breaking as it proved that it was possible to produce hydrocarbons with good faradaic efficiency in such friendly conditions.

1.3.2 **Metal Catalysts previously studied**

The electrochemical reduction of CO_2 has faced scrutiny due to the high overpotentials required, poor product selectivity, slow reaction kinetics and relatively low faradaic efficiencies.[38, 39] An ideal catalyst would yield useful hydrocarbon products with high faradaic efficiencies, good selectivity and economically.[40]

Table 1.3.1 displays the different metal catalysts studied by Hori *et al.* for ECO_2RR [41-43]. In this study, the electrode potentials at which reduction took place and the products yielded were studied. The yielded products were then evaluated, and the faradaic efficiency they were produced at was calculated. The products were formic acid ($HCOO^-$), carbon monoxide (CO), methane (CH_4) and hydrogen (H_2). According to this study, zinc, tin, indium, and lead performed exceptionally well to produce formic acid; however, their yield for other products was minimal.

The best performing catalyst for methane was seen to be copper, which out of all studied, yielded the most amount of methane, as well as small amounts of the other products. This study, therefore, paved the way for evaluating metal catalysts for ECO_2RR, with a particular focus on copper.

Table 1.3.1 Metal catalysts studied by Hori *et al.* for the electrochemical reduction of CO_2. Electrode potentials and faradaic efficiencies were reported for each metal.[41-43]

Electrode	Electrode Potential (V *vs.* Ag/AgCl [3.5 M KCl])	Product and Faradaic Efficiency (upper limit) / %
Tin (Sn)	-1.61	$HCOO^-$ (79.5) , CO (4.1) CH_4 (0.2) , H_2 (40.8)
Lead (Pb)	-1.83	$HCOO^-$ (88.8) , CO (0.6) CH_4 (0.2) , H_2 (30.9)
Indium (In)	-1.72	$HCOO^-$ (97.6) , CO (2.2) CH_4 (0) , H_2 (4.5)
Zinc (Zn)	-1.77	$HCOO^-$ (85.0) , CO (63.3) CH_4 (0) , H_2 (17.6)
Copper (Cu)	-1.60	$HCOO^-$ (16.5) , CO (3.1) CH_4 (40.0) , H_2 (33.0)
Silver (Ag)	-1.66	$HCOO^-$ (4.6) , CO (89.9) CH_4 (0) , H_2 (35.3)
Gold (Au)	-1.35	$HCOO^-$ (1.0) , CO (93.0) CH_4 (0) , H_2 (23.2)
Nickel (Ni)	-1.60	$HCOO^-$ (0.3) , CO (0) CH_4 (1.2) , H_2 (96.3)
Iron (Fe)	-1.63	$HCOO^-$ (2.1) , CO (1.4) CH_4 (0) , H_2 (97.5)

1.3.3 Cu for ECO_2RR

In the study conducted by Hori *et al.*., Cu stood out in being able to uniquely produce a number of hydrocarbons and alcohols. This, therefore, was seen as the only pure metal with the ability to reduce CO_2 to products that require two or more electron transfers with decent faradaic yields.[41, 44] A study in 2008 conducted by Hori *et al.* to obtain faradaic efficiencies of CO_2 reduction products on metal electrodes in $KHCO_3$ (0.1M CO_2 sat.) further solidified the case for Cu being a strong catalyst.

In this study, hydrogen, methane, ethylene, carbon monoxide, formic acid, ethanol and propanol were analysed during ECO_2RR over a range of metal catalysts (including those in Table 1.3.1). To reach this current density, a specified current density of -5 $mAcm^{-2}$ was set; therefore, the overpotentials for each metal studied were different and high. The potentials ranged between -0.52 to -1.24 V vs RHE. In this study, Cu was the only metal to produce amounts of all of the products, at an intermediate potential of -1.04 V vs RHE. An explanation for the unique property of Cu to be able to reduce CO_2 to products that require two or more electron transfers may be explained by the fact that it is the only metal to have a negative adsorption energy for *CO, but a positive adsorption energy for *H. All other metals had either negative or positive adsorption energies for both.[44-46] Hori *et al.* then proceeded to conduct chronoamperometry at potentials ranging from -0.4 to -1.05 V vs RHE. This study found that the most major ECO2RR products formed in detectable quantities were carbon monoxide, formate, methane, and ethylene. Kuhl *et al.* also conducted experiments under similar conditions in 2012 and was able to detect up to 16 liquid products via cryogenic NMR.[47]

Since these studies, interest in the use of Cu for ECO_2RR has grown exponentially, and due to this, attempts to understand the reaction mechanistically have progressed. Surface chemistries, morphologies, nanoparticles, and various other avenues have been explored to understand the mechanisms and tune for better efficiencies or selectivity. Most mechanisms appear to agree on the first step, which involves adsorption or activation of CO_2, with various geometries proposed.[48] To govern the selectivity of carbon monoxide or formate, the distinction of the adsorption intermediate on Cu is important, whether via a carbon atom or an oxygen atom. Alteration of the adsorption site is crucial in the formation of carbon monoxide or formate. Carbon monoxide on the Cu surface needs to be adsorbed long enough to allow for further reactions to form products such as methane, formaldehyde, and C_2 species.[48]

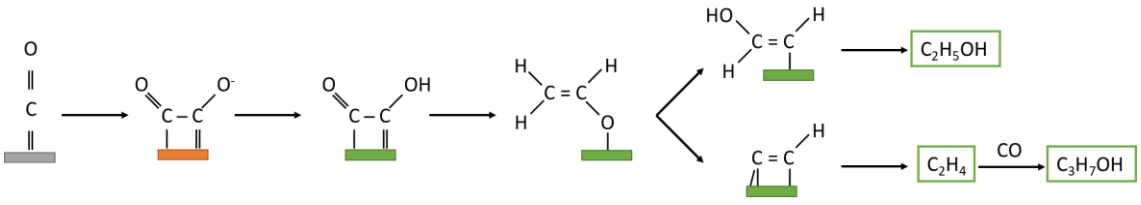

Figure 1.3.1 – Plausible reaction pathways from adsorbed *CO on Cu for C_1/C_2 products. Green base or box shows major C_2 products. Reproduced from Zhao *et al.* [48]

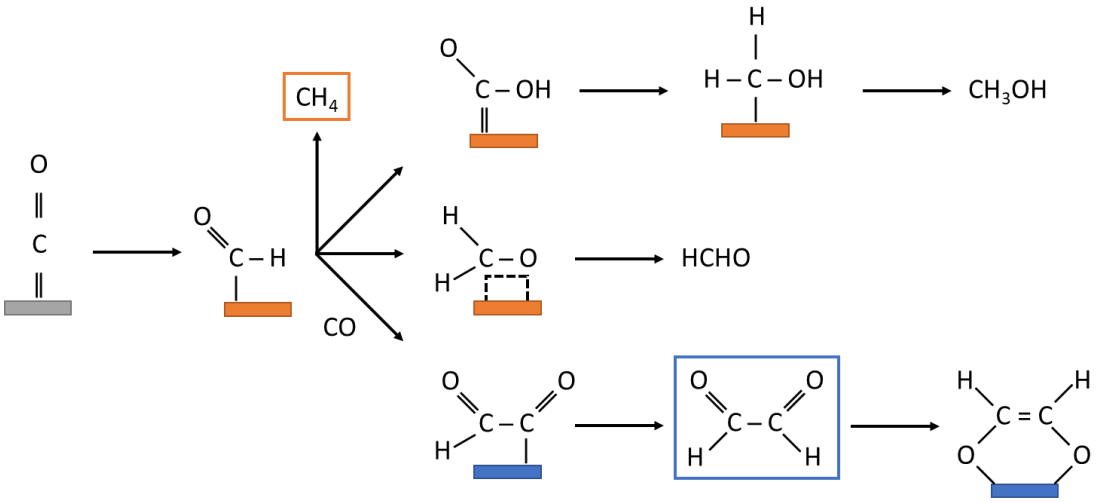

Figure 1.3.2 – Plausible reaction pathway from adsorbed *CO on Cu. Blue base or box to show trace C_2 product formation. Reproduced from Zhao *et al.* [48]

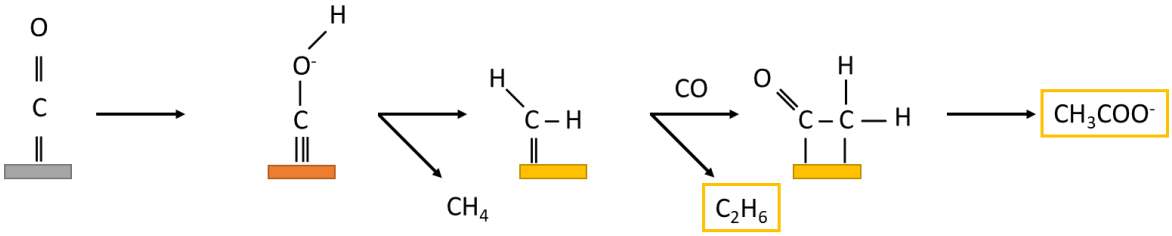

Figure 1.3.3 - Plausible reaction pathway from adsorbed *CO on Cu. Yellow base to show minor C_2 products. Reproduced from Zhao *et al.* [48]

Figures Figure 1.3.1 to Figure 1.3.3 show plausible reaction pathways from adsorbed *CO on Cu. When the environment is high pH, the pathway in Figure 1.3.1 would be favoured, while at low pH, the pathway in Figure 1.3.3 would be favoured. The intermediates are sensitive to the composition and structure of the Cu and the electrolyte and reaction conditions.[48] Further discussion into these factors, however, are outside of the scope of this thesis.

1.4 Challenges Summary

The potential for CO_2RR is great, paving the way for a greener future by using what is essentially a waste product. Progressing further, however, will require significant technological advances for this process to be economically viable and recognised to help the world.

In current times, the development of electrochemical CO_2RR relies on fulfilling three criteria: High energy efficiency, stability in the long term and achieving high current densities for reaction rates and turnover.

One of the most significant hindrances to the progress is the fact that there is a significant lack of understanding of the CO_2RR mechanism. Many have attempted to model this through experimental and computational methods,[49-52] but the pathways to generate valuable products or intermediates have not been elucidated definitively. Making the pathways clear would provide great insight into the chemistry behind CO_2RR at the electrode/electrolyte interface and mechanisms to achieve high faradaic efficiencies or those detrimental to this. To achieve these high faradaic efficiencies, a multitude of factors require taking into consideration and their sub-branches. The catalyst must be able to suppress competing HER while also being selective towards the desired products. Therefore, the operating conditions must be optimised to give the best yields and efficiencies. The Faradaic efficiency of most products has been seen as around 90% for formic acid and carbon monoxide, around 70% for methane and ethylene.

Another hindrance to consider is the high overpotentials associated with these reactions. The amount of energy put into the system versus the products gained from this is minimal; therefore, reducing this high overpotential is required. The high overpotential can be attributed to the limiting step in CO_2RR, which is the formation of the radical anion intermediate $CO_2^{\cdot -}$. In water and many solvents, the equilibrium potential for forming this anion intermediate is very negative, thus resulting in a high overpotential. Therefore, the role of the catalyst would be to stabilise this intermediate. The solubility of CO_2 is also relatively low in most aqueous electrolytes in the friendly conditions used for CO_2RR, therefore introducing a mass transfer limitation of the CO_2 to the electrode surface.

Therefore, a combination of a suitable catalyst, reactor design, and efficient product analysis is necessary to efficiently reduce CO_2 and achieve the target of obtaining high-value products. In recent decades, the field of Electrochemical CO_2 Reduction has seen incredible growth and achievements; however, there is still limited scientific knowledge of the catalytic mechanisms. The multiple bond breaking and forming processes and the sheer complexity of the reaction environment contributes to major difficulties elucidating precise catalytic mechanisms and pathways, thus hindering the fine-tuning of the reaction conditions, kinetics and chemistry.

Further research is also required to understand and suppress the competing and parasitic hydrogen evolution reaction (HER) process and hydrogen protonation to reduce this via catalysts or tweak experimental conditions. However, the future of electrochemical CO_2 reduction, or the whole field of CO_2 reduction, is bright, as research has accelerated significantly to ensure a brighter future for further generations.

1.5 Thesis objectives and overview

The objective of this work was to establish the foundations of research into the electrochemical reduction of CO_2. Specifically establishing and scrutinising an array of analytical methods and techniques to analyse the liquid and gaseous products created by electrocatalytic CO_2 reduction. In line with this objective, the thesis focuses on integrating adaptable and user-friendly electrolysis reactor cells that can be used with various analytical techniques, namely On-line Electrochemical Mass spectrometry (OLEMS) and Gas Chromatography (GC). The reactors in which electrocatalysis occurs are important as this may compromise the reaction and the ability to identify products.

In **Chapter 3,** analytical methods of product analysis are reviewed, and a host of analytical equipment used in this thesis are described in the context of their set-up and calibration to form an array of analytical methods covering most products of ECO_2RR. In **Chapter 4,** an electrochemical approach to determine the concentration of formaldehyde is outlined as a lesser reported yet known product of CO_2 reduction. The subsequent chapters detail electrolysis reactor cell design developments for use with OLEMs. **Chapter 5** details the development of a user friendly and adaptable dual-platform flow cell for the analysis of a range of electrode substrates and catalytic modifications using OLEMs and is directly compared with a commercial electrolysis cell.

2 Electrochemical Theory

2.1 Introduction

Electrochemistry can be defined as a branch of chemistry that studies the relationship between chemical and electrical effects. It is a study of how charge moves through physical and chemical systems at a molecular level. The works of Compton and Banks [53] and Bard and Faulkner, [54] inspire the electrochemical theory derived in this chapter, with theory applicable to electrochemical reduction of CO_2 influenced by the works of Qiao, Liu and Zhang. [4]

Generally, electrochemical experiments are carried out in reaction cells consisting of two electrodes and an ionic conducting electrolyte (which can be in liquid or solid form). These electrodes act as an electron source or electron sink and, in some cases (such as CO_2RR), act as a catalyst for the reaction. The redox reactions between them are analysed via the independent half-reactions taking place at each electrode. A reduction reaction occurs at the cathode, and an oxidation reaction occurs at the anode.

$$Ox + n\,e^- \rightarrow Red$$

Equation 2.1.1 - Reduction half-reaction

The reaction occurs at the interface between the electrode and the electrolyte. The electrode where desired reactions are taking place is known as the working electrode. As a redox process must happen in the cell, the other electrode is known as a counter electrode. Where a specific working electrode potential is necessary, a reference electrode is generally introduced into the system. This should be of constant composition and act as a reference potential in the cell with respect to which the working electrode potential is altered. The most common reference electrodes used are silver-silver chloride (Ag/AgCl) and saturated calomel electrode (SCE).

A cell that produces electricity resultant of spontaneous reactions is known as a galvanic cell. An electrolytic cell is a cell where non-spontaneous reactions are driven by applied current from an external source.

2.2 Electrode Potential

A minimum of two electrodes are required, as the potential difference between the two can then be measured. A simple example is to build a circuit consisting of two metal electrodes (A and B) inserted into a solution. A voltmeter can be used to measure the potential difference between each metal. This (high resistance) voltmeter measures the potential difference by passing a minimal current through. The current is small enough that the electrode or electrolyte is unaffected and purely allows measurement.

The potential difference ($\Delta\Phi$) can be expressed as:

$$\mathrm{DF} = (\Phi_A - \Phi_S) - (\Phi_B - \Phi_S) = (\Phi_A - \Phi_B)$$

Equation 2.2.1 - Potential Difference expression. $\Delta\Phi$ = Potential Difference (V) $\Phi_{A/B}$ = electrochemical potential of the metal, Φ_S = solution potential.

($\Phi_M - \Phi_S$) denotes the electrode potential of each metal electrode - solution interface. The individual potentials are unknown and will have a dependence on the type of metal, the surface state of the metal and solution properties such as ion concentration and temperature. To solve this, an element with a constant or known electrode potential can be added to the system. This is known as the reference electrode, and the potential difference in the system can be calculated by subtracting the known reference electrode potential.

2.2.1 Standard potentials

A reference electrode must be designed so that the composition of the electrode and solution remains constant and unaffected by outside factors. The Standard Hydrogen Electrode (SHE) can be used as an example. When reporting, SHE is used as a standard; therefore, if a different reference electrode was used, a conversion to SHE is made for consistent reporting.

Typically all thermodynamic data concerning electrochemical potentials are made with respect to the SHE. The SHE comprises a platinum electrode immersed in acid of known activity (as opposed to concentration) under a constant supply of hydrogen gas. The half-reaction is thus:

$$Pt(s) \mid H_2(g) \mid H^+(aq)$$

Equation 2.2.2 – Half-reaction of platinum (Pt) electrode immersed in acid of known activity.

Therefore, the standard electrode potential is $(E^0) = 0\ V$. This applies at all temperatures. It is achieved from the activity (a) of the hydrogen ions being equal to 1, and the pressure (P) also being 1 bar. The standard potential of a redox couple (X) is equal to the cell potential; therefore, the SHE becomes the left side electrode, and X forms the right side:

$$Pt(s) \mid H_2(g) \mid H^+(aq) \mid\mid X$$

Equation 2.2.3 - SHE forms the cell's left side, while X forms the right.

$E^0 = E^0(X)$ represents standard potential. To obtain the standard cell potential of a cell, the difference between the two standard electrode potentials is taken:

$$E^0_{cell} = E^0(R) - E^0(L)$$

Equation 2.2.4 - Obtaining standard potential of cell by taking the difference of two standard electrode potentials.

Standard Hydrogen Electrode (SHE) represents the potential of a platinum electrode in an ideal solution (theoretical). This means that it is the current standard for zero potential at all temperatures. Normal Hydrogen Electrode (NHE) represents the potential of a platinum electrode when in a 1 M acidic solution. Reversible Hydrogen Electrode (RHE) consists of a hydrogen electrode in which the potential is dependent on the pH of the solution.

2.2.2 **Practical Reference Electrodes**

The use of reference electrodes is relatively ubiquitous in electrochemical experiments. As mentioned previously, for practicality reasons, the most common reference electrodes used are silver-silver chloride (Ag/AgCl) and saturated calomel electrode (SCE). This range of reference electrodes stems from the fact that a reference electrode must be reliable in the reaction environment. Of course, different electrochemical experiments use differing conditions or electrolytes; therefore, the correct reference electrode must be chosen.

SHE has been arbitrarily used to define 0 V; however, practical use for this electrode can be problematic as hydrogen gas is required. The HCl (1.18M) electrolyte is also only compatible with aqueous experiment conditions. Due to this, Ag/AgCl has found its place in becoming the most commonly used reference electrode. It is easily prepared and has a very stable potential. It is also suitable for use with any aqueous electrolyte within the entire 0-14 pH range.

An Ag/AgCl reference electrode is composed of an Ag wire, on which AgCl is deposited. This wire is then placed into a tube-like vessel containing a NaCl or KCl solution. The top of the vessel is generally capped off with a connector, and the base of the vessel contains a glass frit, allowing Na^+ ions to permeate and allow conductivity.

Therefore, this glass frit prevents the electrolyte from being analysed to mix with the *Cl solution inside the reference electrode. The difference in *Cl solutions and concentrations affects the potential vs the SHE. Variants of the Ag/AgCl reference electrodes can be found in Table 2.2.1, along with the potentials of others.

Another well-documented electrode is the SCE. This is used less in modern experimentation because it is composed of mercury oxide (HgO) and mercury sulphate ($HgSO_4$). In this study, an SCE is used to test the stability of the Ag/AgCl electrodes being used as the vessels can deteriorate in quality over time, therefore compromising the stability of the reference.

Table 2.2.1 Reference electrode potentials *vs.* SHE. [55, 56]

Reference Electrode	Potential *vs.* SHE
Standard Hydrogen Electrode	±0.000
Ag/AgCl (Sat. KCl or NaCl)	+0.198
Ag/AgCl (3.5 M KCl or NaCl)	+0.205
Ag/AgCl (3.0 M KCl or NaCl)	+0.210
Ag/AgCl (1.0 M KCl or NaCl)	+0.237
Saturated Calomel Electrode	+0.242

2.3 Thermodynamics

2.3.1 Chemical and Electrochemical Potential

When it comes to thermodynamics, there must be a level of reversibility in the system, as thermodynamic processes are considered to be when systems are in equilibrium and steady-state. The reversibility can include chemical, practical and thermodynamic reversibility.

In an electrochemical system, the whole reaction is split into two half-reactions. The reaction at the right electrode and the reaction at the left. To analyse the thermodynamic equilibrium and the energy of the whole reaction, the change in Gibbs free energy is required. This is given by ΔG:

$$\Delta G = \left(\sum_i s_i \mu_i\right) right - \left(\sum_i s_i \mu_i\right) left$$

Equation 2.3.1 - Gibbs free energy equation. ΔG = kJmol^{-1}, μ_i = Electrochemical processes of species i (kJmol^{-1}), s_i = Stoichiometric coefficient of i

The change in the Gibbs free energy can also come from the potential difference in the cell reaction. This gives:

$$\Delta G = -nFE$$

Equation 2.3.2 – Change in Gibbs free energy. n = Number of moles of electrons (mol), F = Faraday's constant (96485 $Cmol^{-1}$), E = Cell potential (V)

At this point, it is worth mentioning the definition of overpotential. Overpotential (η) is the potential difference between the half-reaction thermodynamically determined reduction potential (E) and the actual potential where redox is observed experimentally (E_i).

$$\eta = E_i - E$$

Equation 2.3.3 - Calculation of overpotential

This equation for Gibbs energy gives the critical relationship between chemical and electrical energy for cell reactions. From this equation, the entropy change can be given.

$$\Delta S = -\left(\frac{\delta \Delta G}{\delta T}\right) = nF\left(\frac{\delta E}{\delta T}\right)$$

Equation 2.3.4 - Change in entropy using Gibbs. ΔS = Entropy (JK^{-1}), T = Temperature (K)

This can then be substituted into the equation for Gibbs free energy with regards to enthalpy (rearranged for enthalpy ΔH ($J\ mol^{-1}$)):

$$\Delta H = \Delta G + T\Delta S = nF\left[\left(\frac{\delta E}{\delta T}\right) - E\right]$$

Equation 2.3.5 - Gibbs free energy equation rearranged for enthalpy, with entropy substituted.

Furthermore, to calculate the equilibrium constant (K) of an electrochemical reaction:

$$\Delta G = -RTlnK = -nFE$$

Equation 2.3.6 - Equilibrium constant (K). R = Ideal Gas Constant (8.314 JKmol^{-1}),

This equation enables the prediction of electrochemical data from thermochemical data and sets up for the important Nernst equation.

2.3.2 The Nernst Equation

The Nernst equation is known to be one of the most fundamental equations for electrochemistry. It can give a quantitative value of electrodynamic potentials and reactant activity.

According to chemical equilibrium isotherm formulas, the change in Gibbs free energy:

$$-\Delta G = RTln\left(\frac{a^0_{products}}{a^0_{reactants}}\right) - RTln\left(\frac{a_{products}}{a_{reactants}}\right)$$

$$-\Delta G = RTlnK^0 - RTln\,K$$

Equation 2.3.7 - Change in Gibbs free energy according to chemical equilibrium isotherm formulas. a = Activity (molL^{-1}) where superscript ^{0} represents the chemical species in their standard state

Where $RTlnK^0$ can be considered the standard Gibbs energy,ΔG^0 comprising all the chemical species in their standard state. Recalling equation 2.3.6, replace Gibbs energy:

$$\boldsymbol{nFE = nFE^0 - RTln\,K}$$

Equation 2.3.8 - Gibbs energy substitution

Rearranging for cell potential:

$$E = \frac{nFE^0}{nF} - \frac{RT}{nF}lnK$$

Equation 2.3.9 - Equation 2.3.8 rearranged for cell potential.

When operating in non-standard conditions, the equation therefore becomes:

$$E = E^0 - \frac{RT}{nF} \ln Q$$

$$\mathrm{Q} = \left(\frac{a_{products}}{a_{reactants}} \right)$$

Equation 2.3.10 – The Nernst Equation

Equation 2.3.10 is the natural logarithmic form of the Nernst Equation, where Q is the reaction quotient for the chemical species involved. Generally, standard electrochemical reactions are reported at a standard temperature of 298.15 K and often given with respect to $\log_{10}$.

Substituting all values in the equation therefore gives:

$$\boldsymbol{E} = E^0 - \frac{(2.303) * (8.314) * (298.15)}{n * 96485} log\, Q = \boldsymbol{E^0 - \frac{0.0592\ V}{n} \log Q}$$

Log = 2.303 * Ln (conversion)

Equation 2.3.11 - Nernst Equation with numerical values.

2.3.3 Thermodynamics for CO_2RR

2.3.3.1 CO_2RR Principles

CO_2 can undergo electrolysis to provide a multitude of products. The product formation can stem from different experimental conditions, therefore showing that the reactions undergo different mechanisms under different conditions. There have been many proposed mechanisms for the electrochemical reduction reaction on different catalysts; however, the copper catalyst is the most common. This work mainly focuses on the catalysis of CO_2 using copper; therefore, examples of mechanisms proposed over copper catalysts are discussed.

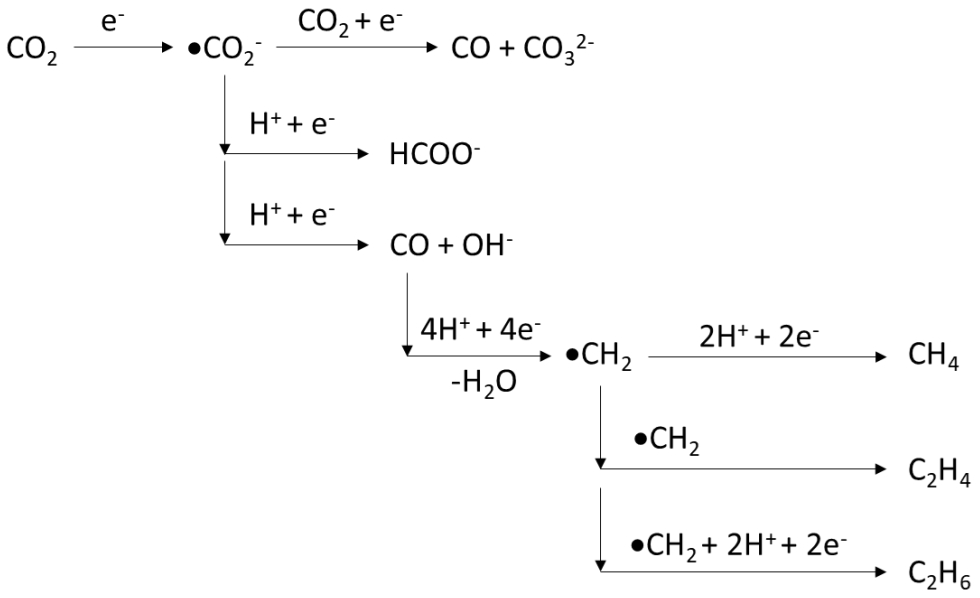

Figure 2.3.1 – A proposed mechanism for the electrochemical reduction of CO_2 using a copper catalyst in methanol.[57]

Figure 2.3.1 shows the proposed mechanism for CO_2 reduction at a copper catalyst in methanol. It displays the variety of pathways that can be taken; however, it is applied to reactions in anhydrous solvents. When working in aqueous solutions, as most electrolytes used (*i.e.* $KHCO_3$), the mechanism for formate proposed is as follows.

$$CO_2 + e^- \rightarrow CO_2^{\cdot-} \quad (1)$$

$$CO_{2\ ads}^{\cdot-} + H_2O \rightarrow HCO_{2\ ads}^{\cdot} + OH^- \quad (2)$$

$$HCO_{2\ ads}^{\cdot} + e^- \rightarrow HCO_2^- \quad (3)$$

$$CO_2^{\cdot-} + xH + e^- \rightarrow HCO_2^{\cdot} + x \quad (4)$$

Figure 2.3.2: Accepted mechanism for electrochemical reduction of CO_2 in aqueous electrolytes. xH represents proton-providing substances.[4]

Pinpointing the mechanism for CO_2RR is notoriously difficult, and there are multiple mechanisms out there; however, they are all proposed and undetermined and naturally have a strong dependence on the nature of the catalyst and experimental conditions. Further discussion into the specific mechanisms and their variations are out of the scope of this thesis. There are many factors that influence the reduction reaction; however, they can be broadly addressed experimentally.

2.3.3.2 Influential factors affecting CO_2RR

There are a whole host of factors that can affect the outcome of CO_2RR. These can include but are not limited to the electrodes used, heterogeneous or homogenous catalysts, the electrolyte, the temperature, the pH, the electrode potential and resistance, and the design of the reactor. Optimising these points is essential in ensuring that the reaction is taking place as efficiently as possible. In this thesis, reactor designs are discussed; however, the main focus is heterogeneous catalysis and the analysis methods required to elucidate catalytic mechanisms and analyse the wide variety of products formed from copper catalysed CO_2 reduction.

2.4 Dynamic electrochemistry

Understanding the thermodynamics behind an electrochemical system is vital in predicting the direction of the electrochemical reaction; however, the kinetics of the reaction are not considered. Applying a potential across electrochemical systems can force non-spontaneous reactions to occur. The subject of kinetics focuses on the mechanisms by which the reactions occur and their rates. Mass transport of a reaction is not considered by thermodynamic predictions either. This transport is of the reactants to the electrode surface. The kinetics of a reaction and the mass transport occurring come under the umbrella of dynamic electrochemistry.

The distinction between faradaic and non-faradaic processes must be understood where kinetics are concerned. Faradaic processes describe the transfer of charge across the electrode-electrolyte interface, causing oxidation or reduction of the electrolyte. Faradaic processes are named in this manner as Faraday's Law of electrolysis governs them; therefore, the magnitude of the chemical reaction is proportional to the number of electrons passing through the system. Non-faradaic processes, on the contrary, involve a change in the structure of the interface as the potential or electrolyte solution composition changes (via adsorption of ions). It is essential to know the distinction as both processes occur in electrochemical reactions.

2.4.1 Mass Transport

Mass Transport is a collective term that describes the preferred movement of dissolved species in solution. It splits into three subcategories; Diffusion, Migration and Convection.

2.4.1.1 Diffusion

Diffusion consists of the movement of species in response to a concentration gradient. To achieve optimum entropy, equilibrium is required. Diffusion, therefore, works to maintain this equilibrium by homogenising the concentration distribution in an electrolyte.

The rate of diffusion depends on both the local concentration gradient at any point and how the concentration gradient evolves. Fick's first law of diffusion shows the relationship between the concentration gradient and the diffusional flux (J), the amount of substance per unit area over time of species (A).

$$J = -D\left(\frac{\delta[A]}{\delta x} + \frac{\delta[A]}{\delta y} + \frac{\delta[A]}{\delta z}\right)$$

J = Diffusional Flux vector

D = Diffusion Coefficient of A (cm^2s^{-1})

A = Concentration of species

x,y,z = Position

Equation 2.4.1 - Fick's first law of diffusion.

Fick's second law must be applied to consider how the concentration of species changes over time. To obtain this, the first law is differentiated with respect to time (t):

$$\frac{\delta[A]}{\delta t} = D\left(\frac{\delta^2[A]}{\delta x^2} + \frac{\delta^2[A]}{\delta y^2} + \frac{\delta^2[A]}{\delta z^2}\right)$$

Equation 2.4.2 - Fick's second law, obtained by differentiating the first law with respect to time.

The diffusion coefficient (D) in both laws is temperature-sensitive. It is a measure of the diffusional velocity of a species in solution.

The root mean squared (RMS) displacement in time, therefore, provides a measure of the distance the molecule has diffused over time:

$$\sqrt{\langle x \rangle} = \sqrt{2Dt}$$

Equation 2.4.3 - RMS of displacement in time to provide a measure of molecular diffusion distance.

Generally, the magnitude of D is in the range of 10^{-6} to 10^{-5} cm^2s^{-1} for species at room temperature in conventional solvents. Due to this, mass transport by diffusion is very slow. Assuming no migration or convection effects, the diffusion of a species by even one centimetre could take up to or more than 24 hours.

2.4.1.2 Migration

Migration concerns the movement of charge resultant from an external electric field. A common source of an electric field is the drop in electrical potential at the electrode-electrolyte interface.

The migrational flux of species (A) through a field (Φ) is directly proportional to its concentration and ionic mobility (u):

$$J_m \propto u[A]\frac{\delta\phi}{\delta x}$$

Equation 2.4.4 - Migrational flux of species A through a field (Φ).

When electrolysis takes place, this electric field is generated at the electrode-electrolyte interface. Therefore, the ionic movement is influenced, meaning ions move in response by being attracted to or repelled from the interface. The ionic rearrangement can cause the electric field to evolve, making migration effects challenging to predict or interpret from experimental data.

Due to this difficulty of prediction and interpretation, it is desirable to try and minimise migration effects. This can be achieved by introducing chemically and electrochemically inert (background) electrolytes into the system. When a solution has high ionic strength, evolved electric fields do not occur as the background electrolyte ions quickly migrate to maintain electrical neutrality over the interface.

2.4.1.3 Convection

Convection takes place due to mechanical forces acting on the electrolyte. This can be introduced from external sources, or natural convection is possible. When introduced from an external source, it can be in the form of stirring (stirrer bar) or bubbling (vibrations and movement caused by the bubbles). Even when controlled, the convection effects are unpredictable; therefore, avoiding unnecessary convection can be critical. In some cases, the convection can be described mathematically. In hydrodynamic electrode systems, such as flow cells, convection is beneficial as the electrochemical response can directly correlate with the convection (*i.e.* electrochemical response from flow rate changes). Natural convection can result from differences in density or thermal gradients within the solution. Natural effects are often negligible when an experiment is operated in a controlled environment on small surface area electrodes to record small current densities.

2.4.2 Electrochemical Kinetics

2.4.2.1 Aspects of Electrochemical Kinetics

Electrochemical reactions are heterogeneous reactions. Reactant molecules must be within the electrode-electrolyte interface to react. The reaction occurring can be described by three steps that take place:

1. First mass transfer – The approach of the reactant to the surface of the electrode.
2. Main reaction – Heterogeneous electron transfer across the interface.
3. Second mass transfer – The departure of the product away into the bulk electrolyte.

Step 2 can be accompanied by chemical reactions which are taking place in the electrolyte or on the electrode surface. These reactions can consist of electron transfer and adsorption at the electrode surface, depending on the electrode potential. To determine the order of the steps and the rate determining step (RDS) is essential to describe specific processes on the electrode dynamically. For example:

$$Ox + n\,e^{-} \rightleftharpoons Red$$

Equation 2.4.5 – Standard representative redox reaction equation.

In this electrode reaction, both oxidised (*Ox*) and reduced (*Red*) forms of a redox couple are present initially in the bulk solution.

For the forward reduction process, the rate (v_f):

$$v_f = k_f C_{Ox}(0,t) = \frac{i_c}{nFA}$$

Equation 2.4.6 - Forward reduction process rate equation.

For the backward oxidation process rate (v_b):

$$v_b = k_b C_{Red}(0,t) = \frac{i_a}{nFA}$$

$k_{f\,/\,b}$ = Forward / Backward reaction process rate constant

C_{Ox} / C_{Red} (0,t) = Surface concentration of Ox or Red at time *t* (s)

$i_{a\,/\,c}$ = Anodic / Cathodic current (A)

n = Number of moles of electrons (mol)

F = Faraday's constant (96485 $Cmol^{-1}$)

A = Electrode area (cm^2)

Equation 2.4.7 - Backward oxidation process rate equation. Key applies to Eqn 2.4.6 also.

To obtain the net reaction rate, therefore:

$$v_{net} = v_f - v_b = k_f C_{Ox}(0,t) - k_b C_{Red}(0,t) = \frac{i}{nFA}$$

Equation 2.4.8 - Equation to obtain net reaction rate.

To finally obtain the overall current:

$$i = i_c - i_a = nFA\,[k_f C_{Ox}(0,t) - k_b C_{Red}(0,t)]$$

Equation 2.4.9 - Overall current of reaction.

The accurate kinetic activity of an electrode process can be obtained by determining the current as a function of potential.

There is proportionality between the net rate of an electrode reaction and the current. The reaction rate is a strong function of the electrode potential.

When the net current is at zero, *i.e.* at equilibrium, the Nernst equation defines the electrode potential:

$$E = E^{0\prime} - \frac{RT}{nF}\ln\left(\frac{C'_{Ox}}{C'_{Red}}\right)$$

C'_{Ox} / C'_{Red} = Bulk concentration of Ox or Red (mol/L^{-1})

$E^{0'}$ = Formal potential (V)

Equation 2.4.10 - Nernst equation to define electrode potential.

When a Faradaic current is passed, the equilibrium value of the electrode potential deviates. This is known as 'Electrode Polarisation'. The magnitude of the polarisation is determined using the overpotential.

$$\eta = E_i - E^{0\prime}$$

Equation 2.4.11 – Overpotential (η) determination during electrode polarisation.

Based upon the Butler-Volmer model of electrode kinetics, for a single electron, single step, reversible electrode process, the derived current-overpotential equation is as follows:

$$i = i_0\left[\frac{C_{Ox}(0,t)}{C'_{Ox}}e^{-\alpha\frac{F}{RT}\eta} - \frac{C_{Red}(0,t)}{C'_{Red}}e^{(1-\alpha)\frac{F}{RT}\eta}\right]$$

i_0 = Exchange current (A)

α = Transfer coefficient

Equation 2.4.12 - Butler-Volmer current-potential equation.

The exchange current (i_0) represents the Faradaic current at equilibrium. This is equal to i_a or i_c. The exchange current value can be calculated by:

$$i_0 = FAk^0\ C'_{Ox} e^{-\alpha \frac{F}{RT}(E_{eq} - E^{0'})}$$

Equation 2.4.13 - Calculation of exchange current value.

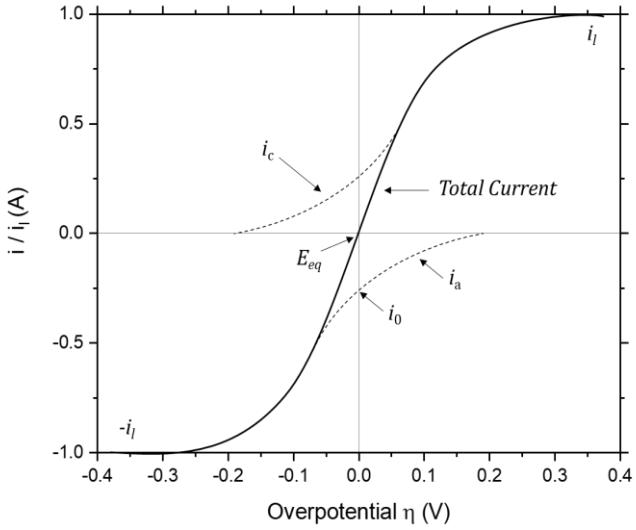

Figure 2.4.1 - Current - Overpotential curves as a representation of the derived Butler-Volmer Equation, with an example system. [54]

i_l = Limiting Current

α= 0.5, T = 298 K, $i_{l,c} = -i_{l,a}$, $i_0 / i_l = 0.2$

Dashed lines show currents of $i_{a/c}$

Figure 2.4.1 displays the behaviour shown in the derived Butler-Volmer equation (2.4.12). From this, it can be seen how at a high overpotential at the cathodic branch, the i_a is insignificant, and vice versa at very positive overpotentials. The total current is the sum of both i_a and i_c. At the extremities of overpotential, the current is seen to plateau, meaning it has reached the limiting currents ($i_{l,c}$, $-i_{l,a}$). These limiting currents stem from mass transfer limitations, and the overpotential can be said to be a 'concentration overpotential'.

At certain overpotentials, the process on the electrode may take place in many small slow steps, and overpotentials from different reaction steps can drive the current.

These can consist of:

- Mass transfer overpotential (η_{mt})
- Charge transfer overpotential (η_{ct})
- Preceding reaction overpotential (η_{rxn})

However, the main relationship between the electrode overpotential and the current generally depends on the nature of the most limiting step. This, therefore, allows a hypothesis to be drawn about the processes being investigated.

When no mass transfer effects are being included in the study, equation 2.4.12 transforms into what is traditionally known as the Butler-Volmer equation:

$$i = i_0 \left[e^{-\alpha \frac{F}{RT}\eta} - e^{(1-\alpha)\frac{F}{RT}\eta} \right]^{Ox + n\, e^- \rightleftharpoons Red}$$

Equation 2.4.14 - Traditionally known Butler-Volmer equation when no mass transfer effects are included in the study.

The overpotential's sole purpose when no mass transfer effects are considered is to drive heterogeneous processes at the rate determined by the current. The exchange current and activation overpotential are inversely proportional; therefore, the lower the exchange current, the larger the activation overpotential. This would therefore display slower kinetics.

When the overpotential value is small to a certain extent, equation (2.4.14) can be expressed as:

$$i = i_0 \frac{F}{RT}\eta$$

Equation 2.4.15 - Equation 2.4.12 when the overpotential value is small.

This shows that the corresponding current-overpotential curve near E_{eq} (in a small potential range) is linear with the reciprocal slope of the current-overpotential (-η/i). This is known as the charge-transfer resistance, R_{ct}.

$$R_{ct} = \frac{RT}{Fi_0}$$

Equation 2.4.16 - Charge-transfer resistance equation.

When considering a large overpotential (positive or negative), equation (2.4.15) transforms further. Looking at the cathodic branch, the equation transforms to:

$$i = i_0 e^{-\alpha \frac{F}{RT} \eta}$$

Equation 2.4.17 - Change in equation 2.4.15 when considering large overpotential (cathodic).

This can also be rearranged to be expressed as:

$$\eta = \frac{RT}{\alpha F} \ln i_0 - \frac{RT}{\alpha F} \ln i$$

Equation 2.4.18 - Rearranging equation 2.4.17 for overpotential.

This therefore, can now be compared to the Tafel equation:

$$\eta = a + b \log i$$

Equation 2.4.19 - Tafel equation.

Substituting the constants (and converting the ln value) gives the following definitions:

$$a = \frac{2.303RT}{\alpha F} \log i_0 \qquad b = \frac{2.303RT}{\alpha F}$$

Equation 2.4.20 - Tafel equation after substituting constants and ln conversion to define (a) and (b).

An indicator of fully irreversible kinetics can be seen when Tafel behaviour is indicated. Plotting log i vs the overpotential (a Tafel plot, Figure 2.4.2) gives a helpful evaluation of the kinetic parameters, such as the transfer coefficient.

The Tafel plot in Figure 2.4.2 is a plot of equation 2.4.17, as the potential is controlled and current is measured. The Tafel equation derives a plot where overpotential is on the Y-axis, and the log of the current is on the X-axis. This is because the Tafel equation preceded the Tafel plot, therefore, controlled the other way around. The resultant plots are different, meaning the gradient per decade interpretation is therefore different.

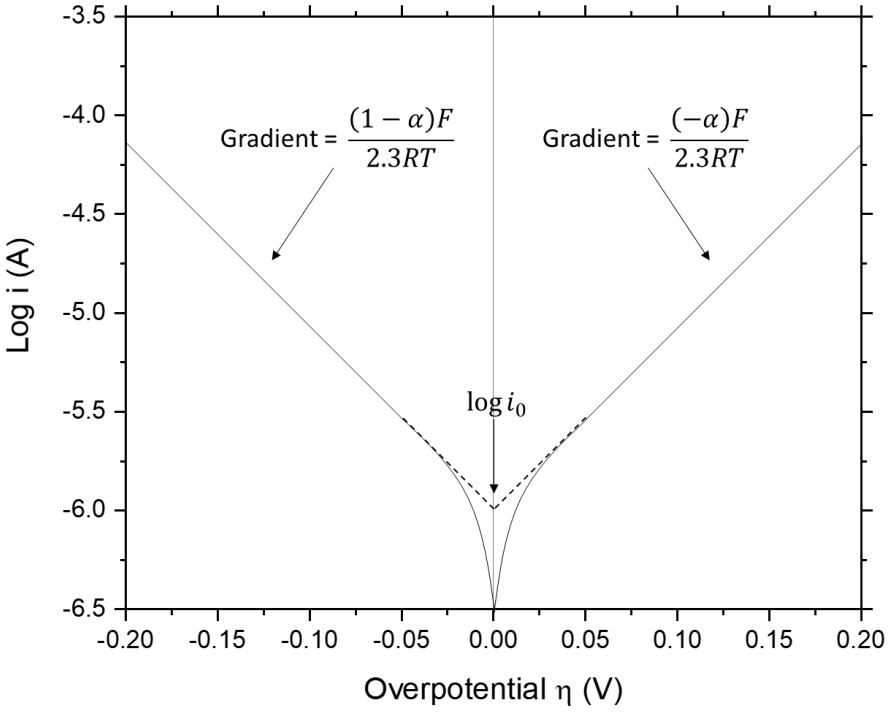

Figure 2.4.2 - Example Tafel plot shows the anodic and cathodic branches of a current-overpotential curve. [54]

α= 0.5, T = 298 K

As seen from the example Tafel plot in Figure 2.4.2, the linear nature deviates as the overpotential approaches zero. Therefore, this only applies to potentials lower than -0.05 V or above 0.05 V. Furthermore, current deviation will occur at higher potentials. The concentration at the electrode surface strays from the bulk, and mass transport effects occur. Therefore, the linear range to conduct Tafel analysis is incredibly limited and only suited to irreversible processes.

2.4.3 **Kinetics of CO_2RR**

2.4.3.1 Overpotentials in CO_2RR

Direct electrochemical reduction of CO_2 on most electrode (catalyst) surfaces requires a high overpotential to drive the process. This, in turn, has a massive effect on efficiency as ensuring all of the energy input is converted to desired product is difficult. This requirement for high overpotential stems from the stability of the CO_2 molecule, and it is also speculated that the involvement of an intermediate species; the $\bullet CO_2^-$ anion radical. This anion requires a very negative potential for formation. The overpotential is dependent on factors such as the metal of the electrode, orientation of the surface and the crystals, and the availability of protons. The product of the reduction may also play a role in overpotential. Carbon monoxide formation can take place at lower overpotentials than that of formate (HCOO-). When the anion radical stabilises on electrodes, this can result in a reduction of the electrode overpotential.

2.4.3.2 Solubility of CO_2

Due to the nature of the experiment and the background, the friendliest conditions are preferred for conducting CO_2RR research. The electrolytes generally used are therefore aqueous and low in concentration. CO_2 solubility in the aqueous electrolyte is seen to be relatively low, resulting in issues and limitations such as selectivity, achievement of higher current densities, and poor mass transport of the CO_2 to the surface of the electrode. The solubility of CO_2 in water is reported to be around 30 mM (at 1 atm, 25°C), and as the electrolytes used are generally aqueous, this value is not significantly affected. The solubility can be increased by decreasing the temperature of the media or increasing the pressure of the system. Solvents such as methanol can also be added to increase the solubility; however, as methanol is a desired product of the reaction, it introduces inaccuracy in the products formed and is somewhat self-defeating.

As the solubility has an adverse effect on the mass transfer, it is essential to ensure that conditions are optimised to ensure solubility is increased or at least consistent. The rate of CO_2 mass transfer to the surface of the cathode is also optimised.

2.4.3.3 Electrolyte choice

When conducting electrochemical CO_2RR, the electrolyte of choice must not affect the quality of the products formed. The hydrogen evolution reaction (HER) is seen as a parasitic reaction that can cause the pH of the electrolyte to increase and inhibit active sites of the electrode surface. Higher solution pH increases the amount of hydrogen on the electrode surface, and electrodes with a high affinity for hydrogen will be inhibited, reducing or even stopping any CO_2RR on the surface. Catalyst choice remains very important as promoting CO_2RR while suppressing HER requires the catalyst to mediate multiple electron transfers at low overpotential. Coupling a copper electrode with $KHCO_3$ (0.1M, pH 6.8), KCl (0.1M, pH 5.9), $KClO_4$ (0.1M, pH 5.9) and K_2SO_4 (0.1M, pH 5.8) was seen to favour the CO_2RR reaction, yielding desirable products (methane, ethylene, ethanol, propanol) at higher faradaic efficiencies than other electrolytes tested. [4, 41, 43, 58]

Table 2.4.1 - Faradaic Efficiencies of Electrochemical CO_2RR using a Cu electrode. Galvanostatic at 5 $mAcm^{-2}$ at 19°C. [43]

				Faradaic Efficiency (%)			
Electrolyte	Concentration (M)	pH	Potential (V vs SHE)	CH_4	C_2H_4	Ethanol	Propanol
$KHCO_3$	0.1	6.8	-1.41	29.4	30.1	6.9	3.0
KCl	0.1	5.9	-1.44	11.5	47.8	21.9	3.6
$KClO_4$	0.1	5.9	-1.40	10.2	48.1	15.5	4.2
K_2SO_4	0.1	5.8	-1.40	12.3	46.0	18.2	4.0
K_2HPO_4	0.1	6.5	-1.23	17.0	1.8	0.7	<0.5

2.5 Principles of electrochemical methods

Analysis of the electrochemical behaviour of a system is possible through a multitude of different electrochemical methods. For ECO_2RR in particular, electrochemical characterisation of the catalyst, the electrolyte and the overall performance is vital to ensure performance is maximised. Characterisation and evaluation of performance can be done through cyclic voltammetry (CV), linear sweep voltammetry (LSV), chronopotentiometry (CP), and chronoamperometry (CA). This section provides a brief overview of CV, LSV, Chrono methods, and their applications for ECO_2RR.

2.5.1 Cyclic Voltammetry

Cyclic Voltammetry (CV) is a very widely used method of electrochemical measurement. Potential is swept in both negative and positive directions through a range of potentials, and the current response is measured. CV is versatile and can provide important information about the electrodes, catalysts and conditions with a range of applied potentials. CVs are conducted during initial characterisations or investigations of prospective catalysts and can usually provide information regarding electron transfers and identify potentials of interest.[59] The window in which the CV takes place can be controlled to be a non-destructive method. The current is measured during the application of the potential sweep, from an initial potential (E_{init}) to a chosen end vertex potential (E_{end}). Another vertex potential can be chosen so that the sweep does not return to the initial potential, and therefore the potential window being analysed is between the two vertices. The initial potential is where no net reaction occurs and can be at OCP; therefore, a negligible current is being passed, not affecting the reaction. The chosen end vertex is relative to the item being analysed, and potential windows for most can be found from literature sources to set vertex boundaries.[4]

Once the end vertex potential is reached, the sweep direction is reversed (E_{end}, t_{switch}), returning to the initial or set vertex potential. Reverse reactions taking place can be observed and analysed by the current response of the reverse sweep. This results in a cyclic voltammogram showing the current response of the front and reverse sweep. Figure 2.5.1 displays a typical cyclic voltammogram obtained alongside the potential scheme as a function of time.

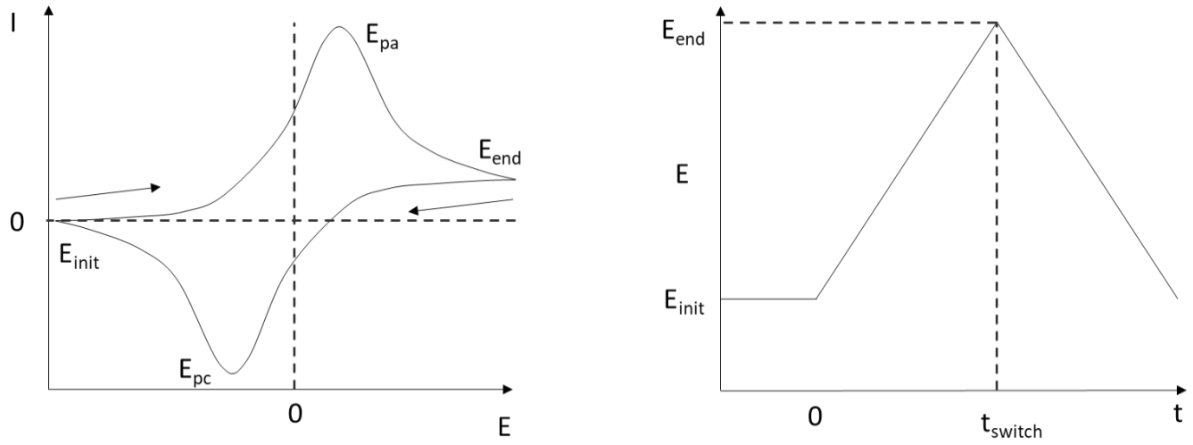

Figure 2.5.1 - Typical reversible cyclic voltammogram. Arrows show direction of potential sweep (Left). Potential scheme as a function of time for cyclic voltammogram (right).[4, 54, 59]

On the cyclic voltammogram, peaks in the current show the potential points at which electrochemical oxidation and reduction are taking place. These are respectively labelled E_{pc} (cathodic peak) and E_{pa} (anodic peak). Once the peak has been reached, the current response decays. The peaks appear due to mass transport effects, as the movement of the substrate to the electrode surface faces diffusion rate limitations, which is slow compared to the electron transfer step. Upon application of high enough overpotentials, the concentration of the substrate close to the electrode reduces to zero, reducing the current response as a depletion layer grows.[59] When using CV as a method, the reversibility of the reaction can be assessed through analysis of the currents and potentials observed. During the CV, if the peak-to-peak separation of a redox couple increases, it can be indicative of a quasi-reversible system. If there is no overlap of the forward and reverse processes on the potential axis, or there is no reverse peak, the process can be said to be irreversible. When exploring new catalysts, electrolytes and conditions for ECO_2RR, benchmarking experiments are required to evaluate the species prior to further usage. An example may be the use of a new heterogeneous catalyst in CO_2 sparged 0.1 M $KHCO_3$. Characterising this catalyst to understand current responses would require first running CV in a specific electrochemical potential window to understand which potentials the electrode shows an oxidation or reduction response. For ECO_2RR, the reduction peak would be necessary as this shows at which potential; the highest reduction current response is obtained. Cyclic voltammetry may also be used to condition electroplated electrodes and ensure the surface chemistry is correct for the desired response.

2.5.2 **Linear Sweep Voltammetry**

Linear sweep voltammetry (LSV) is an electrochemical method that can conduct half of the reaction that a CV does. Instead of a potential being swept forward and reverse, the potential is only swept one way. This enables pure focus on an oxidative or reductive reaction, allowing slower scan rates to observe the reaction without the direction of the sweep being swapped.

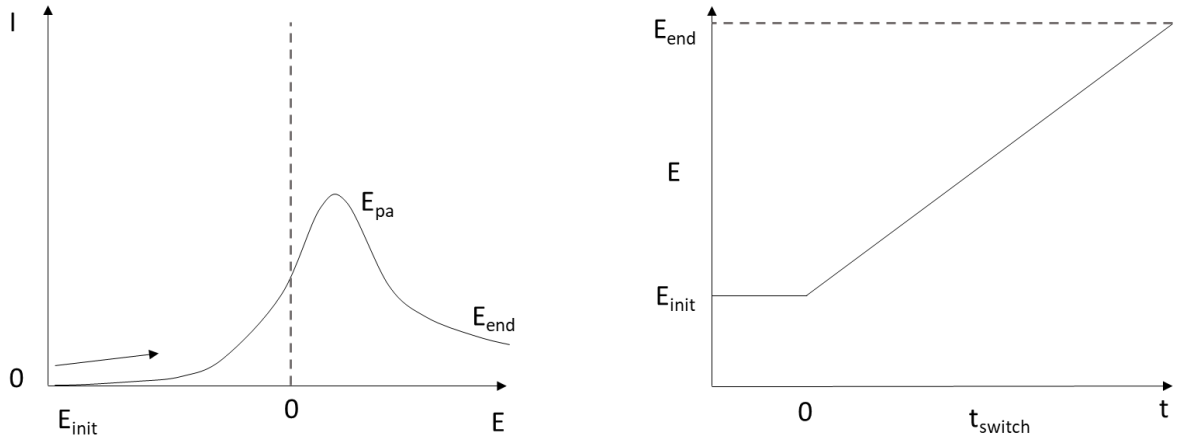

Figure 2.5.2 - Typical Linear Sweep Voltammogram (left), Potential scheme as a function of time (right).[4, 54, 59]

As ECO_2RR is a reduction reaction, the majority of the experimentation is only conducted in the reduction regions. Due to this, LSV is a popular technique to obtain and pinpoint the potentials that give a good reduction response and current response. The response of the species for ECO_2RR can also be analysed over a range of negative potentials, as the product formation may differ as the potentials are swept through.

2.5.3 **Chronopotentiometry and Chronoamperometry**

Chronopotentiometry (CP) and Chronoamperometry (CA) consist of the analysis of potential at a fixed current (CP) and the analysis of current at a fixed potential (CP) as a function of time.

The currents or potentials applied are determined through literature values or determined using CV or LSV. Using those techniques, the value where a peak appears can be isolated and used with CP or CA. Most commonly for ECO_2RR, CA is used as reduction potentials are obtained through CV or LSV. The current response is monitored at this potential and the product formation through analytical techniques. Chrono techniques may also be used in longevity studies. The current response may change over time with catalyst, electrolyte degradation, or changes in the environment from pH altering product formation. Explanation of the drop in response may be attributed to an increase in diffusion layer, therefore reducing electroactive substrate and lowering current response.[59] Determination of the reduction potential and the ability to observe the longevity of the electrode allows increased development to optimise the potential and current response further. In this thesis, CA is used after the determination of potential by LSV.

2.6 Electrochemical reactor cells

2.6.1 **Introduction**

In the field of ECO_2RR, there has been a vast amount of reactor cell development since the first cells were used by Hori *et al.* [41, 43]. The intricate complexities of each design vary depending on the application; however, they can be categorised for ease of understanding. One of the most critical factors is electrolyte convection; therefore, two major categories are Static and Flow cells. In a static cell, the electrolyte is not constantly replenished, and all electrochemistry takes place within a fixed volume, often with a finite amount of CO_2. The electrolyte is constantly flowed through and replenished at the electrode interface in a flow cell. Introducing a flowing electrolyte into the system assists in reaction longevity and mitigates electrolyte degradation. Over time, the CO_2 in the electrolyte is 'spent'; therefore, introducing fresh, saturated electrolyte is advantageous. A flow system, however, brings in added complexity.

To ensure successful experimentation of the electrochemical reduction of CO_2, the reaction cell must be designed to consider a multitude of factors.

First, the cell must be designed to minimise cell resistance. Resistance can be introduced into the cell by placing electrodes too far apart or the connecting path for electrolyte in between being obscured. Therefore, mass transport kinetics and ohmic resistance must be taken into strong consideration, ensuring the space between the counter and working electrodes and the working and reference electrodes is reduced. The electrolyte must also be conductive enough to allow for low resistance mass transport, and any separating membrane must allow for low resistance diffusion while separating anodic and cathodic electrolytes.

Furthermore, the user-friendliness of the cell is a significant factor. Often, complex and intricate designs are seen in the literature, created specifically for their study. However, these designs can make it difficult for users other than the researcher (or research group) undertaking the study.

Consideration for other users is important; therefore, a design that can be used by those new to the studies may prove advantageous in the future. An example of this is seen in Chapter 5, where a commercial cell's user-friendliness is reviewed.

Finally, sampling from the cell requires very strong consideration. Designing a cell where liquid and gas phase products can be efficiently formed and sampled is key to the success of ECO_2RR.

2.6.2 **Three-Electrode Cell**

A three-electrode cell incorporates the anode, cathode and reference electrode into a single vessel. The simplicity of this setup involves no separate chambers or membranes and can be used efficiently for electrochemical experiments in which the anodic and cathodic electrolytes can be mixed. Figure 2.6.1 is a diagrammatic example of a three-electrode cell.

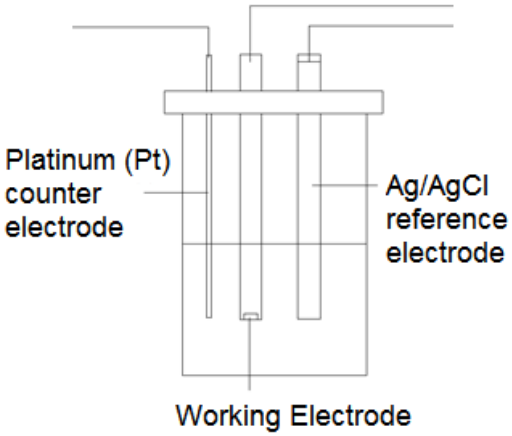

Figure 2.6.1 - Conventional three-electrode cell with a Pt anode, VC cathode and Ag/AgCl reference electrode as an example.

Three-electrode cell setups have been reported in the literature to conduct ECO_2RR on single crystal Cu, [60] Cu_2O-derived Cu nanoparticles, [61] and for various other studies of the catalytic mechanism (especially in homogenous catalysis) [62-68]. These studies are conducted with a focus on catalyst performance for CO_2 reduction. This simple setup allows direct monitoring of the catalyst for validation before usage in more complex setups. Furthermore, the electrochemical method to be used on these catalysts can also be decided. This can include adjusting the parameters to control catalytic selectivity towards higher value hydrocarbons or from parasitic reactions such as hydrogen evolution (HER).

The advantage of using this conventional three-electrode cell system is that the electrodes can be placed very close, reducing resistance introduced by mass transport limitations and ohmic losses. There is also no electrode convection due to electrolyte flowing, and convection can be introduced and easily controlled using a magnetic stirrer bar.

Finally, this cell is one of the most user-friendly and is used to introduce electrochemistry to students and those embarking on an electrochemical journey for the first time.

2.6.3 **Bulk electrolysis cells: The H-cell**

One of the most renowned lab-scale bulk electrolysis reactors for ECO_2RR is the H-type cell (H-Cell). In a conventional H-cell, the working (cathode) electrode and reference electrode are placed into the cathodic compartment, while the counter (anode) electrode is placed in a separate anodic compartment. The dimensions and volumes are generally the same for both compartments.

A PEM separates the two compartments to prevent reduced products from being oxidised again and vice versa. This type of cell has been used in multiple publications. [69-83] Figure 2.6.2 shows a conventional H-cell setup.

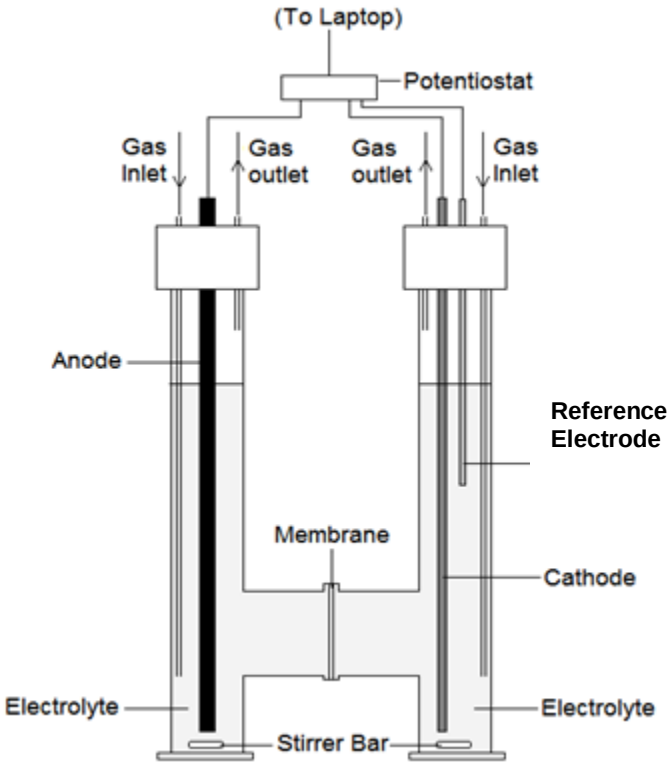

Figure 2.6.2 - Conventional H-Cell setup

In this setup, analysis of products resultant from a single half-reaction is possible. Gaseous and liquid products are isolated to their respective side, enabling the collection and sampling of products created by the anodic and cathodic processes.

The design can feature multiple ports for electrode entry or electrolyte sampling. H-cells feature similar advantages to those of the three-electrode cell, as the working and reference electrodes can be placed close. Convection inside the H-cell can be introduced using stirrer bars, as there is no flow convection to account for. The convection, however, can be seen to be inferior to the linear convection of the flow cell. Ohmic resistances are also increased depending on the spacing between the working and counter electrodes due to the space required to fit the flange that holds the membrane.

This, in turn, would result in higher overpotentials. This can be combatted by attempting to insert the electrodes so that they sit close to the membrane, but this requires specialist design. Surface area limitations are also an issue these cells face, as each electrode's surface area and the membrane are limited to a specific size. H-cells are scalable; however, to try to rectify this issue.

Sampling from an H-cell for gaseous products can be conducted with a gas-tight (GT) syringe; however, in some publications, CO_2 is seen to be flowed into the cell (controlled by a mass flow controller) and sampled by GC at an exhaust. This, therefore, shows that it is possible to do an on-line analysis of the products being formed at the cathode working electrode. Longevity of the reactions and electrolyte face the same issue as the three-electrode cell, as the electrolyte can end up 'spent', reducing the activity.

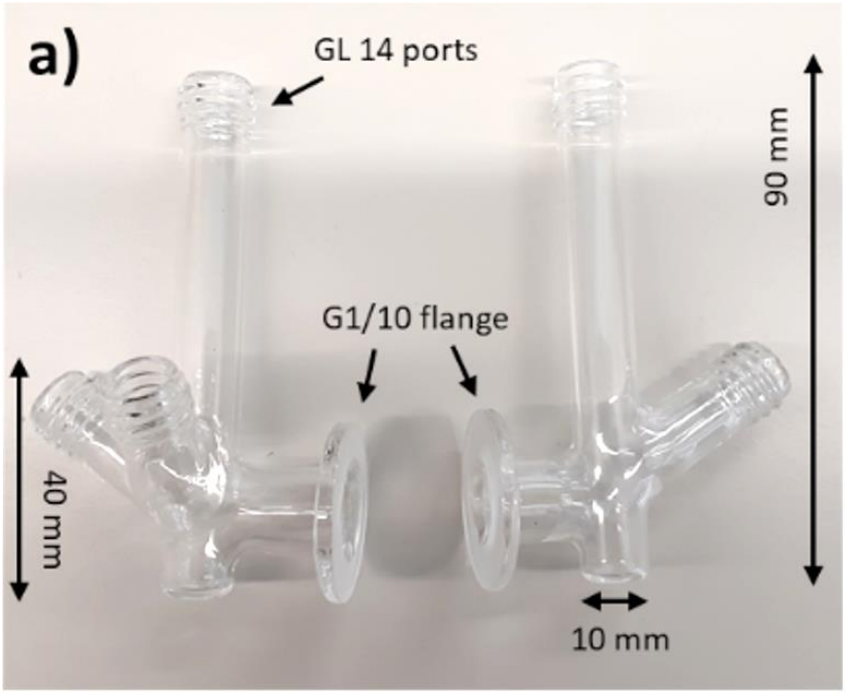

Figure 2.6.3 - Glass H-cell used for preliminary experiments for ECO_2RR.

2.6.4 **Flow Cell**

Flow cell technology has been used for decades prior to the research into ECO_2RR. Flow cells have been adapted from the fuel cell and water electrolyser technologies due to their efficient mass transfer and ability to replenish spent and degraded electrolyte.

Therefore, mass transfer limitations in static cells are overcome with the continuous circling of reactants to and products away from the electrode interfaces.

This enables constant, high concentrations of CO_2 at the electrode catalyst surface. Due to the low solubility of CO_2, flow cells also enable gas-phase electrochemical reduction.

The kinetics and thermodynamics of a flow cell are very different from static cells. Due to this, they are much more scalable, therefore paving a path for commercial and large-scale applications [84] [85]. The term 'flow cell' can be applied to any cell with a flowing electrolyte; however, the most used for ECO_2RR are Proton Exchange Membrane Flow Cell (PEMFC). Due to the efficiency of the PEMFC, the design has been studied and adapted in a multitude of ways.

A flow cell setup is required to achieve a cell where electrolyte samples can be taken and analysed during experimentation (or analysed on-line) and have a constant stream of fresh electrolytes to replace any contaminated.

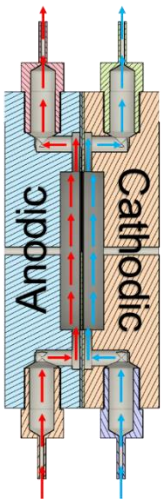

Figure 2.6.4 - Typical electrochemical flow cell cross section. Red shows anodic electrolyte flow, blue shows cathodic electrolyte flow. Both flows are separated by a PEM.

Flow cells can be said to be the most complicated setup with regards to CO_2 reduction. There are significant differences in the kinetics and thermodynamics of CO_2 electroreduction within flow cells, and there are parameters that require setting for optimal results. As expected, one of the main parameters consists of the flow. The flow rate must be fast enough to clear products (both gasses in the form of bubbles and liquid phase) while slow enough for the highest (most efficient) conversion of CO_2.

The delivery of CO_2 to the cathode also depends on the cell type. The cell design can consist of a purely gas-phase flow system, a gas-diffusion electrode (GDE) system, or a totally liquid-electrolyte based system. Figure 2.6.4 shows a liquid electrolyte based system, which would consist of a CO_2 – saturated electrolyte entering the cell and then exiting with the products in the electrolyte stream.

When it comes to GDE cells, the complexity arises considerably. Gas-phase flow systems consist of a similar design; however, there is no liquid electrolyte, and the catalyst is (or mounted upon) a gas diffusion electrode. The CO_2 gas is delivered directly to the cell. Instead of chambers for the anodic and cathodic chambers, there are flow plates located behind the GDEs. The separation of both chambers is achieved using a polymer electrolyte membrane (PEM), which facilitates ionic flow and reduces product crossover. The products are then collected upon exit via an on-line system or GT syringes. As the CO_2 is being delivered to the cell directly, the amount delivered can be controlled using a mass flow controller, allowing quicker conversion calculation and faradaic efficiencies.[86-88]

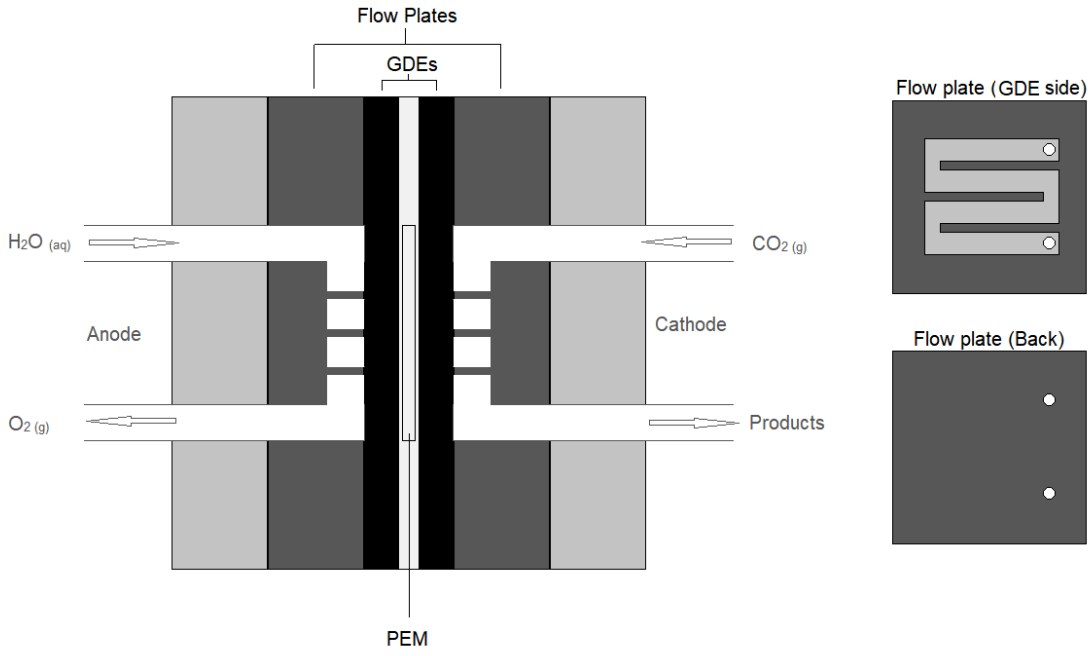

Figure 2.6.5 - Gas-phase flow system.

In recent years, there has been increased usage of GDE systems for ECO_2RR. Due to the poor solubility of CO_2 in aqueous electrolytes (~ 34 mM) [86], challenges have been faced in achieving high conversion rates and faradaic efficiencies. Therefore, many researchers have moved to cell designs, which allow vapour-phase CO_2 to be delivered to the catalyst to help overcome the solubility issues and performance barriers. Gas diffusion electrodes (GDE) achieve this as they are composed of a porous catalyst layer deposited on a diffusion matrix, facilitating the transport of reactants. GDEs have been used in research for fuel cells and water electrolysers for high current densities and minimised mass transport losses.

2.7 Summary

To summarise this chapter, the fundamentals of electrochemistry are discussed. This includes electrode potential, covering the potential difference, standard potentials, half-reactions and practical reference electrodes. Thermodynamics and kinetics of electrochemical systems are also discussed, with focus on Gibbs free energy and the Nernst equation for thermodynamics, and mass transfer, reactions, overpotentials for kinetics. The thermodynamics and kinetics when concerning electrochemical CO_2 reduction, in particular, are discussed, with a focus on mechanisms (thermodynamics) and overpotentials, CO_2 solubility and electrolyte choice (kinetics). Mechanisms and pathways for reactions are still disputed; therefore, understanding proposed mechanisms is essential due to the influence on methodology. The kinetics are also fundamental as the efficiency of the experiments being carried out can be significantly affected by factors such as overpotential and poor electrolyte choice. Principles of electrochemical methods are discussed, focusing on cyclic voltammetry and linear sweep voltammetry as the most common methods used. As electrochemical methods are discussed, it is vital to understand the different electrochemical reactor cells used. This chapter details three of the main types of electrochemical cells historically used, focusing on the field of ECO_2RR.

In this work, the progression of cell design has utilised the basis described in this chapter. Cell design plays a vital role in the efficiency, configuration and usability of the reactor. This thesis considers the cell (reactor) design for ECO_2RR product analysis and user-friendliness and adaptability.

3 ECO_2RR Product Analysis

3.1 Introduction to Product analysis

In 1985, Yoshio Hori explicitly stated in a publication the following;

"No publication has reported total analysis of products (gaseous and soluble in electrolytes) in the electrochemical reduction of CO_2 at metal electrodes." [36]

As time has progressed, there have been advances both in the electrochemical aspects of CO_2 reduction and product analysis. Product analysis plays a key role in determining whether an electrochemical method, catalyst, electrolyte or overall conditions are effective. Each publication uses its own array or adaptation of methods for product analysis. Hori *et al.*., for example, reports utilising ion chromatography (IC) for liquid phase analysis [36], yet Hong *et al.*. utilised an array that included using gas chromatography (GC), high-performance liquid chromatography (HPLC) and IC.[89] The fact that there is no standard procedure is due, in part, to the fact that the electrochemical reduction of CO_2 yields a multitude of products in different phases, ionic states, and often at low concentrations. At least 16 different products can be obtained when using a copper catalyst. This was highlighted in a 2012 publication by Jaramillo *et al.*., where reduction using copper foil yielded products ranging from formate to glycolaldehyde.[47] Table 3.1.1 displays some of the potential products. [4, 38, 39, 47, 90, 91]

Table 3.1.1 - Products that can be formed during the electrochemical reduction of CO_2. [4, 38, 39, 47, 90, 91]

Product	Formula
Ethylene	C_2H_4 (g)
Ethanol	C_2H_5OH (l)
Methane	CH_4 (g)
Methanol	CH_3OH (l)
Formaldehyde	HCHO (l)
Formic Acid	HCOOH (l)
2-Propanol	C_3H_7OH (l)
Acetic Acid	CH_3COOH (l)
Oxalic Acid	$C_2H_2O_4$ (l)
Carbon Monoxide	CO (g)
Hydrogen	H_2 (g)

Due to the variety of products and their phases, a single analytical technique for all proves to be impossible. General trends can be seen when product analysis has been described in publications. However, it is rare for a publication to explain the in-depth analysis, especially concerning the methodology used. Method development for ECO_2RR product analysis, therefore, proves to be challenging. This chapter discusses the different methods which have been used for product analysis historically, as well as the methods which have been established during this work.

3.2 Product analysis methods

3.2.1 Gas Chromatography (GC)

Gas chromatography (GC) is a popular analytical technique. It is very commonly used in research and industrial labs for the qualification and quantification of gaseous or volatile species. Gas chromatography works on the basis of the separation of gasses by their reaction to the stationary phase. A sample is introduced to the GC by injection, either manually or via a sample loop. The sample is carried by the carrier gas (generally helium, the carrier gas acts as the mobile phase) through into the column. The packing of the column absorbs components of this sample differently. This causes the components to flow through separately and exit the column at different times. The detector records this and is known as 'retention time', *i.e.* how long the compound was retained in the column. The retention times can be matched with data from calibration standards or online sources such as manufacturer application notes if similar conditions (*e.g.* column, flow rates, injection type) are used. Provided that a calibration plot has been made prior, the integral area of the peak can be used for quantification of the sample.

Due to the range of products resultant from the electrochemical reduction of CO_2, there has also been a difference in the columns used between publications. Carbon columns, molecular sieves, and micropacked and porous layer open tubular (PLOT) columns prove popular choices due to the nature of the obtained products. The products mainly produced include lighter gasses; therefore, the column of choice must be either packed in a way that the lighter gasses can react or must be long enough to ensure their detection. [39, 92, 93]

The column is not the only variable when it comes to the physical equipment. The detector required when conducting gas chromatography may also need to be different. Many different detectors can be coupled to the GC equipment. The following describes those typically used for CO_2 electroreduction product analysis.

3.2.1.1 Thermal Conductivity Detector (TCD)

The TCD is one of the earliest developed detectors for GC and is regularly used in CO_2 product analysis. TCDs work by analysing the change in thermal conductivity of the carrier gas due to the sample by comparing the thermal conductivity of pure carrier (reference) gas with the eluted. Electrically heated wires in the detector are affected by this thermal conductivity change in the gas flowing around them.

Therefore, the change in thermal conductivity is sense as a change in electrical resistance, which is measured. An advantage of using a TCD is that they are easy to use and can detect inorganic compounds. A significant disadvantage of using a TCD for CO_2 electroreduction product analysis arises from its sensitivity (<40 ppm). Further disadvantages include response towards carrier gas impurities and stationary phase bleeding from the column. TCD is also seen to be very sensitive to changes in flow rate; therefore, discrepancies may be seen during experiments where the temperature or flow is programmed. As newer detectors are being developed, they become more sensitive and can detect trace analytes. TCDs give chromatograms that display peaks for the retention times of the components in the sample. [92, 93 39]

3.2.1.2 Flame Ionisation Detector (FID)

This detection method utilises an air-hydrogen flame to chemically decompose the samples (pyrolysis). The samples are ionised due to this decomposition, and these ions and the electron currents are recorded using a picoammeter. FID can also be used to analyse volatile liquid phase from liquid injections or headspace samples.

They are considerably more sensitive than TCDs and are less affected by issues that may affect the accuracies of TCDs. FIDs are unable to detect inorganic substances such as N_2 and H_2 and are not a favourable method to detect oxygenated species (*e.g.* formaldehyde) as they cannot undergo pyrolysis [92, 93 39]. Methanizers can be coupled with FID detectors to allow CO detection by hydrogenating the CO to methane (CH_4). However, one of the main products of interest is methane; therefore, a method to differentiate the methane produced from the experiment and methanized CO would be required.

3.2.1.3 Mass Spectrometer (MS)

Mass spectrometry alone is a popular method of qualifying products by analysing their molecular weights. It can be used as a stand-alone method or coupled with equipment such as GC, both for on-line and off-line methods (*e.g.* DEMS, which is an on-line *in-situ* method)

When coupled with GC, it can be one of the most powerful detection methods. Coupling GC with MS allows direct qualification of the products eluting from the column. This is displayed as a ‘total ion chromatogram’ (TIC), which shows the intensity vs the time. The peaks displayed by the TIC are then examined for the fragmentation pattern at that time.

The fragmentation pattern can then be used to identify the product which eluted. The intensity of the peak can also be used to quantify the product.

To qualify the product, if one is unable to find out from the displayed mass, nuclear mass data is always readily available, and recent software comes with a library search function. This means that the fragmentation pattern can be matched with ones in their database and the closest match is displayed, therefore revealing the product's identity with ease.

Disadvantages associated with the use of MS include the fact that the sample may decompose between the GC and the MS. The MS inlet may not be set correctly or may just decompose before being able to undergo MS. Another issue would be quantification with just the MS; however, this can be resolved by using the TIC displayed.

GC-MS is one of the most commonly used analysis methods for ECO_2RR, as it is able to identify almost all of the products of interest from the reaction. One of the significant drawbacks to GC-MS is the costs associated. To obtain a GC-MS capable of analysing products to the trace quantities produced from ECO_2RR, triple quadrupole systems would be required.

3.2.1.4 Barrier Ionisation Discharge Detector (BID)

In recent years, a detector known as a ‘barrier discharge ionisation detector’ (BID) has been introduced. This was seen to have twice the sensitivity of FID and almost 100 times the sensitivity of TCD. It also did not require the use of a methanizer for the analysis of CO and CO_2. Another advantage over FID is that it is able to respond to N_2, O_2 and oxidised organic substances, if required, simultaneously.

The basis of the BID is a dielectric barrier discharge ionisation source, a low-temperature helium (He) plasma in a state of non-thermodynamic equilibrium. The plasma is generated by two electrodes, one of which is coated with a dielectric material. An electrical discharge takes place between them, producing the plasma. High voltage alternating current (HV-AC) is applied to the electrode coated in di-electric material to initiate the discharge. This applied voltage goes beyond the breakdown voltage of the discharge gas (He). The discharge is initiated between both electrodes. The photons and metastable species are then responsible for ionising ($h\upsilon$, ΔE=17.7 eV) the components for detection [94-97].

The detector, which is now commercially available [98], is based upon the principle of dielectric barrier discharge ionisation with He plasma gas. It is operated at a medium frequency (5 to 30 kHz) and a high voltage (5 to 10 kV). This is applied to a central ring electrode, and the two outer electrodes are grounded. A quartz tube running between the ring acts as a dielectric barrier, across which the discharge is initiated. The produced ions are a product of the oscillating electrical field between the electrodes, therefore enabling ion current detection.

GC-BID has found several valuable applications. Antoniadou *et al.* [94] analysed semi-volatile and volatile organic compounds such as alcohols and polycyclic aromatic hydrocarbons to investigate the performance of GC-BID. The result consisted of superior sensitivity of the BID detector by a factor of 4 compared with an FID detector. Studies using GC-BID have been applied to the products from CO_2RR using other methods such as photocatalytic reduction. GC-BID was able to analyse CO, H_2 and O_2 produced by photocatalytic reduction of CO_2 in an aqueous solution of NaCl [99].

Due to the nature of the products formed during ECO_2RR, the selection of analytical techniques and arrays depends on the type of analyte, *i.e.* light hydrocarbon, small inorganic compounds, and the physical state of the product (gaseous or liquid). The variation of products formed can mean a diverse array of analysis equipment is required. Selecting the suitable analytical technique for detecting and quantifying CO_2 reduction products generally depends on the analyte being a small inorganic compound or a light hydrocarbon and the physical state of the product being gaseous or liquid.

3.2.1.5 GC for CO_2 electroreduction product analysis

ECO_2RR yields a multitude of products in different phases. However, GC is a very popular method as it can analyse most gas and volatile liquid phase products [36, 39, 83, 100]. To use this as a versatile product analysis method, one must first obtain the correct column(s) for separation and the appropriate detector for the limits of detection and products undergoing analysis.

The introduction of the sample to the column may also be conducted in different ways, depending on the ECO_2RR reaction. GC can be used for either on-line or off-line analysis. On-line analysis involves using a gas sampling loop. The gasses flowing out of the reaction cell fill the loop.

The sampling loop is then set to load an aliquot of this gas onto the column for analysis, therefore analysing on-line the products coming from the cell. This set-up is generally used with GDE-type cells where the gaseous stream differs from the electrolyte stream. The gas flow stream must also be regulated to prevent pressure in the reaction cell.

When running GC for samples obtained post-electrolysis, a 'headspace' injection is usually conducted for the sample, especially if it is a sample of the post-run electrolyte. A headspace injection consists of just the vapour above a sample being analysed. Therefore the needle does not touch the liquid sample. This is only applicable to volatile products with suitable vapour pressure.

To obtain good results, there are a few parameters that must be considered; such as the injection amount, the heat at which the injection must be (hotter than the desired product to prevent condensation), the heat and agitation speed once the sample has been loaded into the agitator by the autosampler, and finally the heat of the inlet so that the sample once again does not condense. The inlet also needs to be taken into consideration.

There are three types of injection, split, splitless and direct. A split injection can be considered an 'internal dilution' method, where a ratio is set, *i.e.* 10:1. The rest is then exhausted through a 'split valve'. This prevents the column and detector from being saturated with the sample injected, giving considerably better resolution and no broad peaks or detector overload. This also reduces the risk of damaging the column. A splitless injection is similar; however, the split valve is closed off. Therefore most of the sample goes to the column. This is better for trace sample analysis. Finally, direct injection means directly injecting the total sample amount into the column. This again is very good for trace gas analysis however can very easily overload the column and detector, causing oversized, unresolvable peaks. Each of the three has different inlet liner types, which require changing depending on the application. When it comes to products of CO_2 electroreduction, the preferred injection types are split (with around a 5:1 ratio) or splitless. Direct can often overload the column; however, the products are sometimes in ppm quantities, meaning a direct injection method is required.

3.2.2 High Performance Liquid Chromatography (HPLC)

HPLC is a common method for liquid phase analysis in CO2 reduction research, developed as a method to overcome the limitations of standard liquid chromatography. It is similar to GC because it requires a column packed with an adsorbent material as the stationary phase. The mobile phase in HPLC consists of a polar/non-polar solvent mixture (like the carrier gas of GC). The mixture is altered depending on the sample and the desired separation. The sample components interact differently with the stationary phase and the solvent mixture, leading to different flow rates for each component. The components flow out of the column, and a detector records their order as well as intensity. As with GC, a few detectors can be used, which is not the only variable. There are choices in the columns used too, and the type of analysis that can be carried out.

There are two phases of analysis; normal phase and reverse phase. Normal phase consists of a polar stationary phase and a non-polar mobile phase, and the reverse phase has a non-polar stationary phase and polar mobile phase. Using a reverse phase requires a reverse phase column, and as the polarity of a compound increases, the retention time decreases.

The choice of column is also important. A standard choice for reverse phase HPLC consists of C18 ODS (octadecylsilyl) packed columns. The lengths and packing of these columns are essential as the retention is greatly affected due to this.

3.2.2.1 HPLC Detection methods

Many detectors can be coupled with HPLC. One of the most common detectors consists of UV-vis. A UV-vis detector utilises light in the UV/visible area of the spectrum to analyse the samples upon elution from the column. The compound can be analysed by the amount of light absorbed at different wavelengths. As with the MS, the software now has an integrated library to match and identify the product; however, if this is unavailable, there is UV-vis data online to match and identify products manually. Another common type of detector coupled with HPLC is MS, which works similarly to the GCMS. It gives instantaneous mass/fragmentation analysis of the products eluting from the column with high sensitivity.

3.2.2.2 HPLC for CO_2 electroreduction product analysis

Once again, liquid phase analysis methods are also required due to the range of products and their phases.

The use of HPLC has been reported in most studies where product analysis has been reported. Hashiba *et al.* reported the use of HPLC to find formate in the electrolyte, [62]. In contrast, Hori *et al.* showed that HPLC could detect products such as ethanol and propanol within the post-reduction electrolyte. [36, 101]

3.2.3 Ion Chromatography (IC)

Ion chromatography is an analytical method used to separate and determine ionic and charged species. IC works through the separation of components based upon their charges. This separation occurs due to the interactions of the components to the charged stationary phase. There are two types of stationary phase for IC. Anionic stationary phase columns are known as 'cation exchange' columns as they are coated with an anionic material allowing cationic interactions. A cation stationary phase utilises 'anion exchange' columns and allows anionic interactions.

IC can also utilise a UV detector; however, the most common is a conductance detector, consisting of two electrodes, a sensor cell and a detector. It is essentially a straightforward electrochemical method of detecting products. As the ions pass through the sensor cell, the electrical impedance between the electrodes is altered.

This alteration is recorded and then displayed as a change in conductivity (in microsiemens). To quantify, the area of the peak is taken (microsiemens*minute). The major limitation is that it is only useful for charged species when doing product analysis.

3.2.3.1 IC for CO_2 electroreduction product analysis

Due to three potential products being charged, anionic species (formic, acetic and oxalic acid), IC is an easy and helpful technique to check whether these products have been formed.

3.2.4 Nuclear Magnetic Resonance (NMR)

NMR is a method used for the qualification (and sometimes quantification) of compounds by determining their structure. It is based on the fact that nuclei have intrinsic spin properties and work by applying an external magnetic field (electromagnetic radiation) to the nuclei. This provides it energy to move up to a high energy level. Once the nuclei spin settles to a non-excited state, the input energy is emitted at the same frequency. The emitted signal is then recorded and processed, resulting in an NMR spectrum [102, 103].

3.2.4.1 NMR for CO_2 electroreduction product analysis

Both ^{1}H and ^{13}C NMR have been reported to analyse the structures of products. As the products of CO_2, electroreduction consists of mainly hydrocarbons; both NMR methods are capable of being used for the qualification of products obtained. NMR has always been reported not alone but as part of an analytical process alongside GC, HPLC, MS and other methods. NMR has been generally reported for product qualification; however, quantification has also been conducted. Kuhl *et al*. reported using NMR to measure liquid phase products (formic acid, acetic acid, methanol, ethanol, propanol), as no purification or product separation is required prior, therefore significantly reducing the risk of product loss [47].

3.3 Analysis methods developed

Analysis methods were developed for ECO_2RR prior to conducting work on cell design. To be able to qualify and quantify the products of ECO_2RR, an array of analytical methods was required. The methods were set up over the course of BSc and PhD; however, some methods were not used in subsequent chapters due to equipment errors or time constraints. However, the methods are still established and usable for future work. This chapter does not include the development of OLEMS, as that is in chapter 5.

3.3.1 Standard Solutions

Stock solutions of acetic acid, formic acid, oxalic acid, methanol, ethanol, propan-2-ol, acetone, formaldehyde and potassium hydrogen carbonate ($KHCO_3$) were made up for analysis with IC and NMR. $KHCO_3$ standards were made due to the use as an electrolyte in ECO_2RR.

Each stock solution began at a concentration of 10 gL^{-1} and was then diluted using Milli-Q® ultrapure water. All of the chemicals used were of analytical or HPLC grade and were all supplied to the university by Sigma-Aldrich Company Ltd. All glassware used was Grade A Fisherbrand™ glassware, supplied by Fisher Scientific. Mixtures of the stock solutions were also made, with the concentration of each constituent being carefully calculated to 1 gL^{-1} in the solution. These mixed solutions were then diluted further to samples in the range of 1 to 10 ppm *(note: ppm = parts per million = mgL^{-1})*.

3.3.2 **Ion Chromatography**

IC can be used to identify the charged species in a solution; therefore, the potential products prioritised here were acetic, formic and oxalic acid. Analysis was carried out on a Thermo Fisher Scientific Dionex ICS-5000+. The column used in the experiments was Dionex IonPac AS11 (Thermo Scientific, 250 x 2mm) Anion-Exchange Column. The eluent used in each IC experiment was potassium hydroxide (KOH) supplied by Thermo Scientific for their Dionex EG unit (Thermo Scientific Dionex EGC-KOH). The vials used for each sample were composed of polypropylene (Thermo Scientific).

Application notes supplied by Thermo Scientific for the IonPac AS11 columns were first studied to observe the potential retention times of the analytes in question. All potential products were placed as separate samples (concentration 10 mgL^{-1}) to observe the conditions required to obtain a reasonable retention time for each potential product. Each injection volume remained constant at 10 μL, the flow rate remained unchanged at 0.38 $mLmin^{-1}$, and the anion ratio was kept at 2.47. The eluent concentration and anion suppression were altered accordingly, and the elution time. The suppression is generally calculated and altered, corresponding to the flow rate, eluent concentration and the anion ratio. Equation 3.3.1 shows how the suppression current is calculated.

$$\text{Suppression current (mA)} = \text{Flow rate} \times \text{Eluent concentration} \times \text{Anion ratio}$$

Equation 3.3.1 - Calculation of suppression current for Ion Chromatography

Then, a range of eluent concentrations, suppressor currents, and elution times were tested. It was then concluded that potential products such as acetic and formic acid were eluted first. To obtain a good retention time, it required a very low eluent concentration (1 mM). It was then found that at this low concentration, analytes such as oxalic acid and $KHCO_3$ did not elute in the hour elution time frame. Therefore, they required a higher eluent concentration of between 15-30 mM ($KHCO_3$ ~21 mM, oxalic acid ~25 mM).

After individual tests, mixed solutions were also tested. These mixed solutions consisted of acetic, formic and oxalic acid at a concentration of 10 mgL^{-1} and $KHCO_3$ (0.1 M). Due to the nature of the analytes in this mixture, a 'ramping' method was implemented. This method held the concentration at 1 mM for the first 10 minutes, which was sufficient for acetic and formic acid elution, and then slowly ramped between 10 to 35 minutes from 1 mM to 30 mM. This then allowed the elution of $KHCO_3$ within this ramp. The concentration was then held at 30 mM for 10 minutes, allowing oxalic acid to elute before being dropped to 1 mM for equilibration.

Once this method was established, mixtures of the same components but at different concentrations were then analysed. The range of concentrations studied consisted of a low range (1 to 10 ppm in increments of 2 ppm) and a high range (20 to 100 ppm in increments of 20 ppm). The software used to obtain the data was Thermo Fisher's Chromeleon 7, and this software was able to record and display the data and accurately calculate the peak areas. Therefore, the peak areas of each component were recorded from the software and then plotted against the concentration of the sample to create calibration plots. The calibration plots can be found in Appendix A. The use of the IC was short-lived due to major equipment failure. The equipment was not repaired prior to completion of this work and is therefore not used further to analyse the products obtained in further experiments.

3.3.3 **NMR**

NMR is a powerful tool that can be used to quantify and qualify. However, its application for this project is its ability to detect many of the potential liquid phase products. These include formic and acetic acid, formaldehyde, 2-propanol, ethanol, methanol and acetone.

3.3.3.1 Equipment

The equipment used for this experiment was Bruker's AVANCE III 400 MHz Ultrashield Plus (NanoBay) NMR Spectrometer, fitted with a 5 mm ^{1}H-X broadband observe (BBO, ^{109}Ag-^{19}F) RT probe. The NMR tubes used were Wilmad-LabGlass 527-pp-7 5mm 7" Thin Wall Grade A borosilicate 400 MHz precision NMR sample tubes.

3.3.3.2 Chemicals and sample preparation

As with IC, samples for NMR were also prepared with those products. First, a 'test mixture' of acetic acid, formic acid, formaldehyde, methanol and $KHCO_3$ was prepared and underwent regular ^1H (proton) NMR. Due to the fact that all of these solutions were made in water, this resulted in a dominating water peak between 4-6 ppm. As anticipated, water suppression was required for the analysis of these samples; therefore, subsequent tests used water suppression to omit this prominent peak.

The NMR samples were composed of 540 µL of analyte and 60 µL D_2O. Therefore, the solvent was selected as 90% H_2O and 10% D_2O in the NMR software. The software used for the NMR was Bruker's IconNMR and TopSpin 3.5 pl6. An internal standard of DMSO (anhydrous Dimethyl Sulfoxide, analytical grade, Sigma-Aldrich) was required for quantification, therefore altering the NMR samples to 540 µL of solution and 60 µL 90 ppm DMSO in D_2O. This amount for DMSO was decided after tests were carried out to observe the size of the DMSO peak compared to the others. A 90 ppm concentration of DMSO in D_2O yielded a DMSO peak that was appropriately sized to be used as an internal standard. DMSO was also added to give a better signal:noise ratio. The number of scans (NS) was increased to 64, eventually 128, to obtain a better ratio and better-resolved peaks.

A calibration solution of acetic acid, formic acid, methanol, ethanol, 2-propanol, acetone (1000 ppm) and $KHCO_3$ (0.1M) was prepared and analysed for peak identification.

3.3.3.3 Calibration

Calibration samples were then prepared from the calibration solution. This included 5 samples containing 1 to 10 ppm constituent concentration (increments of 2 ppm) and 5 samples containing 20 to 100 ppm constituent concentration (increments of 20 ppm). These samples underwent analysis overnight, as the number of scans was increased to 128. Each sample was also shaken to eliminate the possibility of a concentration gradient. To eliminate other outside factors and systematic errors, a 5 minute equilibration period was added between analysis and a stability check to ensure the signal is not affected to eliminate other outside factors and systematic errors.

A range of D1 (delay time) and NS (number of scans) were analysed for optimal results. It was found that D1: 5 coupled with NS: 128 delivered optimal results. Analysis of D1 and NS can be found in Appendix A.

The integration of each peak was then set with respect to the DMSO peak (which was set to 1000) in TopSpin, and the integral values for each peak were then recorded. These integrations were then plotted against their respective concentrations to form calibration plots. The calibration plots can be found in Appendix A. This established the method to qualify and quantify the products of ECO_2RR in aqueous solutions.

3.3.4 Gas Chromatography with BID detector (GC-BID)

Using a GC-BID system to analyse all products (gaseous and volatile liquid) of ECO_2RR is possible; however, it is mainly used to analyse the gaseous products obtained in this work. These products include hydrogen, methane, ethylene and carbon monoxide. The GC-BID setup in this work is also on-line, which is beneficial for analysis due to direct input, eradicating the potential product losses faced when transferring to a vial for injection. Furthermore, the analysis can occur during electrolysis, and the products obtained during the experiment can be analysed.

3.3.4.1 Equipment

Products analysis was performed using a Shimadzu Nexis GC-2030 gas chromatography system fitted with a dielectric barrier discharge ionisation detector (BID-2010 plus). Sampling was conducted using a 500 uL gas sampling loop, interfacing the gas injection port with the GC column (ShinCarbon micropacked column ST 80/100, 2m, 0.53 mm ID, 0.74 mm OD, Thames Restek UK). The ShinCarbon column was complimented by an Integra Guard column to prevent any particulates from the column reaching the detector. A custom gas sampling vessel (made with Swagelok parts) was used to calibrate the equipment.

3.3.4.2 Chemicals

Calibration gas (CG) (1000 ppm of hydrogen, methane, ethylene, carbon monoxide, helium balanced) and CO_2 (>99.99%) were purchased from BOC UK. Helium (99.999%), used as a carrier gas for GC column and discharge gas for the BID, was provided by a helium purifier (VICI, Valco Instruments Co Inc., Schenkon, Switzerland) fed from a helium cylinder (BOC, UK).

3.3.4.3 Calibration

GC-BID was calibrated with the use of the CG, CO_2 and custom gas sampling pressure vessel (Figures 3.31, 3.32). The vessel was first evacuated under vacuum and then filled with CG. The CG was then vented to atmospheric pressure before the vessel was evacuated again. To ensure the vessel was saturated, it was also flushed for approximately 1 minute with CG. All tubing associated was also flushed with CG, and the gas sampling loop was flushed with CO_2 to prevent potential contaminants. The vessel inlet was connected to the CG cylinder and CO_2 cylinder directly. The outlet was connected to the GC sample loop inlet, creating a closed system up to the GC to ensure accuracy.

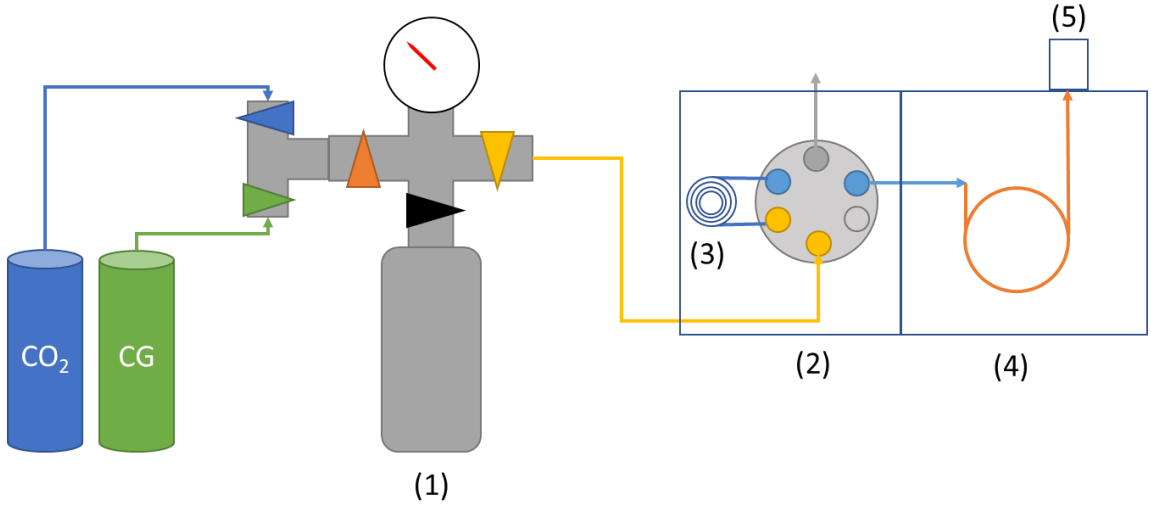

Figure 3.3.1 – Calibration set-up diagram for GC-BID. CO_2 and Calibration Gas (CG) cylinders feed into sampling vessel (1). The mixture is fed to the GC 6 port valve (2), where it fills the 500 µL sample loop (3) before being injected into the main column (4) and being detected by the BID (5).

Calibration plots were obtained by diluting the CG with CO_2. This was done inside the pressure vessel. The vessel was filled to 2 bar with calibration gas and then vented down to 1 bar. The vessel was then filled back up to 2 bar with CO_2, resulting in a 50% dilution (*i.e.* 1000 ppm to 500 ppm). Dilutions to smaller concentrations were completed by venting and adding CO_2 until the desired concentration was reached. A calibration range of (nominal) 15 to 300 ppm was possible with this method. GC parameters can be found in appendix A.

Figure 3.3.2 – Pressure vessel

Error analysis consisted of using the uncertainty of the analogue pressure gauge (± 0.02 bar), as the gauge has increments of 0.1 bar; therefore, intermediate values may be estimated to have an approximate accuracy of 0.2 of each division.

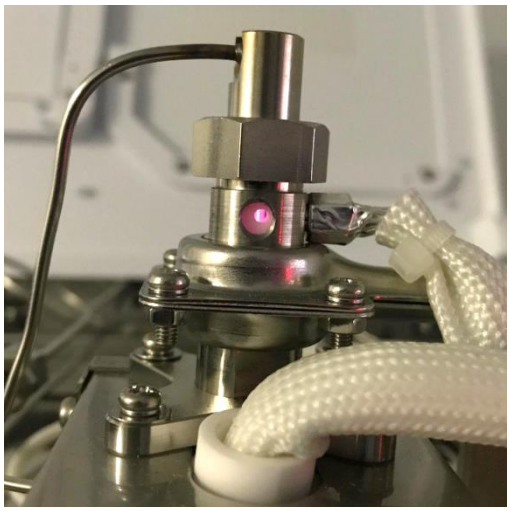

Figure 3.3.3 - Plasma inside BID, window open for inspection.

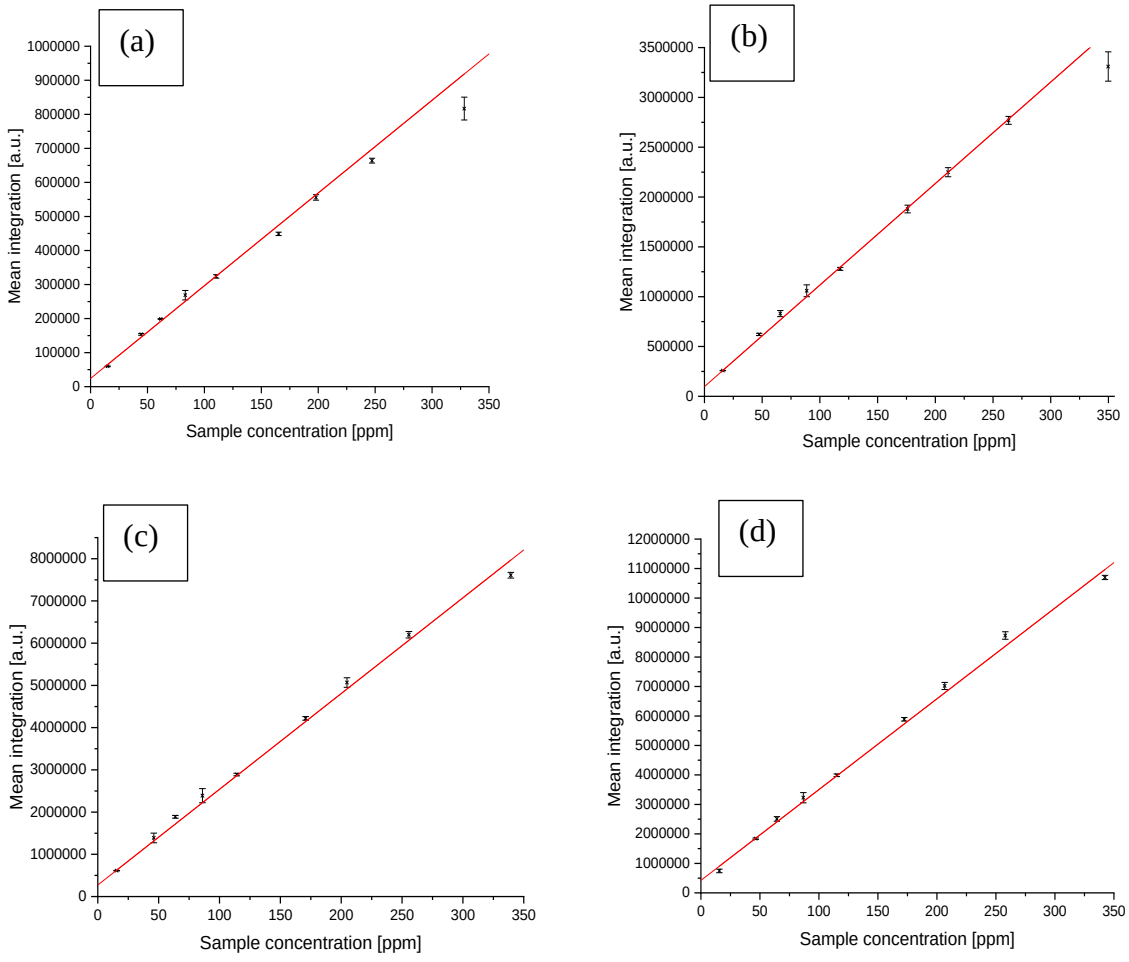

Figure 3.3.4 - Calibration plots obtained for GC-BID. (a) Hydrogen $R^2 = 0.993$, (b) Carbon monoxide $R^2 = 0.998$, (c) Methane $R^2 = 0.997$, (d) Ethylene $R^2 = 0.998$.

The calibration plots shown in Figure 3.3.4 are resultant of triplicate runs of CG. The fitting was seen to have an R^2 value of above 0.99; however, some points are poorly fitted to the line. Due to this, the line of best fit was redone over two ranges, 0-100 ppm and 100-350 ppm. This resulted in a better fit; therefore, the equipment was ready for the quantification of real samples. This calibration was conducted every so often to check for changes, such as with the detector, column or inlet, and to ensure that the quantification was accurate.

3.3.4.4 Quantification and Faradaic Efficiency

Quantification of the gaseous products detected by the GC-BID was conducted by integrating the signal and checking against the calibration plots. To obtain the faradaic efficiencies during an experiment, the moles of gas that can be held in the 500 μL loop (and injected on the column, n_{loop}) were calculated using the equation:

$$\frac{PV}{RT} = n_{loop} \qquad 3.3.2$$

P = 1 atm, V= 0.0005 L, R = 0.0821 L·atm·K^{-1}·mol^{-1}, T = 293 K

The n_{loop} was then divided by one million and multiplied by the ppm value obtained from processing the data using the calibration plots. This resulted in the amount of moles of product, n_{prod}. The theoretical moles were the obtained using:

$$n_{theo} = \frac{Q}{Fz} \qquad 3.3.3$$

Q = Charge, n = moles, F= Faradays Constant (96485 C/mol), z = electrons

The n_{loop} was then divided by the theoretical amount of moles (n_{theo}) and multiplied by 100 to obtain the faradaic efficiency.

3.4 Conclusions

A strong arsenal of analytical methods is required to analyse the vast array of products that ECO_2RR on Cu produces. Robust yet efficient methods are required to be able to analyse the full range of products. In this chapter, the methods historically used are reviewed, and the analytical equipment methods and calibrations established as a basis for ECO_2RR work are discussed. These methods include Ion Chromatography, NMR for liquid products, and On-Line Gas Chromatography with Barrier Discharge Ionisation Detector (GC-BID) for gaseous. Development of DEMS/OLEMS (differential / on-line electrochemical mass spectrometry) was also completed for analysis of dissolved gasses; however, this is discussed in chapter 5, alongside the development of an adaptable reactor cell for use with OLEMS and GC-BID.

4 Electrochemical Formaldehyde Determination

This work was published in 2018.

D. Trivedi, J. Crosse, J. Tanti, A. J. Cass and K. E. Toghill, *Sensors and Actuators B: Chemical*, 2018, **270**, 298-303.

4.1 Introduction

The determination of formaldehyde in complex media is notoriously a challenging process, and finding a simple, selective and effective method of identifying and quantifying formaldehyde in a complex medium is a fundamental issue [58, 104-106]. Formaldehyde is a ubiquitous chemical used in many applications, from the production of chemicals to manufacturing plastics, and can be found in many household products [107]. This means it is present in many areas, such as domestic and industrial workplace air spaces and industrial waste. Due to its presence in industrial waste, it is seen as one of the most common contaminants in groundwater via dumpsite leaching [107-109].

Formaldehyde is also seen as a product of the electrocatalytic conversion of CO_2 to valuable hydrocarbons. Both photocatalytic [26, 110, 111] and electrochemical [41, 90, 112] methods of CO_2 reduction have reported the presence of formaldehyde alongside other products in post-reduction samples when using a variety of catalysts. Other products include methanol and formate, which, like formaldehyde, are water-soluble.

When analysing post-reduction samples, formaldehyde analysis is complex, especially when using analysis techniques such as NMR. It was found experimentally that the formaldehyde peaks interfered with others, such as methanol, making it impossible to qualify whether both are in a sample.

There are many analytical strategies to determine formaldehyde, with a particular focus on gas-phase formaldehyde. When it comes to liquid phase product analysis, the most notable technique is derivatising the carbonyl compound using 2,4-dinitrophenylhydrazine (2,4-DNPH). This compound is known to produce Brady's reagent for qualitative determination of aldehydes and is the reagent specified by the U.S. Environmental Protection Agency [113] for quantitative use with HPLC. The HPLC method consists of using reverse-phase HPLC and requires a long derivatization process [89, 113, 114]; however is one of the most recognised modern methods, obtaining limits of detection of 10^{-10} M (in an optimised system).

There have been recent safety concerns regarding the use of 2,4-DNPH, as it harbours flammable and explosive properties when allowed to dry in poor storage conditions. The consequence of this is that solid reagent is now challenging to purchase.

Another derivatization method focuses solely on a spectrophotometric approach. It is an adapted Hantzsch method, reported by Nash in 1953. [115] This uses the reaction between formaldehyde and acetylacetone, acetic acid and ammonium acetate to form diacetyldihydrolutidine (DDL). DDL is a yellow derivative of formaldehyde with a high extinction coefficient.

Concerning products of CO_2 electroreduction, an electrochemical approach would be preferable due to the complex nature of the post-reduction electrolyte samples. These samples would be unsuitable for chromatographic machinery. Currently, there is a small body of research in the field of formaldehyde determination using electrochemical methods. This research typically uses platinum [116, 117], palladium [118-121] or gold [122] electrocatalysts and are conducted in sulphuric acid or sodium hydroxide solutions. They also use various nanoarchitectures and complex fabrication methods. Detection limits have been reported around 10^{-5} M; however, some palladium electrodes have been reported to determine formaldehyde concentrations as low as 10^{-11} M.[117]

Nickel modified electrodes in an alkaline solution are well-known catalysts for small organic molecules. The Ni(III) species in the oxidised NiOOH reacts with the organic compounds, oxidising the organic analyte, which results in the $Ni(OH)_2$ species being reformed. [123-126] There is a lot of literature that utilises $Ni(OH)_2$ as a redox catalyst for alcohol and glucose oxidation [69, 127, 128], yet only a few on the electrochemical oxidation of formaldehyde. [129-131]

The few have also mainly focussed on large concentrations in fuel cell assessment instead of formaldehyde detection [132]. The nickel catalyst strongly responds to the presence of formaldehyde, as the formaldehyde forms a gem diol in water, and these polyol species are highly responsive to nickel as a catalyst. [126]

This part of the thesis reports a simple, low-cost nickel modified glassy carbon electrode and its application to the determination of formaldehyde with comparison to a spectrophotometric technique.

4.2 Experimental

4.2.1 Reagents and Equipment

Ammonium acetate, acetic acid, sodium acetate and acetylacetone (reagent grade) purchased from Sigma Aldrich (UK) used as received. $Ni(NO_3)_2$ was purchased from Sigma Aldrich (UK). KOH was purchased from Fisher scientific. All solutions were prepared using Milli-Q® ultrapure water (resistivity 18.2 MΩ/cm).

The formaldehyde additions were made with standardised formaldehyde (HCOH) stock solution. HCOH was purchased from ARCOS Organics (37> wt % stabilised with 5-15% methanol). A stock solution of 0.05 M was prepared for use in electroanalytical experimentation using Milli-Q® ultrapure water. The stock was standardised in accordance with the US EPA Method 554 [133].

Anhydrous sodium sulphite (98%) and hydrochloric acid (HCl, 37%) were purchased from Sigma Aldrich (UK) and used as purchased.

To determine formaldehyde in a real-world water sample, a sample of water was obtained from a pond on the university campus. This had been filtered to 0.45 µm and then spiked with a volume of the formaldehyde stock solution.

All glassware was soaked for at least 8 hours in 3M HCl, followed by a triple rinsing of Milli-Q® ultrapure water. All electrochemical measurements were made using an Ivium EmSTAT 3+ (Alvatek, UK) with PSTrace software. The electrodes consisted of the following; glassy carbon working (3 mm ⌀, purchased from IJ Cambria Scientific LTD, UK), platinum wire counter (CH Instruments, purchased from IJ Cambria Scientific LTD, UK), and an Ag/AgCl reference (BASi, Alvatek, UK).

The UV-vis experiments were conducted using a Jenway 7315 Spectrophotometer. The HPLC experiments were conducted with an Agilent 1220 HPLC (Hanover, Germany) fitted with an Agilent Poroshell 120 EC-C18 column (3.0 x 50 mm, 2.7 µm particle size). The HPLC detector was a variable wavelength detector monitoring absorbance at 412 nm. Solvents; acetonitrile (B), water (A).

4.2.2 Electrochemical Method

To fabricate the nickel modified glassy carbon (Ni-GC) electrode, electrodeposition of nickel was conducted at -1.3 V (vs Ag/AgCl) in a 1 mM $Ni(NO_3)_2$ with 0.1 M acetate buffer deposition solution. This was a freshly polished GC electrode, held at potential from 30 to 600 seconds under constant stirring (N_2 atmosphere). Higher deposition times yielded a visible thin metal film across the GC electrode (Figure 4.2.1).

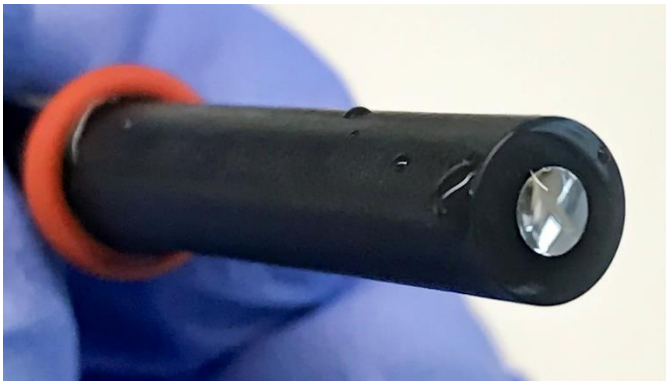

Figure 4.2.1 - Ni plated GC (high deposition time)

Following deposition, the electrode was rinsed with Milli-Q® ultrapure water and then placed in a 1 M KOH solution for conditioning. Conditioning consisted of cycling the electrode between ca. 0.15 and 0.55 V around 250 times at 100 mVs^{-1}. This allowed for the crystalline phases of the $Ni(OH)_2$ to settle into the aged beta phase (ensures that the $Ni(OH)_2$ layer is formed and present in the stable β-crystalline structure) [123-126].

A holding potential of 0.46 V (*vs.* Ag/AgCl) was determined via cyclic voltammetry in the presence of formaldehyde. This allowed a potentiometric calibration plot to be obtained over various linear ranges (Figure 4.2.2, Figure 4.2.3). In a standard three-electrode set up under constant fast stirring, additions of formaldehyde were made to the 1 M KOH at intervals of 20 – 30 seconds. This resulted in a calibration plot based on the average current of the time interval of each addition. The method was then repeated with the formaldehyde spiked pond water.

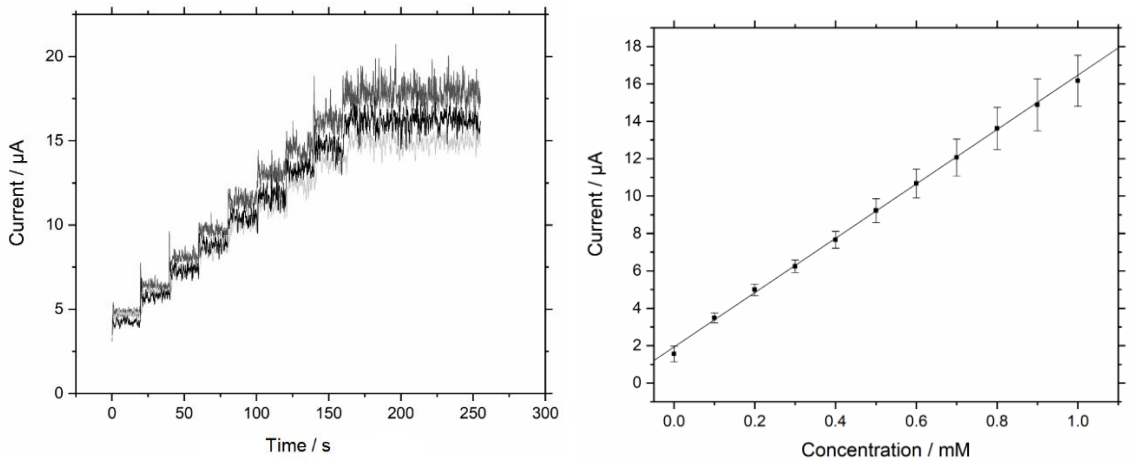

Figure 4.2.2 - Formaldehyde detection n=3 data for calibration over linear range of 0.1 to 1 mM.

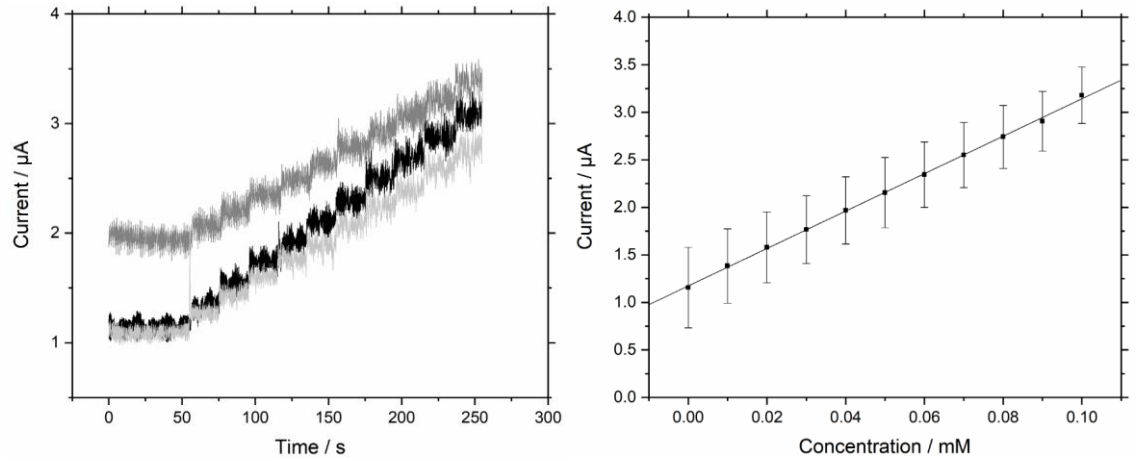

Figure 4.2.3 - Formaldehyde detection n=3 data for calibration over linear range of 0.01 to 0.1 mM

4.2.3 **Spectrophotometric method**

4.2.3.1 UV Detection

A calibration of six points was made via dilution of the 35% formaldehyde stock with Milli-Q® ultrapure water. Aqueous formaldehyde standards were reacted with equal amounts of Hantzsch reagent (15% w/v ammonium acetate, 3% v/v acetic acid and 2% v/v acetyl acetone, heated for 30 minutes in a 40°C water bath, and then allowed to cool to room temperature (20°C) for 30 minutes). This resulted in a yellow 3,5-diacetyl-dihydrolutidine (DDL) solution, analysed with spectrophotometry at 412 nm.

4.2.3.2 HPLC

A portion of the DDL solution was transferred into a GC vial, and a complimentary DDL determination was performed with HPLC. The analysis was conducted with the HPLC detector monitoring absorbance at 412 nm. Solvents; acetonitrile (B), water (A). Injection volume 20 µL.

4.3 Results and discussion

4.3.1 Electrochemical determination

In accordance with the experimental section method, glassy carbon electrodes were modified with nickel to produce Ni-GC electrodes. Optimising the deposition procedure found -1.3 V (*vs.* Ag/AgCl) to be the optimum deposition potential, coupled with a deposition time of 60 seconds. The formation of bubbles on the surface (caused by water reduction) was also avoided to ensure a smooth deposition. Deposition of 300 seconds or more generated a relatively thick film on the electrode surface. Thicker films were less durable during repetitive testing and were found to 'peel' from the surface, possibly under their own weight.

Figure 4.3.1 shows cyclic voltammograms of the Ni-GC during conditioning during the first cycle up to the 250th cycle (every 30th cycle shown).

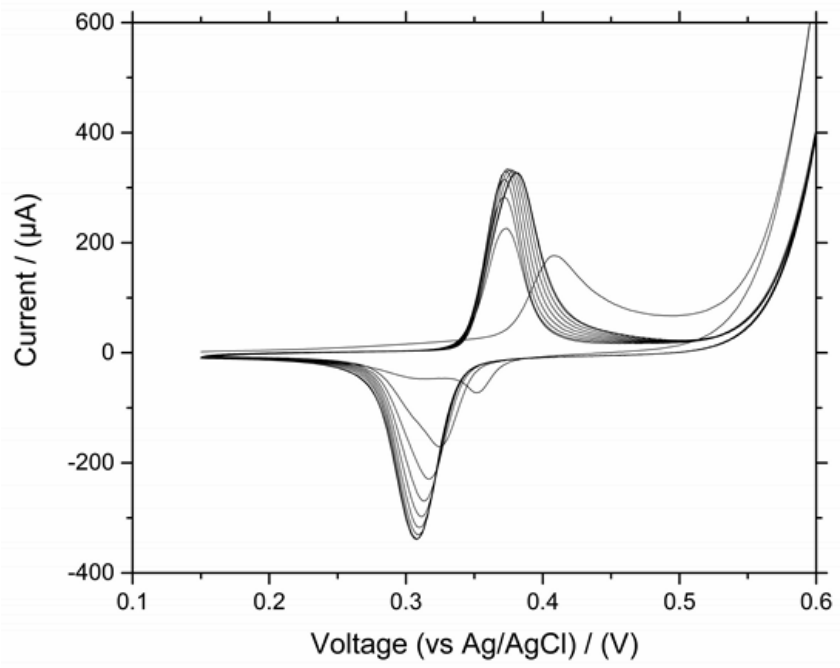

Figure 4.3.1 - Conditioning of a nickel modified glassy carbon electrode for 250 scans in 1 M KOH following 60 s deposition of nickel. Scan Rate: 0.2 V/s. Every 30th scan shown.

It is evident in Figure 4.3.1 that there is an anodic shift and that there is a growth of the broad $Ni(OH)_2$ peak as the nickel oxidises to NiOOH. Over that potential window, the number of cycles ensured that the redox couple was stable and unchanging for the subsequent formaldehyde additions.

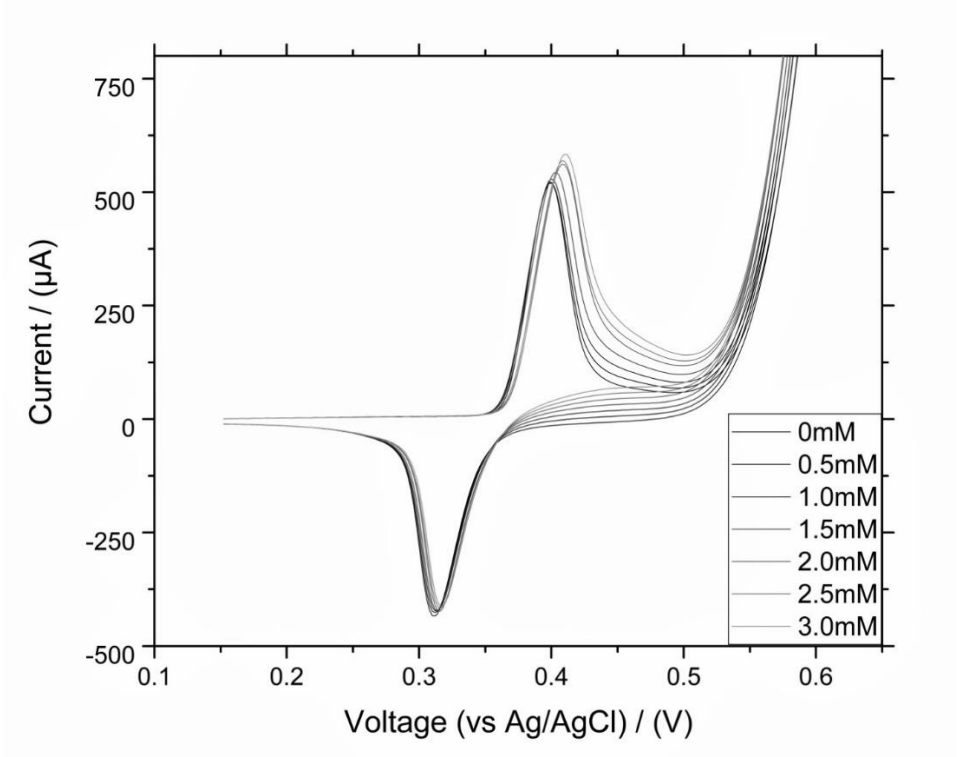

Figure 4.3.2 - Six consecutive additions of 0.5 mM HCHO to a 10 mL 1 M KOH solution. Scan Rate: 0.2 V/s; Electrode: Ni-GC – 60 s.

Figure 4.3.2 displays overlaid cyclic voltammograms taken when 0.5 mM additions of HCHO were made to a Ni-GC cell (in 1 M KOH). It is evident from this that there is an electrocatalytic response to the formaldehyde from the forward scans. The peak potential is seen to shift positively with each addition, but a somewhat linear increasing current response appears after the main peak. A target potential for potentiometric analysis of 0.46 V was then found from this.

Calibration plots were then obtained using a potentiometric staircase method (under constant stirring). Two plots were formed, with a linear range of 0.01 to 0.1 mM (Figure 4.3.3 b) and 0.1 to 1 mM (Figure 4.3.3 a).

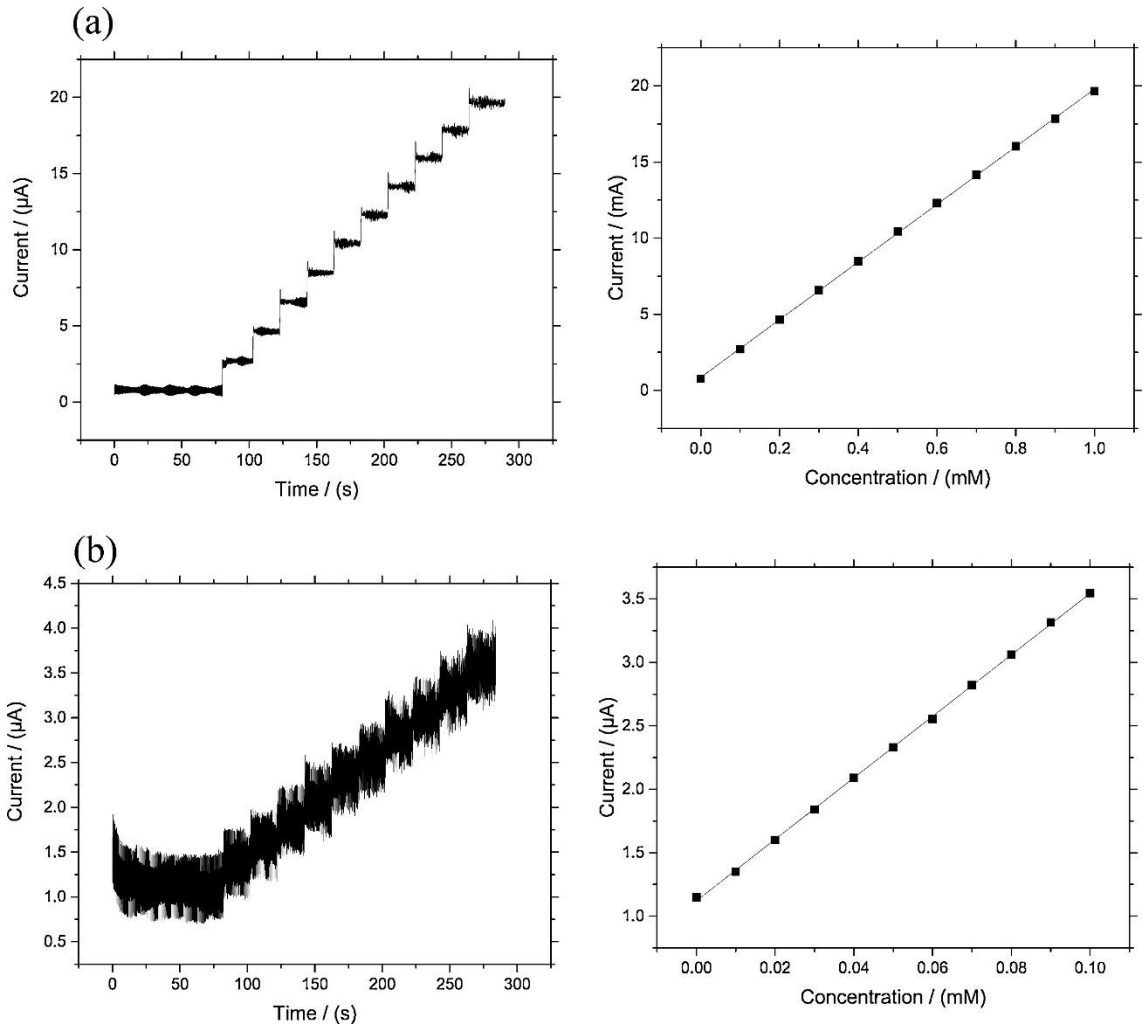

Figure 4.3.3 - Standard additions of formaldehyde under chronoamperometric conditions, using the Ni-GC electrode under constant, fast stirring. a) Additions of 0.1 mM formaldehyde with the calibration plot alongside. b) Additions of 0.01 mM formaldehyde with corresponding calibration plot alongside.

The noise of the current response can be attributed to the convection and the stirrer bar. Alongside each figure are the corresponding point calibration plots obtained by averaging the current response over each addition time interval. Both plots gave a highly linear response (R^2=0.999) with a sensitivity of 19 μA mM^{-1} for the 0.1 M additions and 24 μA mM^{-1} for the 0.01 mM additions. The limits of detection (LOD) for both ranges were (calculated using 3σ [134]) 1.0 x 10^{-5} M.

The detection limit and sensitivity exhibited and obtained in other experiments were of similar magnitude, therefore giving a sensitivity of 22.8 ± 3.8 μA mM^{-1} across both ranges and LOD range of 1.1-1.6 x 10^{-5} M. The Ni-GC was found to be relatively durable, as results were seen to be consistent with repeated use. For repeat use, a simple 20 cycle reconditioning re-established the $Ni(OH)_2$ layers. This reconditioning resulted in a current response equivalent to a freshly plated and conditioned GC electrode. It was also found that the Ni-GC was durable for about 10–15 tests when handled with care.

The sensitivity over the lifespan of the Ni-GC remained consistent, with values around 20 μA mM^{-1}, showing excellent reproducibility. As an extension of the calibration study, the ability to determine an unknown concentration accurately was tested. Using the standard addition method, an aliquot of an unknown concentration sample was added to the reaction cell, followed by a series of known formaldehyde additions Figure 4.3.4 shows an example of this experiment.

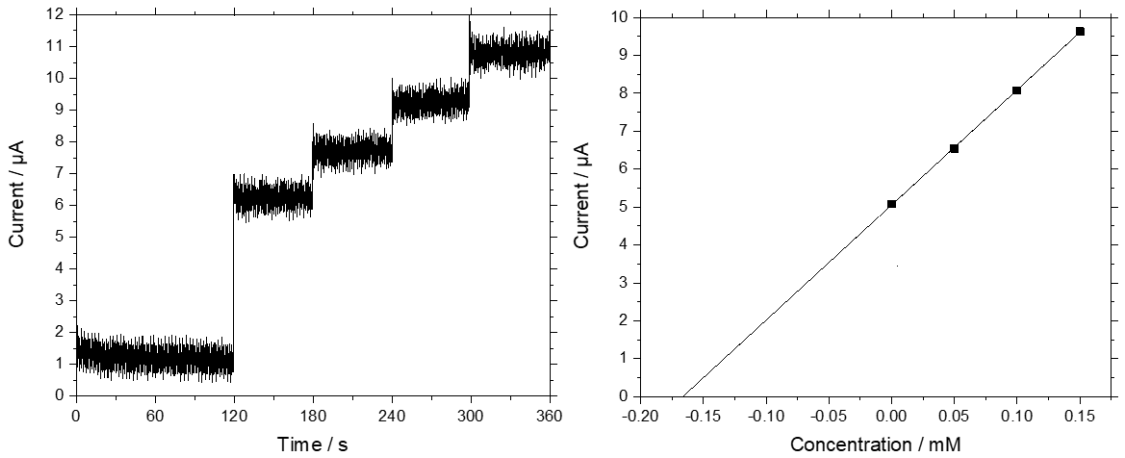

Figure 4.3.4 - Standard additions of formaldehyde under chronoamperometric conditions, using the Ni-GC electrode under constant, fast stirring. Addition of 'unknown' concentration sample of formaldehyde in Milli-Q, followed by three additions of 0.05 mM formaldehyde in Milli-Q water. The modulus of the x-intercept indicates the 'unknown' concentration.

A current vs concentration plot was formed from the potentiometric data, where the current for the 'unknown' addition corresponded to 'zero' concentration. The line of best fit was extrapolated until the X-axis intercept to identify the' unknown' concentration. This modulus of the x-intercept gave the concentration of the 'unknown'.

The 'unknown' in Figure 4.3.4 was 0.18 mM and was calculated using the modulus method to be 0.17 mM. Further 'unknown' concentrations were determined using this method to evaluate the accuracy of the technique with respect to the limit of detection (10^{-5} M).

4.3.1.1 Interface Tests

Nickel modified electrodes are very sensitive to a range of small organic molecules, notable certain alcohols and glucose. Due to this, it was necessary to ascertain the relative sensitivity of the Ni-GC electrode to formaldehyde in the presence of potential interferants. The compounds selected as the interferants in this study were methanol and formic acid. The two were selected as they are potential solution-based products of the electrochemical reduction of CO_2.

In a chronoamperometric study, the potential interferants were added in a similar standard addition manner to the calibration method.

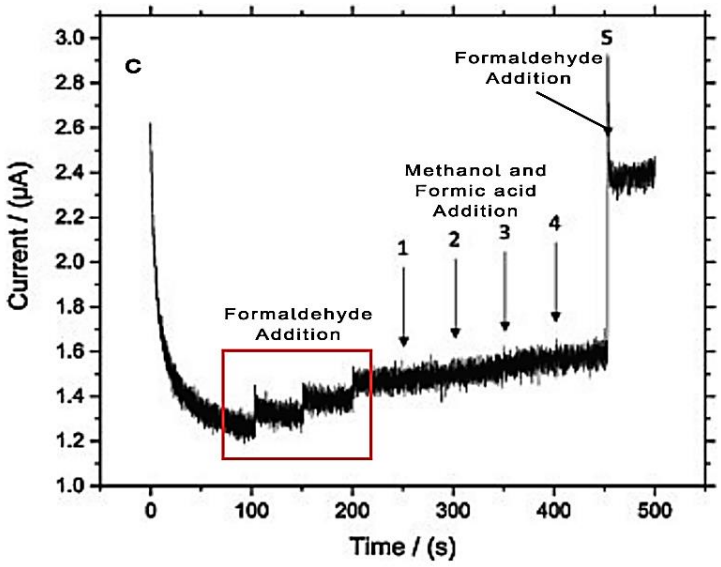

Figure 4.3.5 - The catalytic response of the Ni-GC electrode in 1 M KOH to additions of 0.01 mM formaldehyde at 100, 150 and 200 s, followed by additions of methanol and formic acid. 1–methanol 0.01 mM; 2–formic acid 0.01 mM; 3–methanol 0.1 mM; 4–formic acid 0.1 mM; 5–formaldehyde 0.1 mM.

Figure 4.3.5 shows the results obtained after a series of formaldehyde additions (0.01 mM), followed by methanol and formic acid (0.01 mM) and subsequently formaldehyde (0.1 mM). Whilst not very discernible for methanol and formic acid, the additions were made at 50 second intervals, and a very slight incline in current response can be seen.

This rise in current response is almost negligible compared to the current response for formaldehyde additions. It can be concluded from this result that the Ni-GC demonstrates excellent selectivity towards formaldehyde within potential interferants. It is worth noting that due to the use of highly alkaline KOH as the electrolyte, there is potential for the Cannizzaro reaction to take place [135]. This reaction is recognised as the spontaneous disproportionation of formaldehyde to methanol and formic acid. It is evident in Figure 4.3.5 that the reaction is not taking place in the time scale of the experiment, as formic acid and methanol show no notable response. It may be assumed that formaldehyde is not being altered but only hydrated on the timescale of the analysis. Formaldehyde is also a potential product of ECO_2RR, as are formic acid and methanol. Due to the response of formaldehyde vs methanol and formic acid, this detection method may be utilised to observe formaldehyde in the reduction reaction products.

4.3.2 **Spectrophotometric determination**

The electrochemical approach offers a fast analysis of a post-reaction matrix for the determination of formaldehyde and displays great selectivity; however, it is not 100% selective. A complementary method of assessing formaldehyde is also required to validate. Due to the likelihood of a complex matrix and the extensive pre-processing necessary, the use of the standard 2,4-DNPH method of analysing formaldehyde was rejected for this study. Instead, a more straightforward, more flexible method, which utilizes the Hantzsch reaction, was investigated [115].

The UV spectrum of the derivatized formaldehyde gave a single absorption peak at ca. 412 nm. This was the wavelength used to obtain calibration plots for three sets of formaldehyde. Figure 4.3.6 shows the results of the calibration.

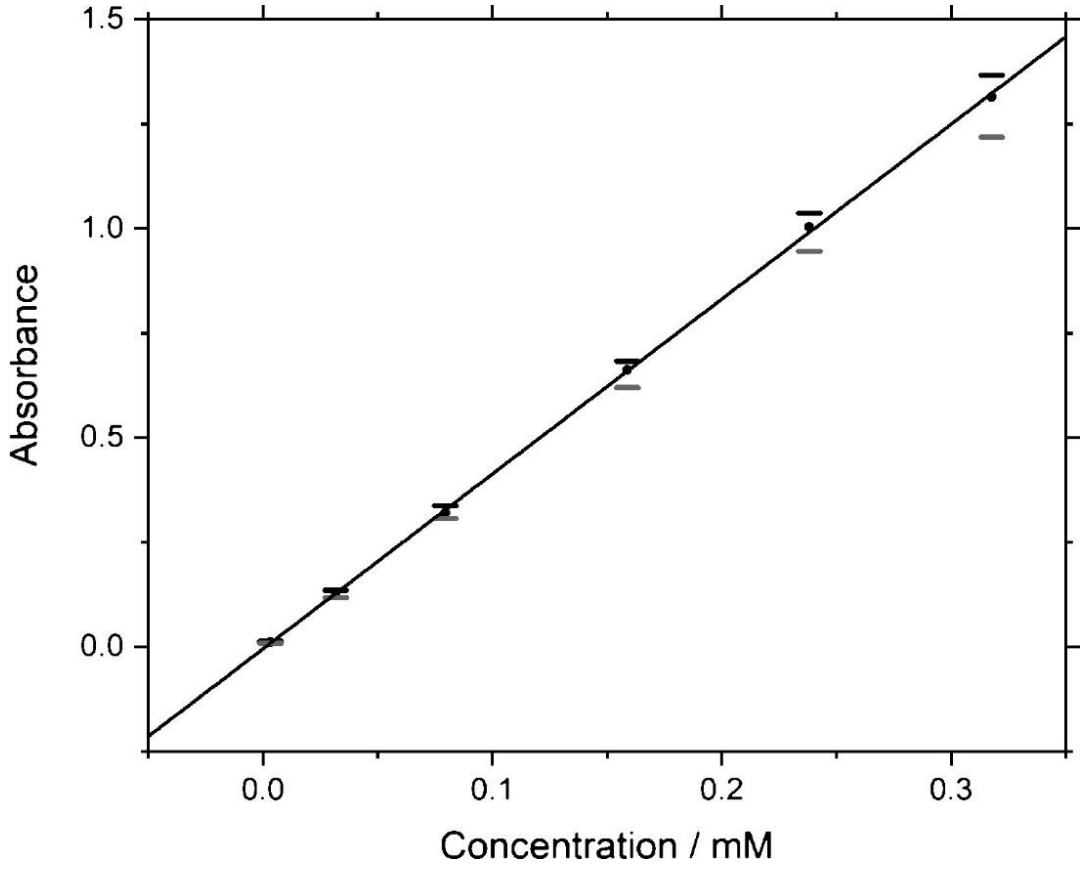

Figure 4.3.6 - UV/vis calibration data for the DDL derivatized formaldehyde where n = 3.

Minimal discrepancy was noted between the three batches, with a near-identical absorbance being observed. The UV/vis spectrophotometry calibration shows a highly linear response to formaldehyde concentrations and a wide linear range of two orders of magnitude (0.1-10 ppm, 0.003-0.3 mM). Instrument precision was measured by analysing the same standard thrice. The standard deviation of the mean of the three samples was ± 0.00%. The calculated limit of detection for this method was 6×10^{-6} M, but the lowest observable standard was 3×10^{-6} M (0.1 ppm). The calibration was tested again using three aqueous formaldehyde samples independently made up of the operator. Mean accuracy was found to be 99.34%. Furthermore, the Hantzsch reagent is not reactive to potential interfering species (methanol and formic acid).

Based on the UV/vis method, the extinction coefficient was found to be 0.1434 L mol^{-1} cm^{-1} (this is the slope of the line of the calibration). The extinction is the molar absorptivity of a sample, which relates to the sample's ability to absorb light at a specific wavelength. The extinction coefficient is directly proportional to the absorbance and is a physical property of the molecular bonding of the sample. At a specified wavelength, the extinction coefficient for the molecule will always remain constant.

4.3.3 **Comparison of both methods with a real-world sample.**

In this study, both electrochemical and spectrophotometric methods were used for the determination of low formaldehyde concentrations in complex matrices. In 0.1 M potassium hydrogen carbonate ($KHCO_3$, a typical electrolyte for the electrochemical reduction of CO_2), a volume of formaldehyde was added. Standard additions of this solution found a negligible difference in the determination of formaldehyde when compared to analysis in Milli-Q® ultrapure water. The spectrophotometric method determined the formaldehyde concentration with a 0% error too.

A subsequent experiment consisted of observing the quality of analysis when it came to naturally occurring water sources. This experiment used filtered pond water obtained from a stagnant pond on the campus grounds. The water first went analysis as received (with no spiking), and no formaldehyde was detected. It was then spiked with 10 mM formaldehyde. The standard addition method was then carried out with this too. The first addition was an ‘unknown’ amount of pond water formaldehyde, followed by three additions of known concentration formaldehyde in Milli-Q® ultrapure water. Figure 4.3.7 shows one of the plots obtained when this experiment was conducted.

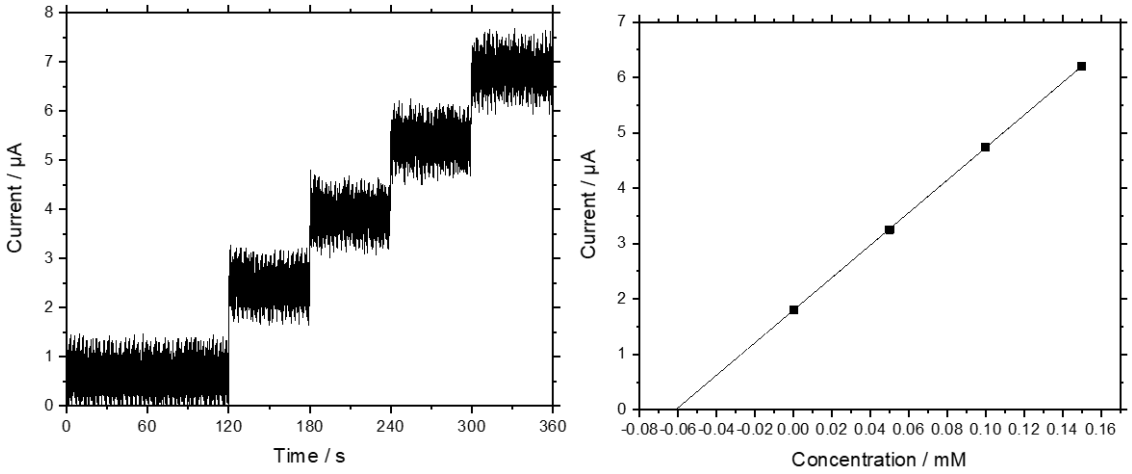

Figure 4.3.7 - Standard additions of formaldehyde under chronoamperometric conditions, using the Ni-GC electrode under constant, fast stirring. Addition of 'unknown' concentration sample of formaldehyde spiked pond water, followed by three additions of 0.05 mM formaldehyde in Milli-Q® ultrapure water.

The 'unknown' concentration was 0.06 mM. Extrapolation of the line of best fit gave an intercept of -0.06, therefore showing the accurate determination of the 'unknown' calculation. In fairness, the 'unknown' addition was made independently to the operator. Further analysis in the pond water matrix found a typical percentage error of zero; however, some tests gave an error up to 12.5%. Table 4.3.1 displays the errors associated with experiments conducted for this study (* w.r.t limit of detection).

Table 4.3.1 - Errors associated with formaldehyde determination (* w.r.t limit of detection).

Technique	Sample Matrix	Unknown added (mM) *	Concentration Determined (mM) *	Percentage Difference (%)
Electrochemical	Milli-Q® ultrapure water	0.05	0.05	0.0
		0.08	0.07	12.5
		0.10	0.10	0.0
		0.18	0.17	5.5
		0.25	0.22	8.0
	HCHO in Pond water	0.01	0.01	0.0
		0.02	0.02	0.0
		0.04	0.04	0.0
		0.05	0.05	0.0
		0.06	0.06	0.0
Spectrophotometric	Milli-Q® ultrapure water	0.0033	0.0033	0
		0.0033	0.0033	0
		0.0333	0.0313	6
		0.0333	0.0313	6
	HCHO in Pond water	0.0033	0.0033	0
		0.0033	0.0033	0
		0.0033	0.0033	0
		0.0333	0.0333	7
		0.0333	0.0333	7
		0.0333	0.0333	7
		0.0166	0.0153	8
		0.0166	0.0157	6

Comparative analysis was made using the spectrophotometric technique. As the UV/Vis analysis required a single point measurement of absorbance compared to the calibration plot obtained, there are no presentable results. Table 4.3.1 gives a summary of the results obtained. The error between the measured and expected concentration was generally 0%; however, some had a 6-8% error. It is worth noting that the spectrophotometric technique was operated at an order of magnitude higher accuracy than the electrochemical method, owing to each approach's difference in detection limit.

Concerning the pond water analysis, the main reason it was carried out was to test whether either method was affected by interference from chlorophylls or dissolved organic carbon (DOC). DOC, for example, appears yellow/brown, and analysis to detect it is often done at 254, 278 and 340 nm. It was also a test for whether DOC or any other compounds affected the Hantzsch reactions in any way. The results show no evidence of any other water chemistry on the measurable formaldehyde concentration and that further additions of formaldehyde were unaffected. It can be said that this particular real-world, contaminated water sample does not have any effect on formaldehyde concentration. Should the pond water have been compromised in colour, there would be issues using the spectrophotometric analysis method.

It should be acknowledged that a set of experiments were carried out where the glassware was not acid-washed prior, thus unsuitably prepared. This gave errors when using the spectrophotometric method of up to 80%, whereas the electrochemical method did not require extensive cleaning or equipment preparation to obtain accurate results.

4.4 Conclusions

This work presented the application of a nickel modified glassy carbon electrode (Ni-GC) to the electrochemical determination of formaldehyde in aqueous solutions. The limits of detection were typically in the order of 10^{-5} M. This detection limit is comparable to other electrochemical systems for formaldehyde determination. This was highlighted with accurate determination of 'unknown' formaldehyde concentrations.

Methanol and formate showed slight electroactivity towards the NiOOH catalyst species; however, the response was negligible compared to the formaldehyde, even when in a 1:10 ratio with the potential interferants.

A spectrophotometric technique was also carried out and resulted in consistent low detection limits of the order of 10^{-6} M. The approach was suited to analysing formaldehyde in a wide range of media. Low concentrations were very responsive to the derivatization method, yielding reproducible responses. The extinction coefficient for the derivatized formaldehyde led to sensitive and accurate determination of unknown concentrations after a rapid confirmatory calibration of the UV/Vis spectrophotometer.

5 Adaptable Dual Stage Flow Cell with On-line Electrochemical Mass Spectrometry (OLEMS).

5.1 Introduction

When conducting electrochemical conversion reactions, one of the most essential parts is product detection. The products obtained help determine whether catalysts, electrolytes or reaction conditions are sufficient for the desired conversion reactions. When it comes to product analysis, the most common method is to conduct the chemical reaction first and then analyse the electrolyte and gas samples post-electrolysis using a suite of equipment including gas chromatography, spectrometry and NMR. This is known as off-line analysis. One of the biggest problems faced with this sort of product analysis stems from the fact that chemicals decompose, gasses escape, and therefore partial loss of sample is frequently encountered. To eliminate these potential product losses, on-line analytical methods have been developed. The instantaneous detection of electrochemical reduction products helps eliminate product loss but also assists in elucidating catalytic mechanisms at defined points in reactions.

Mass spectrometry (MS) was one of the first spectroscopic techniques adopted for on-line electrochemical analysis. The potential for MS was first demonstrated in 1971 by Stanley Bruckenstein and R. Rao Gadde using a porous electrode for *in-situ* mass spectrometric determination of volatile reaction products. Gaseous products were collected in a vacuum system before using electron impact (EI) MS for detection.[136] Further advances came in 1984 with Wolter and Heitbaum [137], who refined the method. Their method continued using a porous Teflon membrane coated with an electrocatalytic lacquer as the interface to the MS.

Their work notably improved the vacuum system; they lowered the time constant, allowing on-line detection of volatile electrochemical reaction products directly related to the polarisation of the electrode. This refinement in design incorporated a vacuum system with two differential pumping stages. This dual-stage setup reduced the delay time and enabled the measurement of the rate of product formation as a function of electrode potential.

The result was that the signal from the MS became proportional to the rate of formation instead of the accumulated product, thus distinguishing this technique from post-reaction product sampling.[138] From the beginning, this method has demonstrated a high level of sensitivity. It has been found to detect desorption products corresponding to approximately one monolayer of adsorbed species at porous electrodes.[139] Instantaneous analysis of electrochemical reaction products can be said to make the whole process more efficient, therefore, more time can be spent on developing the electrochemistry further to industrial applications or even down to 'electrochemistry-on-a-chip'. Electrocatalytic reactions represent the largest field of application when it comes to DEMS systems.[140] These studies are often associated with fuel cell research and wastewater remediation,[141], however it is increasingly being used for analysing the products of CO2 reduction.138, 140, 142, 143 On-line analysis of products resultant of electrocatalytically reduced CO_2 can save hours as well as prevent product loss between electrochemical and analytical techniques.[144] The principle of DEMS has remained relatively consistent; however, upgrades have been made over time to ensure better two-stage vacuum and better detection. Historically, DEMS systems for the second pumping stage (containing the MS) have always used turbo-pumps; however, diffusion pumps and rotary vane pumps have been used for the first stage. Otherwise, the sensitivities of detectors have seen to evolve with technology. However, the main part that has evolved is the design of the electrochemical cell, as there have been multitudes of DEMS cells over the years to obtain good efficiency both faradaic and in terms of product collection. [140]

5.2 Principles of Operation

A DEMS system combines electrochemical half-cell experiments with MS, enabling the on-line mass-resolved analysis of volatile or gaseous reactants, reaction intermediates, and products. Matching the faradaic electrode current with respective mass ion currents, electrochemical reaction processes that are otherwise ambiguous can be made somewhat clearer. [140] Figure 5.2.1 displays a basic representation of a DEMS system.

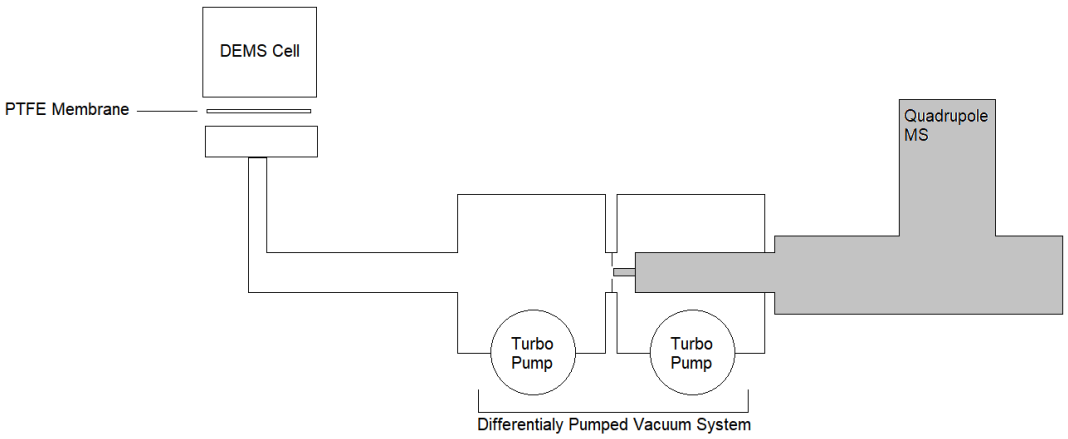

Figure 5.2.1 - Basic representation of DEMS system

The DEMS instrument of multiple essential components. The electrochemical reaction cell, a vacuum system which contains a quadrupole mass spectrometer (QMS), an ion source (usually electron impact), a Secondary Electron Multiplier detector, and a PTFE membrane interface (pervaporation membrane). The PTFE membrane is microporous and partitions aqueous electrolyte from the high-vacuum conditions. It is hydrophobic, preventing any aqueous electrolyte passing through, but allows volatile, non-polar and dissolved gas species to permeate and evaporate into the vacuum. Those, which are able to permeate, can then be analysed with the MS system. The differential name stems from the differentially pumped vacuum system required for the high vacuum conditions.[140]

For a DEMS, the most adaptable and flexible part of the system is the electrochemical cell. Over the decades, there have been multiple designs and evolutions of DEMS cells, each adapted to the electrochemical studies taking place. These variations include electrodes, reactor sizes, materials and configurations. Some have inspired and have been roots of design evolution, such as Wolter and Heitbaum's 'classic' cell,[137] and thin-layer DEMS cells. The 'classic' cell consisted of working electrodes mounted upon membrane material (sputter coated on to PTFE membrane), which a stainless-steel frit would then support. The advantage of this was that response time was less than 100 milliseconds.

Electrocatalyst research eventually began to move away from the powdered electrode materials which were used on these porous electrodes, towards single and polycrystalline electrodes.[140]

Thin-layer DEMS cells were first introduced in 1990, enabling DEMS study of polycrystalline and single-crystal electrodes[140, 145]. In a thin-layer DEMS cell, the working electrode is separated from the membrane interface, and the thin-layer is composed of electrolyte. This enabled flexibility in choice of catalyst and electrodes used for DEMS study. A design by Hartung and Baltruschat placed the counter and reference electrodes externally of the cell, connected by capillaries to the thin-layer cell containing the working electrode.[145] Inherently, the change resulted in longer delay times, but collection efficiency was still comparably high. Using this cell also avoided the process to prepare porous membrane electrodes, and improved versatility for working electrodes that could be studied.

Limitations faced by this cell however include diffusion of reaction products across the electrolyte layer. The diffusion to the membrane depending on the reaction can compete with the electrolyte flow of the cell. This therefore results in reaction products being flushed out of the cell before reaching the membrane. Another drawback was that reactants in gaseous form could enter the cell and then evaporate through the membrane before reacting with the working electrode. This was possible as the thin layer had no direction towards only the working electrode, and there is no physical separation in between. To address this issue, the Dual Thin-Layer Flow Cell was developed. [137, 140, 146]

The Dual Thin-Layer flow cell separates the working electrode and membrane into chambers, where only reactants have contact with the working electrode. Products are carried with the electrolyte stream to the membrane (pervaporation) chamber, before the electrolyte leaves the cell. This cell design is better suited for continuous reactions; therefore, reactions such as ECO_2RR can be conducted well. The nature of the cell however means that component parts are minuscule and challenging to use.

In this chapter, the use of a thin-layer dual cell is discussed and compared with the use of a standard flow cell in conjunction with a pervaporation chamber. The approach adopted in this chapter is considerably more user-friendly and versatile, yet the performance directly comparable.

5.3 Instrumentation and Experimental

5.3.1 DEMS Equipment

The DEMS equipment consists of a HPR-40 DEMS Dissolved Species Gas Analysis system supplied by Hiden Analytical. This is a pre-built piece of equipment consisting of the following parts:

- HAL 201 RC Quadrupole (Mass Filter) Mass Spectrometer with Faraday Cup and Secondary Electron Multiplier detector.
    - 125 mm single filter with 6 mm rod diameter. Open Ion Source. Oxide coated Iridium Filament material. 200 amu mass range.
- Sample Inlet Controller
- Vacuum Control Unit
- Process Indicator Unit
- Scroll Pump

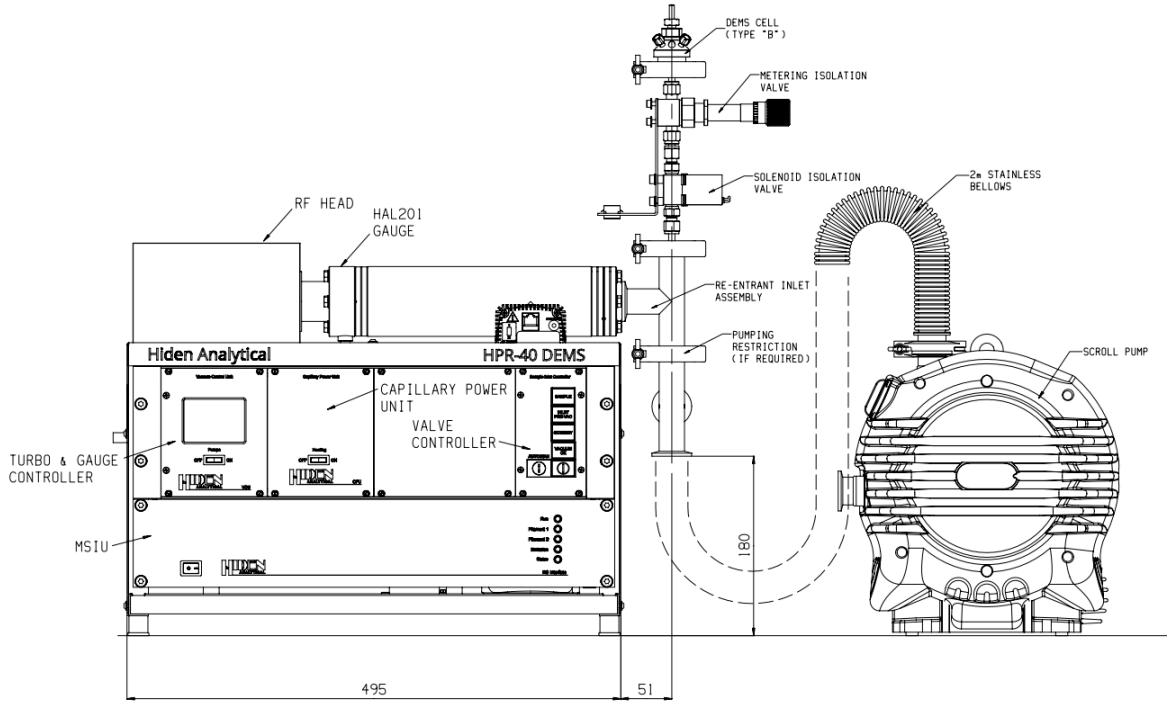

Figure 5.3.1 - Hiden HPR-40 DEMS system diagram - Image property of Hiden Analytical Ltd.

5.3.2 **Mass Spectrometry and Product Detection**

Mass spectra were obtained using the Hiden HPR-40 dissolved species DEMS system, coupled with MASsoft 10 software. For the ionisation of all species, an electron energy of 70 eV was used, with an emission current of 500 μA. The acceleration voltage of Hydrogen ions (m/z = 2) was set to 0.2 V, while the voltage for methane (m/z = 15), ethylene (m/z = 26) and ethanol / 1-propanol (m/z = 31) ions was set to 3 V. This maximised detector response, while ensuring that hydrogen does not saturate the detector, but was also detectable. Higher than 0.5 V caused there to be a zero-response due to hydrogen saturation. Each species was detected using the secondary electron multiplier (SEM), with a detector voltage of 1200 V.

5.3.3 **DEMS Calibration**

Calibration of hydrogen, methane, ethylene and carbon monoxide was carried out using 1000 ppm calibration gas (CG) containing each constituent balanced in helium (BOC Special Products, UK). The CG was introduced to the catholyte stream upon entry of cell for 10 minutes at defined flow rates. The convention for the calibration consisted of fixing the amount of time CG is introduced, and altering the flow rate to match the amount of gas introduced.

For example, CG flowed into the cell at 2 mL/min for 10 minutes, which would mean 10 mL of 1000 ppm CG was introduced. The average MS response for m/z = 2, 15, 26 and 28 over the 10 minutes was then recorded.

Calculation of the moles of gas was conducted by first obtaining the litres of gas passed (L_p) at the defined flow rate in 10 minutes, and then with use of the ideal gas law, the number of moles overall were found.

$$n = \frac{p * L_p}{R * T}$$

Equation 5.3.1 - Ideal gas equation to calculate number of moles of gas for calibration. P = 1 atm, T = 293 K, R = 0.0821 L atm K^{-1} mol^{-1}.

Once the moles of gas for each flow rate were obtained, the moles of each constituent were then calculated. The CG was supplied with a certificate of true concentrations for each constituent in ppm. This was divided by one million, and then multiplied by the calculated total moles of gas.

The moles of each constituent were then plotted against the integrated area of the MS response obtained. Figure 5.3.2 to Figure 5.3.5 show the calibration graphs. Due to the nature of gaseous product analysis, the linearity of the plots are affected. Each plot however still has an R^2 value of above 0.9.

As a note, and for future work, more extensive calibration of the DEMS equipment may be required. This calibration was conducted with electrolyte present, however further calibration in the absence of electrolyte may be required to evaluate the differences. The difference in quantitative analysis when electrolyte is present and absent is due to the different solubility of each species. This therefore introduces limitations as the results can be affected up to 15%, however the membrane requires a liquid interface to maintain vacuum.

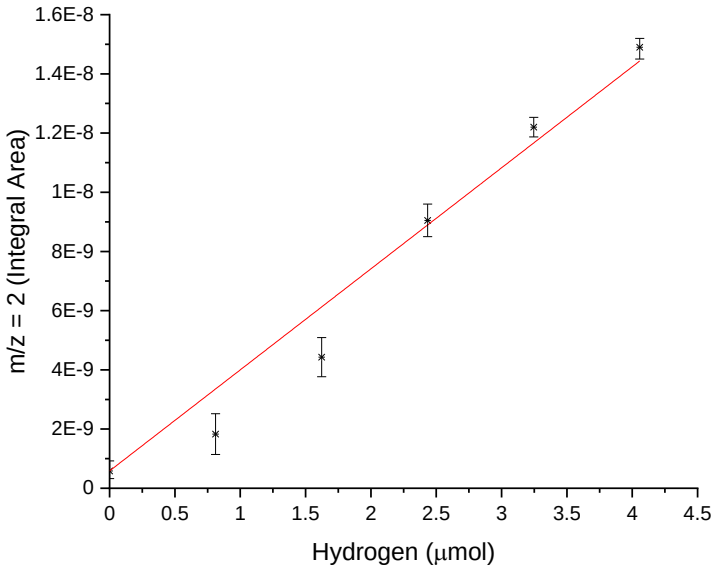

Figure 5.3.2 - MS Calibration plot obtained for hydrogen (m/z = 2). Integrated area of signal response plotted against calculated molarity of gas flowed into the cell over 10 minutes. R^2 = 0.966

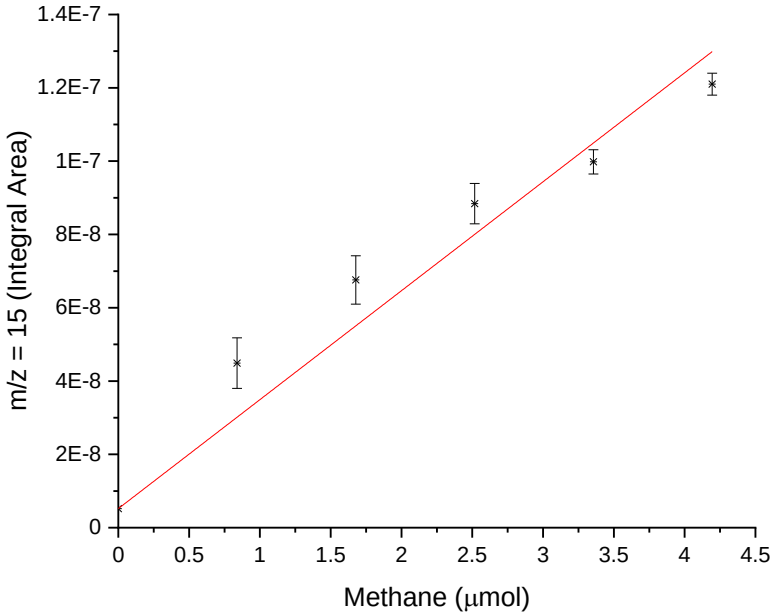

Figure 5.3.3 - MS Calibration plot obtained for methane (m/z = 15). Integrated area of signal response plotted against calculated molarity of gas flowed into the cell over 10 minutes. R^2 = 0.936

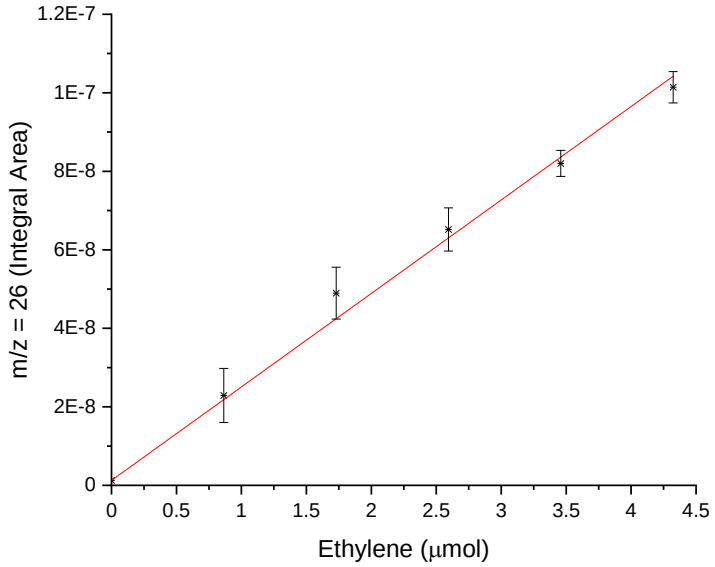

Figure 5.3.4 - MS Calibration plot obtained for ethylene (m/z = 26). Integrated area of signal response plotted against calculated molarity of gas flowed into the cell over 10 minutes. R^2 = 0.993

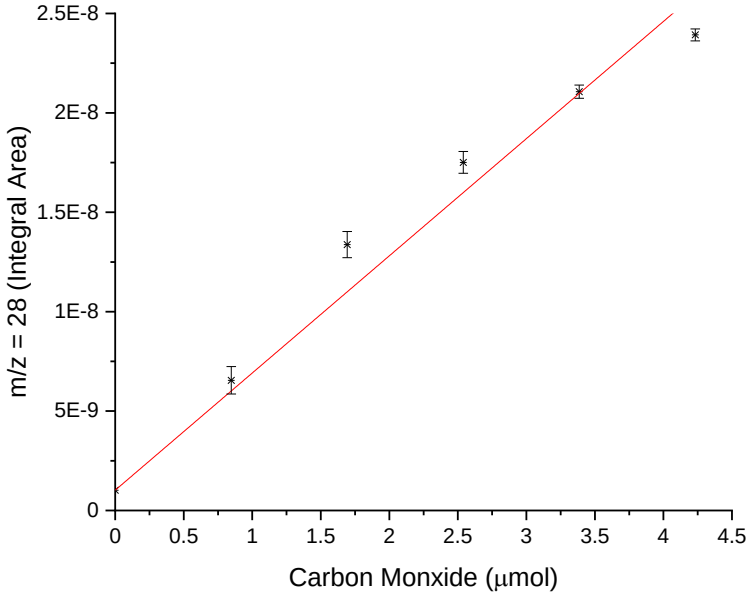

Figure 5.3.5 - MS Calibration plot obtained for CO (m/z = 28). Integrated area of signal response plotted against calculated molarity of gas flowed into the cell over 10 minutes. R^2 = 0.967

5.4 Commercial DEMS Cell

A dual thin layer flow cell was provided with the DEMS equipment upon setup.[147] This ready-made commercial flow cell provided a good entry and starting point into *in-situ* MS for electrochemical CO_2 reduction. To better understand the inner workings of the cell Figure 5.4.2 and Figure 5.4.3 show a 3D rendering of the cell and a cross sectional diagram of this. It can be seen how the cathodic chamber is solely interacting with the DEMS inlet and not the anodic. The reference electrode intersects the catholyte inlet. The working electrode in this cell consists of a copper ring, and the electrolyte enters through the centre of this ring, leaving from four capillary channels (not shown) in its periphery. These four channels then lead to the pervaporation membrane chamber, where vapours pass through to the DEMS.

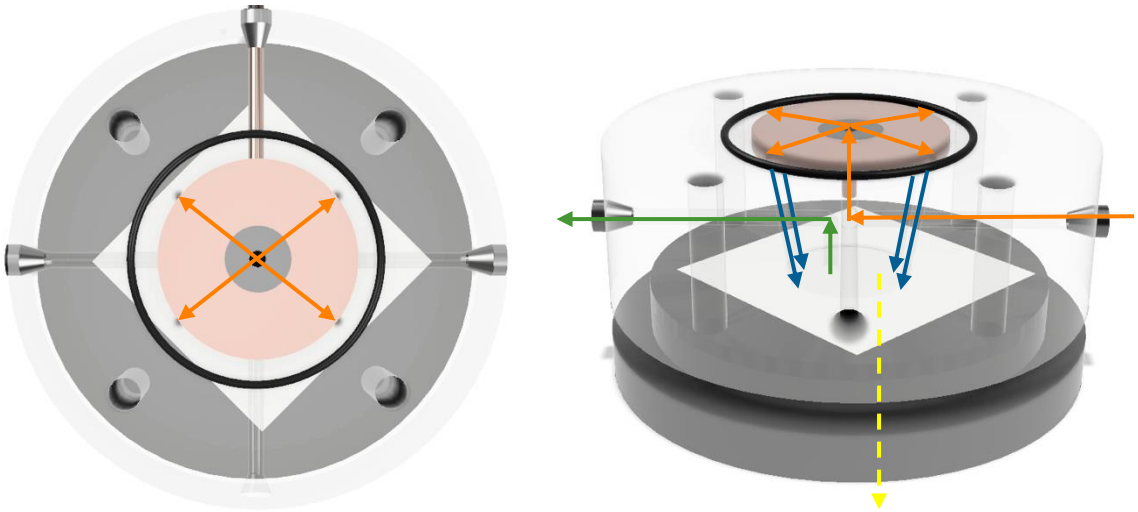

Figure 5.4.1 - Cathodic electrolyte flow diagram. CO_2 sparged electrolyte enters cell (orange) and radially passes over ring electrode. Products (blue) are carried down to the pervaporation chamber, where products can pass the PTFE membrane to DEMS (yellow dashed). The electrolyte then exits the cell (green).

Figure 5.4.2 - 3D rendering of cell

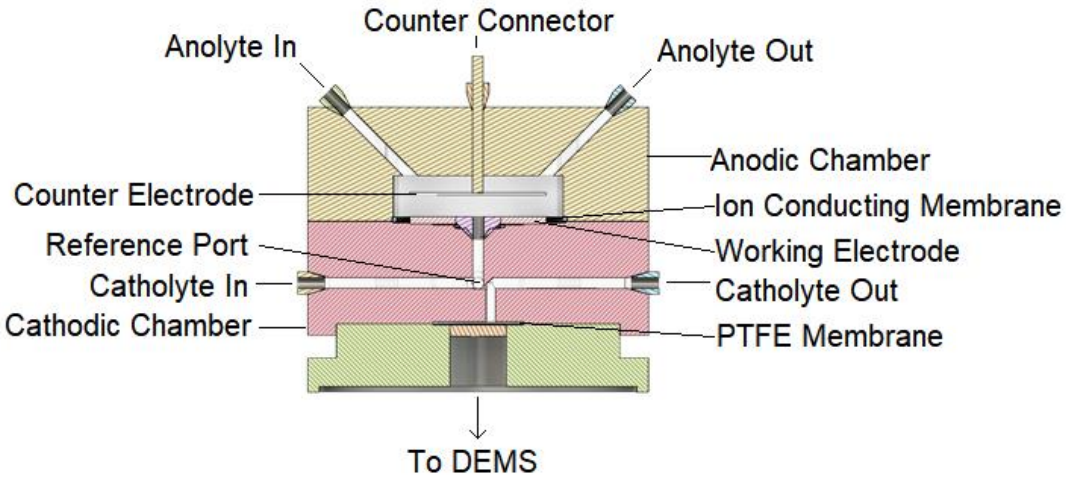

Figure 5.4.3 - Cross-section of DEMS cell

The DEMS dual-cell was supplied by Hiden Analytical and engineered initially by a group at Lawrence Berkeley National Laboratory (Berkeley, California).[147] This cell was made up of three chambers. The counter electrode chamber housed a platinum gauze disk (20 x 20 mm, 82 x 82 wires/inch, 99.9% Sigma-Aldrich, surface area 2 cm^2) counter electrode. The volume of this chamber was 710 µL (0.71 mL). The counter electrode was connected using platinum wire (99.9% Sigma-Aldrich) via a hole at the top of the chamber, allowing contact with the mesh. The counter electrode was flame annealed prior to each experiment. This was located above the working electrode chamber to achieve a parallel electrode configuration.

An ion-exchange membrane (Nafion 110, Ion Power Inc.) separated the counter and working chambers. The surface area of the membrane was approximately 1.75 cm^2.

In the working electrode chamber, catholyte entered via the centre of a PEEK screw, which held a washer-shaped copper electrode (supplied with cell, machined from a copper sheet, 99.9%, Sigma-Aldrich, surface area 1 cm^2). The copper electrode was polished mechanically with diamond polishing compound (Buehler MetaDi Supreme Polycrystalline Diamond Polish, 3 µM) to a reflective finish, then sonicated in isopropanol (30 minutes) and Milli-Q water (30 minutes) prior to each experiment. The volume of the working electrode chamber was 23 µL (0.023 mL), and separated the working electrode surface and the ion-conducting membrane with a layer of electrolyte approximately 130 µM in thickness. The electrolyte flows radially over the surface of the electrode out towards four transfer capillaries.

The working electrode was held in place with a mounting screw, which was hollow to allow electrolyte to flow through, while centrally holding the working electrode down. This screw was also sonicated with the working electrode. The reference electrode ('leak free' Ag/AgCl, 1 mm O.D., Innovative Instruments Inc.) intercepted the inlet stream as it entered the cell.

Transfer capillaries (0.5 mm in diameter, 1 mm in length) transferred the catholyte to a collection chamber. The collection chamber was the third chamber and brought the catholyte to contact with the pervaporation membrane. The polytetrafluoroethylene (PTFE) pervaporation membrane (20 nm pore size, 0.5 cm^2 surface area, Hangzhou Cobetter Filtration Equipment Co. and Pall Corporation, UK) separated the mass spectrometer inlet from the liquid catholyte, only allowing vapours to pass. The volume of this chamber was 5.5 µL.

The working electrode chamber was fabricated using PEEK (polyether ether ketone), and the counter electrode chamber was fabricated using polycarbonate. Each chamber and outlet was fitted with Viton O-rings.

5.4.1 **Electrochemistry**

In accordance to the publication associated with this cell [147], a K_2CO_3 (0.05 M, 99.9%, Fisher Chemical) electrolyte solution was prepared in Milli-Q® ultrapure water (18.2 MΩ deionized water).

When saturated with CO_2, the steady-state pH of the electrolyte was 6.8, making it chemically equivalent to a CO_2 saturated solution of 0.1 M $KHCO_3$ (at 25°C). $KHCO_3$ (0.1 M, Fisher Chemical) was also used for flow cell experiments down the line.

All electrochemistry was conducted using an Autolab (Metrohm, UK), and a Bio-Logic SP-300 potentiostat (Bio-Logic Science Instruments SAS, France). Before each experiment, the applied potential to the working electrode was swept from open circuit potential (OCP) to -1 V (*vs.* Ag/AgCl) at 50 mVs^{-1} to reduce the native CuO_x layer.

A negative system was utilised, pulling the electrolyte through the cell at 1 mL/min with the use of a dual syringe pump. During the CO_2 reduction experiment, the potential was swept from 0 V to -1.2 V *vs.* RHE (0 V to – 1.8 V *vs.* Ag/AgCl) at 0.2 mVs^{-1}. This scan rate was optimal according to the publication in reducing the impact of bubble noise. Each experiment took ca. 2.5 hours to complete.

5.5 Results

5.5.1 CO_2 Reduction on Copper Electrode

Electrochemical reduction of CO_2 was carried out on the copper ring electrode provided with the cell. The electrode was prepared for electrolysis in accordance with electrochemistry section. Figure 5.5.1 shows Mass Spectrum - Linear Sweep Voltammetry (MS-LSV) obtained from the commercial DEMS cell experimentation.

Reproducing the experiment shown in the paper resulted in some minor issues. However, the cell gave sufficient evidence that this system could be used to analyse the products formed during electrochemical CO_2 reduction at a range of potentials. Sweeping from 0 V to -1.8 V at a scan rate of 0.2 mV/s trace detection of methane and ethylene was observed from -1 V but substantial production in this cell began around -1.5 V (*vs.* Ag/AgCl). The current response of the LSV (black trace in Figure 5.5.1) appears to be very unsteady. This can be attributed to bubble formation on the copper electrode and in the confined space of the cell. A 5 Hz internal filter by the potentiostat was applied to this to attempt to stabilise the current response but it was still erratic. At around -1.2 V (6000s) a small hump can be seen in the LSV.

In this region, catalytic activity for Cu has been seen, however this discrepancy can be put down to a potential CO_2 bubble entering the cell.

Analysis at a range of potentials enables the potential at which catalytic activity takes place to be found and ascertains the right balance between desired catalytic activity (formation of products) and parasitic reactions such as hydrogen evolution. During these experiments, the faradaic efficiency for methane was around 27%, while it was around 45% for ethylene. All of the faradaic efficiencies and their totals can be found in Table 5.5.1. Concentrating on desired products methane and ethylene, there is a high yield seen at this potential range. Further experimentation to try to isolate the potential and optimise the yield of these products was therefore planned. Due to setbacks with the use of this cell however, it was challenging to continue. The issues faced are detailed in section 5.5.2 as an alternative cell design was deemed necessary.

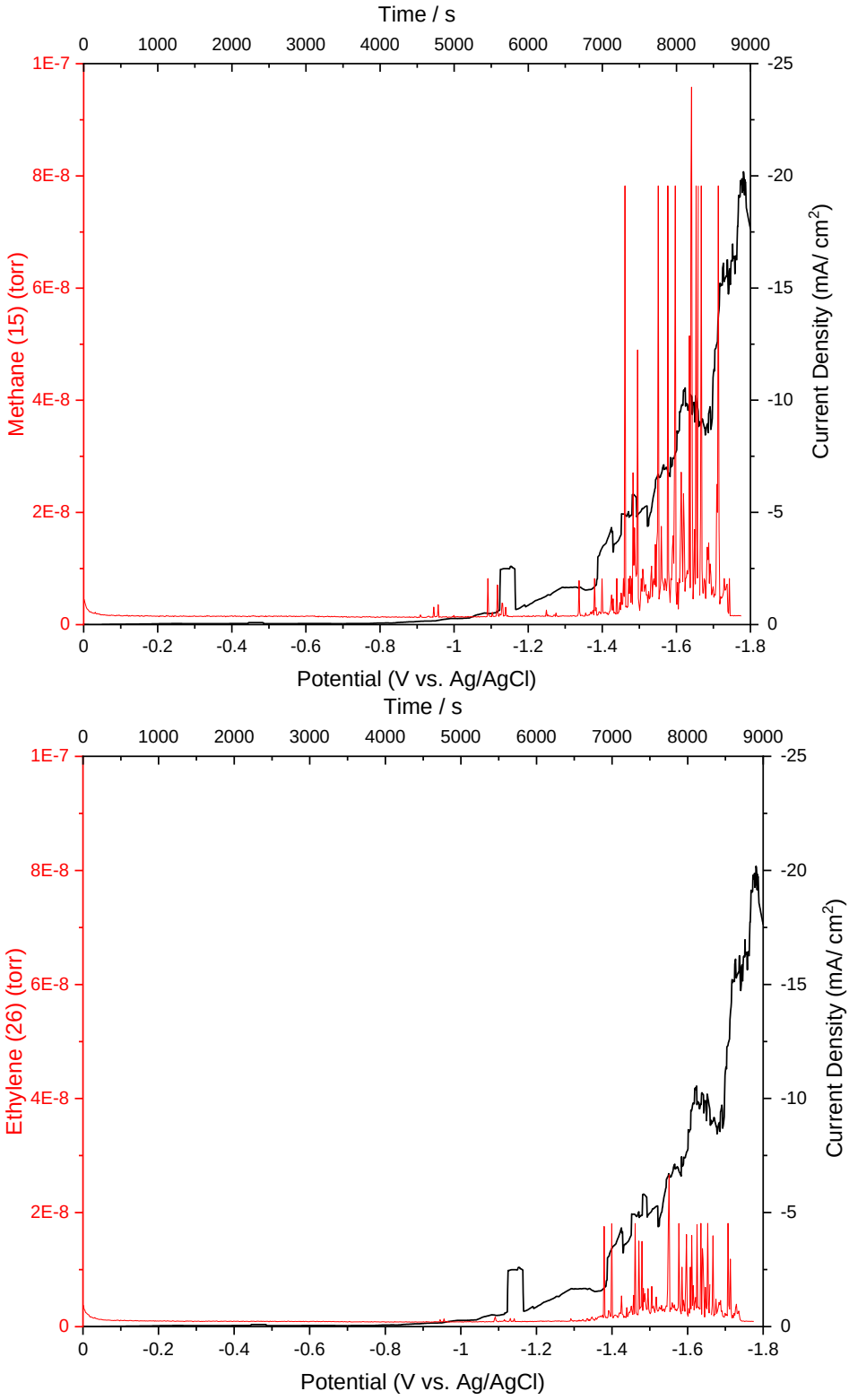

Figure 5.5.1 - MS-LSV overlay of methane and ethylene formed during CO_2 reduction using Commercial DEMS cell. Copper ring working electrode, Pt mesh counter electrode, 'leak-free' μ-Ag/AgCl reference electrode, LSV from 0 V to -1.8 V vs Ag/AgCl, 0.2 mVs^{-1}

It was stated in the paper that formic acid was undetectable with DEMS equipment. This was tested by analysing the mass ion currents of the four primary ionisation fragments of formic acid (m/z = 28, 29, 45, 46) as a CO_2 saturated electrolyte solution was passed through the cell (constant flow rate). The solution was then replaced with another containing 10 mM formic acid. There was a distinct lack of detector response. The reason behind this is due to the low pKa of formic acid (3.77), which means it is deprotonated in these reaction conditions, as well as the fact that the acid is not volatile.

Due to this, it is unable to breach the PTFE membrane to the MS.[147] Mass ratio 45 can correspond to either ethanol or formic acid, therefore in future experimentation, m/z = 45 was also analysed as there have been publications which state that it is possible to detect formic acid with a DEMS system.[12]

The use of the DEMS system and the dual cell provided, it can be said that the experiments were conducted as an introduction to on-line product analysis, with the purpose of becoming accustomed with the equipment, as well as flow systems.

Table 5.5.1 - Faradaic efficiency comparison between Commercial DEMS Cell and Flow Cell. Experiments conducted on both with similar conditions.

	Faradaic Efficiency (%)	
Product	Commercial DEMS Cell	Dual Stage Flow Cell
Hydrogen	13.00	11.00
Methane	27.27	27.80
Ethylene	45.85	47.75
Carbon Monoxide	11.31	12.31
Total	97	99

5.5.2 DEMS Cell setbacks

The DEMS cell provided was a suitable, microfluidic analysis cell, which was helpful for learning the initial stages of electrochemical CO_2 reduction using a flow cell and DEMS. However, it was found that this cell was relatively difficult to work with, and the design had flaws, which created severe roadblocks in research.

The reference electrode required to use this cell was a small, 'leak-free' μ-Ag/AgCl. It is a fantastic electrode concept, as its dimensions allow cell designs to be smaller, removing any dead space that may be introduced by a comparatively large reference electrode port (Figure 5.5.2). In this design, the reference electrode intercepts the catholyte flow and due to the microfluidic channels, resistance is relatively low.

Figure 5.5.2 - Comparison of 'leak-free' μAg/AgCl (left 1 mm O.D., middle 1.6 mm O.D. Innovative Instruments Inc., USA) with conventional, standard Ag/AgCl electrode (right, IJ Cambria, UK). Major difference in size allows flexibility of design with 'leak-free' electrodes, but promised longevity was not met for these experiments.

The ‘leak-free’ μ-Ag/AgCl however faces significant drawbacks. With multiple uses, and in prolonged electrolysis, it was found that the ‘leak-free’ μ-Ag/AgCl was unable to withstand the electrolyte used. It was not expected, as these electrodes have shown potential in cells which have used 1 M KOH, however the only conclusion that can be drawn is that the material used as the frit must be either degraded or blocked by the salts in the electrolyte. It was apparent that the reference electrode was causing issues as there would be heavy corrosion on the working electrode surface during electrolysis (Figure 5.5.3), and the current response would be erratic.

Figure 5.5.3 - Copper ring working electrode, post-analysis corrosion.

The ‘leak-free’ μ-Ag/AgCl were washed and stored after use as recommended by manufacturer. To confirm, the ‘leak-free’ μ-Ag/AgCl was checked against a saturated calomel reference electrode (SCE), which resulted in behaviour characteristic of a bad reference. Attempts to revive the electrode included the manufacturer-recommended immersion in water, and also immersion in chloride solution. The measures taken were not helpful in reinstating the function of the electrode. To continue with work with this cell, multiple ‘leak-free’ electrodes were used, however this is not an economically viable option given the frequency of electrolysis studies required. Due to this, a cell design that incorporates a standard, more commercially available Ag/AgCl would be better.

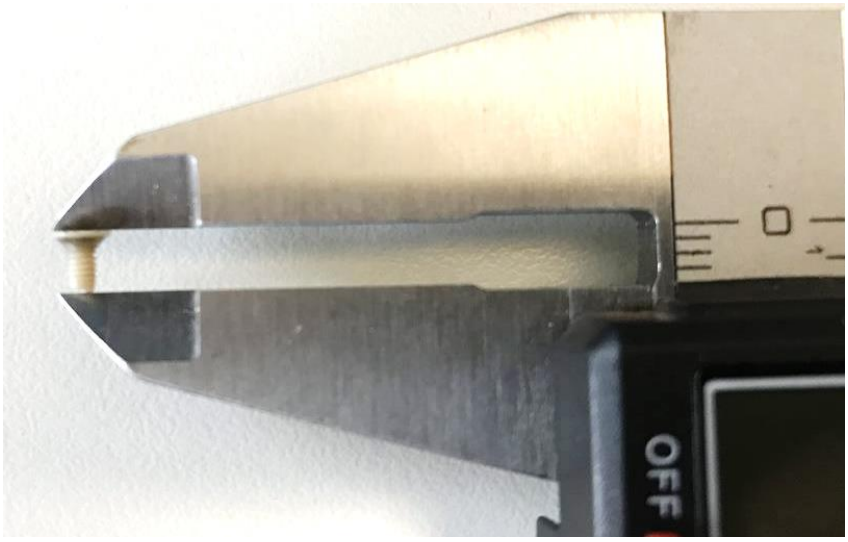

Figure 5.5.4 - Flow through retaining screw size 4 mm.

Further to this design was the fact that it was not adaptable. It was supplied with a machined copper ring held in place by a 4 mm PEEK screw (Figure 5.5.4). This PEEK screw retained the electrode and was a channel for the electrolyte to enter the working chamber. The design concept is good as the electrolyte enters through the centre of the ring-shaped electrode, and is distributed over the electrode surface evenly to channels that take the electrolyte and products to the pervaporation membrane. The limitations faced here include the fact that the ring electrode was machined specifically to fit the cell; therefore attempting to use other metals would require a specially made ring with the exact same dimensions.

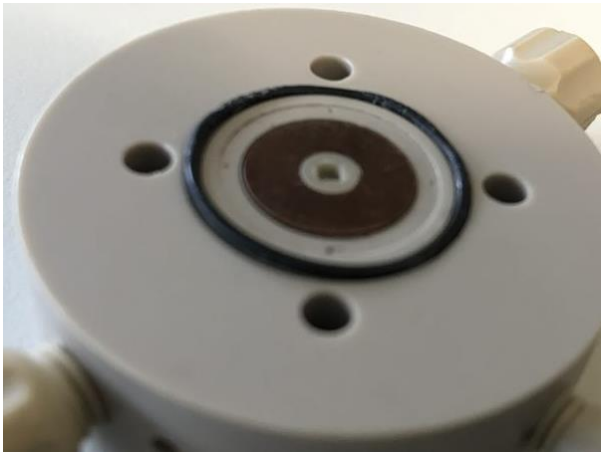

Figure 5.5.5 - Copper ring electrode inside cell, held in place with screw. Wear and 'rounding' of the screw can be seen, making it considerably difficult to remove.

Furthermore, attempting to use a graphite based current collector for drop-cast or electroplated catalyst was not possible due to the shallowness of the electrode bay. PEEK is very resilient and great for making small parts; however, the retaining PEEK screw was seen to degrade with time. This is due to the pressure required to retain the ring electrode in place. Since this cell is reliant on this screw, it would require replacing every so often to ensure correct cell operation. The screw is also very small, making it difficult to handle, reducing the user-friendliness.

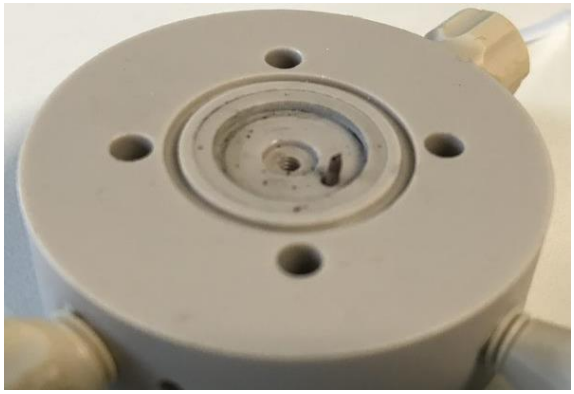

Figure 5.5.6 - Recess for copper ring working electrode, with copper connecting rod visible. The position of the connecting rod is due to spring underneath. Careful positioning and pressure would need to be applied while electrode is screwed in to ensure connecting rod spring is fully pressed, therefore completing the connection. Connecting rod made from piece of copper wire, size determined through trial and error.

The electrode was connected using a very small rod of conductive metal that is inserted into a sprung hole before the electrode is sat in the space (Figure 5.5.6). This rod then contacts the copper wire inserted from the outside of the cell to form connection to the electrode. The hole contains the spring, so that the connection between the working electrode and the wire leading out is ensured and held in place by the screwed-in working electrode. This design therefore requires solid metal electrodes to be able to be screwed down with enough pressure to ensure connection. Attempts were made with the use of carbon bi-polar plate material, as graphite of around 100 μm would be too brittle; however, the plate was seen to bend due to the force of the spring pushing up the connecting rod.

This was not a viable option to be used in the cell. The conclusion was then drawn that using machined carbon electrodes such as glassy carbon was also not possible.

Overall, the cell design and concept were good for learning how to use the system in very restricted parameters. However, the user-friendliness was poor due to challenging small parts, the requirement for restrictive electrode designs and therefore the lack of flexibility of working electrodes and catalyst modifications that could be used. Due to this, a flow cell system that was easy to use, adaptable to different catalysts and did not use such specialist parts was conceived.

5.6 Adaptable Flow Cell (AFC)

5.6.1 Introduction and Development

A completely new cell design was conceptualised to overcome the shortfalls and limitations of the previous cell designs. This cell design was based upon existing electrolyser designs for redox flow battery research within the group and the works of Brushett group[148-150].

Due to its ability to incorporate parts through stacking the electrolysis cell is usable as a standard flow cell and as a GDE cell. Correspondingly the cell design was denoted as an Adaptable Flow Cell (AFC). The graphite current collectors are part of the stack and do not require integrating into the cell body. There is no metal introduced into the system from connectors as all electrical contacts are external of the cell. This eradicates the issue from the commercial flow cell where the brass electrical contact behind the current collector would interfere with electrochemistry. The AFC design is modular, therefore allows different electrode configurations, and flow fields for introduction of gas to a GDE or electrolyte into the system. This flexibility therefore makes this cell design adaptable for use in a multitude of applications.

The AFC concept was first designed using CAD, and 3D printed using Fused Deposition Modelling (FDM) to test the ease of assembly and scale of flow cell. Figure 5.6.1 shows an image of this concept. The cell concept was printed with the cell outer body, spacer for reference electrode and cathodic electrolyte flow and current collectors, as they make up the most of the cell.

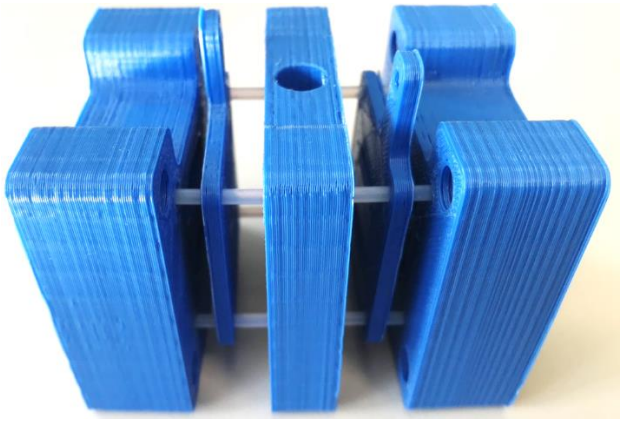

Figure 5.6.1 - FDM-3D Printed initial cell concept to observe ease of assembly and scale. Cell body, spacer and current collectors all printed in ABS.

The FDM concept of the cell was not usable for ECO_2RR due to the nature of the printing. The layers formed are not close enough to ensure liquid or gas tightness. Once it was established that this cell scale, design and assembly by end user was good to proceed with, the cell was manufactured using resin 3D printing. The layers at which resin 3D printing manufactures components are considerably smaller and closer (50 µm) than FDM (200 µm), meaning liquid and gas tight components can be made. Settings for the resin 3D printer can be found in Appendix B.

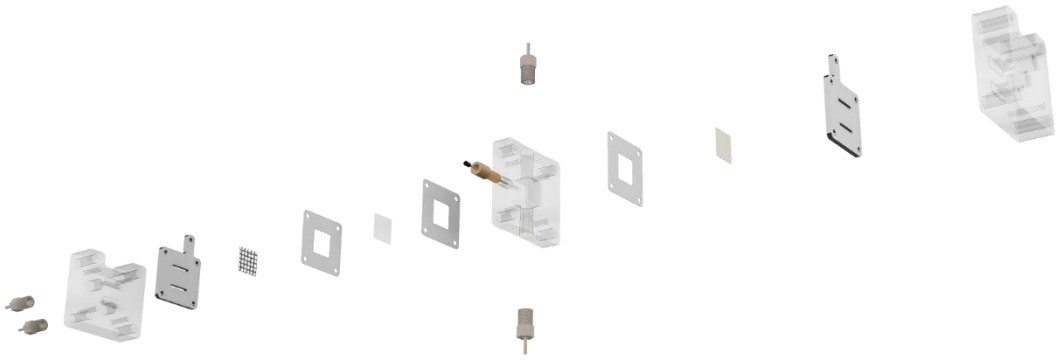

Figure 5.6.2 - 'Exploded' CAD view of cell and components.

For initial electrochemical testing, the AFC body and reference electrode spacer was 3D printed in-house using a methacrylate-based resin (Anycubic Photon DLP, Anycubic Shenzhen, PRC). The current collectors were milled out of ppg-86 graphite-polypropylene composite using computer numerical control (CNC). Gold-pin contacts were used as the electrical contacts. The gaskets used in this cell were of a 0.5mm thickness, laser cut from ethylene-propylene diene monomer (EPDM) rubber. Platinum mesh counter electrode (20 x 20 mm, 82 x 82 wires/inch, 99.9% Sigma-Aldrich), Cu plate working electrode (2.475 cm^2, Alfa Aesar) and Ag/AgCl reference electrode (IJ Cambria).

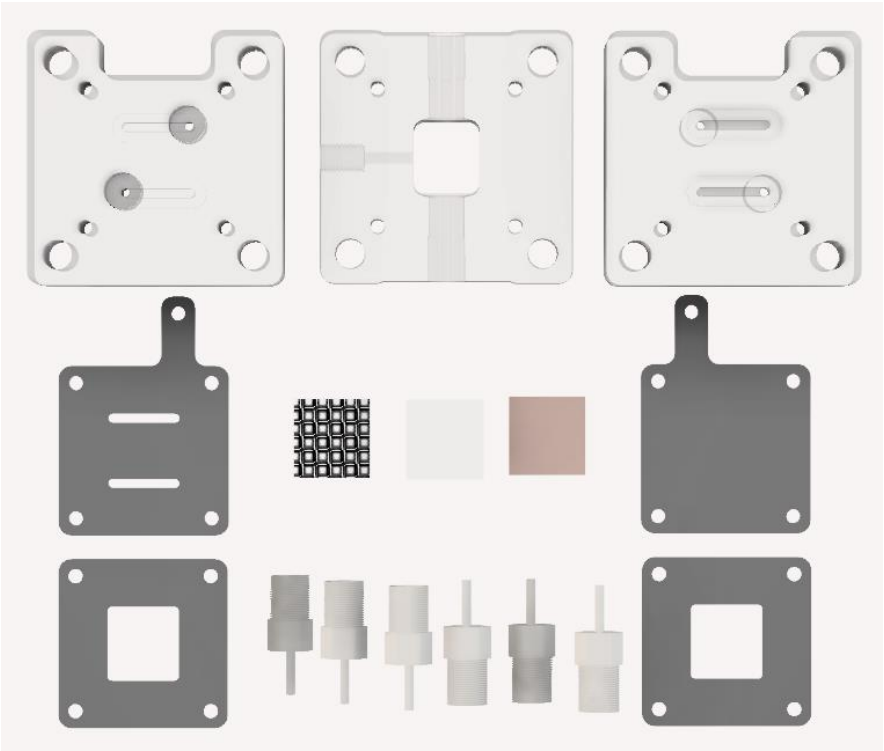

Figure 5.6.3 – AFC Plan layout. Top row left to right: Cell body, Spacer, Cell Body. Middle row: Flow-through current collector for Pt Mesh, Pt Mesh, Nafion-115 Membrane, Cu Plate, Current collector for Cu Plate. Lowest row: Gaskets and NPT tube fittings.

The AFC body and spacer were then CNC machined out of clear acrylic. The use of acrylic was possible due to the inert nature of the reactants and electrolyte. This was especially beneficial to observe the cell internally at the cathode surface, however acrylic is also more durable than the 3D printed resin for multiple use. Therefore, 3D printed resin cells are possible, but require research into the resin used to ensure longevity and protect against warping and damage from multiple use.

Figure 5.6.3 shows a plan layout of the AFC in standard flow cell configuration. In this configuration, the electrolyte for the anodic reaction is passed through the side of the cell, through the flow field, and through the Pt mesh, leaving from the side of the cell again. The cathodic electrolyte flow however only passes through the spacer where the reference electrode is housed. The blank current collector and solid Cu plate ensures no electrode passes through to the ports on the cathodic side of the cell. These side ports are only enabled when using the AFC in GDE configuration, as a gas-diffusion electrode is used with a flow field current collector for entry of gas. The most efficient flow field for gas was determined to be a serpentine flow field, to ensure even distribution of the gas before leaving the cell (Figure 5.6.4).

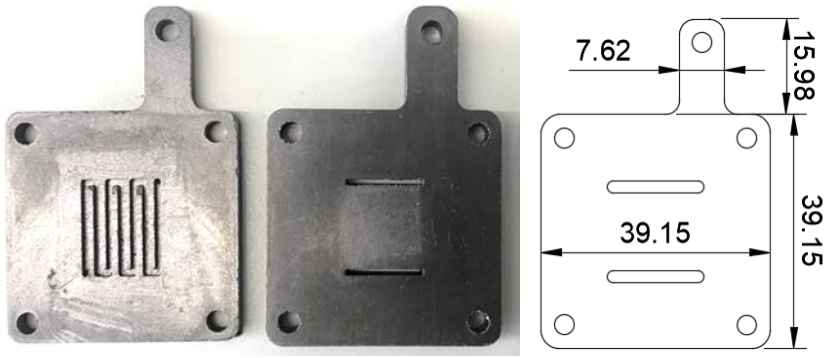

Figure 5.6.4 – Serpentine flow field current collector (left) to provide even distribution of gas to the GDE. Flow-through flow field current collector (centre) for comparison, used for electrolyte flow through Pt mesh. Dimensions of current collector (right).

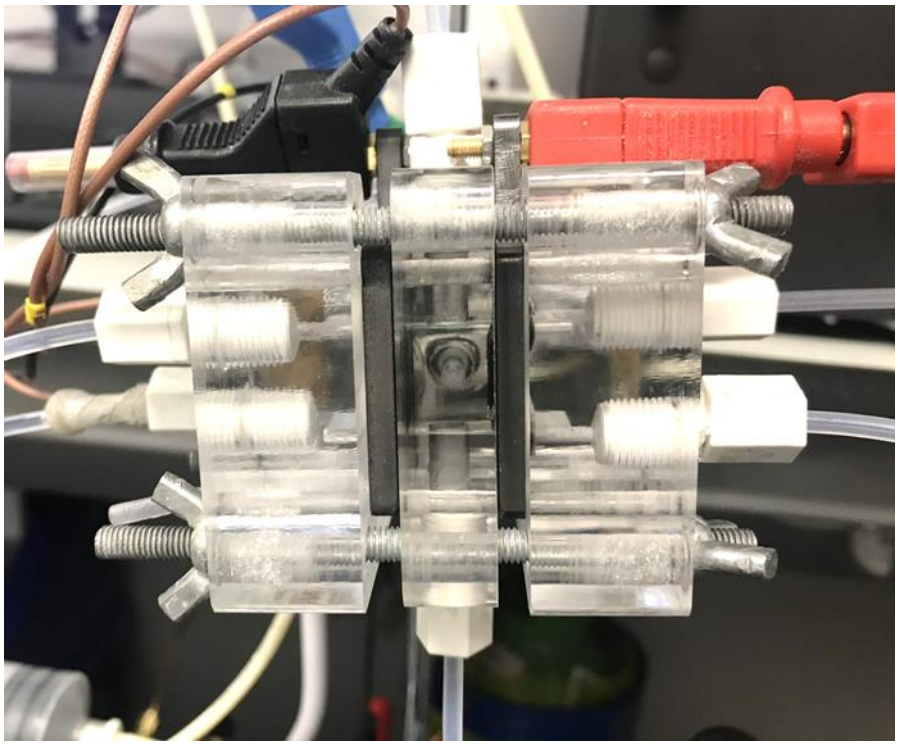

Figure 5.6.5 – AFC with all ports in use for GDE setup. Ports to the left used for anodic electrolyte flow, ports in spacer for cathodic electrolyte flow, ports to the right for CO_2 flow to GDE.

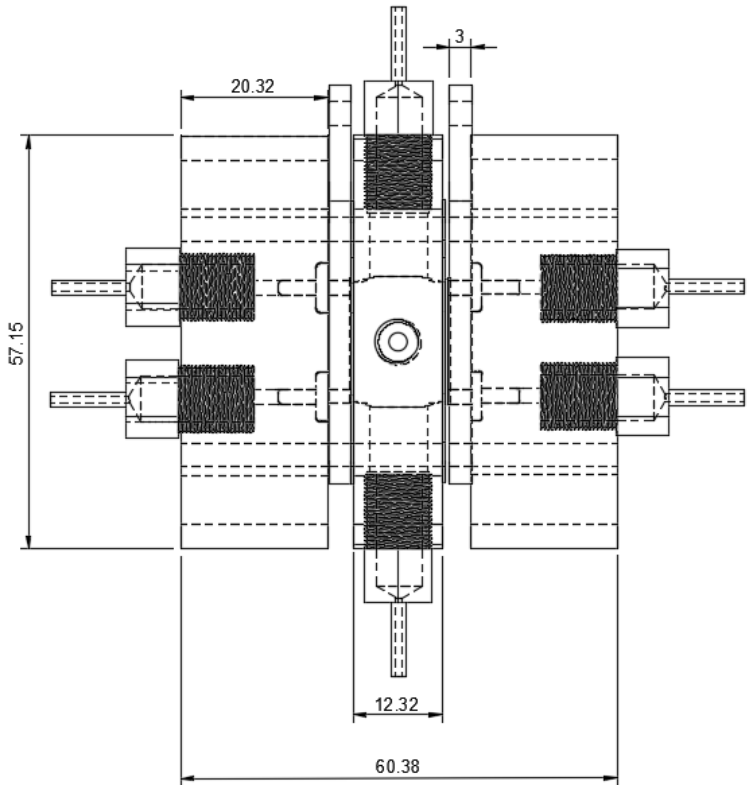

Figure 5.6.6 - Assembled flow cell dimensions. All measurements are in millimetres.

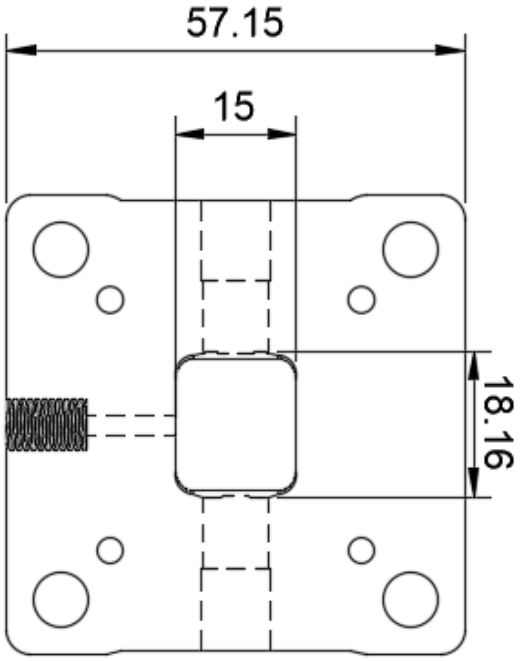

Figure 5.6.7 - Spacer dimensions inc. chamber (18.6 x 15 x 12.32 mm, internal volume 3.44 cm^3).

The cell can be used in two configurations (standard flow and GDE) without further modification; however, the spacer or parts of the cell may be modified and adapted to enable methods such as novel sampling.

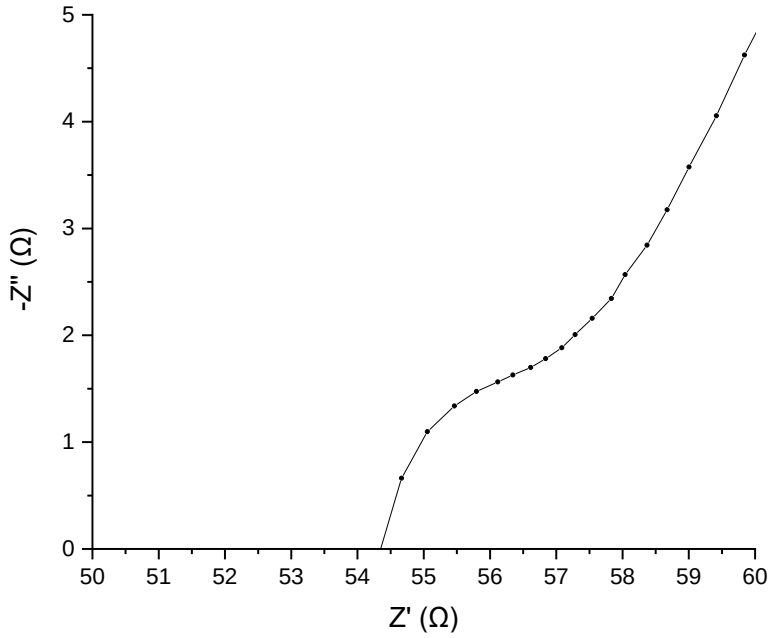

Figure 5.6.8 - EIS of AFC in standard flow cell configuration. WE =Cu plate, CE = Pt mesh, RE = Ag/AgCl. 0.1 M $KHCO_3$ electrolyte flowing at 1 mL/min. Ohmic resistance around 54.5 Ω.

The cell in standard flow configuration and GDE configuration exhibited internal resistances around 55 Ω depending on configuration. This resistance can be attributed to the low concentration of the electrolyte, therefore lower electrolyte conductivity. The cathodic flow chamber volume (3.44 cm^3), and the distance between the working and counter electrodes (12.32 mm) may also have an effect overall resistance. The justification for the spacer width was to incorporate a full sized reference electrode instead of a μ-Ag/AgCl due to drawbacks that are discussed *vida infra.* A Luggin-capillary could be employed to ensure that the reference is as close as possible to the working to combat internal resistance. In this design it sits perpendicular approximately 3 mm away.

5.6.2 **Dual Stage Flow Cell OLEMS**

The Dual Cell designed by the Berkeley group comprised a single unit with two distinct functions that appended directly to the DEMS inlet. In this new design the strategy was to separate the functions into two stages, the electrochemical flow cell and a microfluidic bridge that interfaced the DEMS. A simple schematic of the set-up used for CO_2 electrolysis is given in Figure 5.6.9.

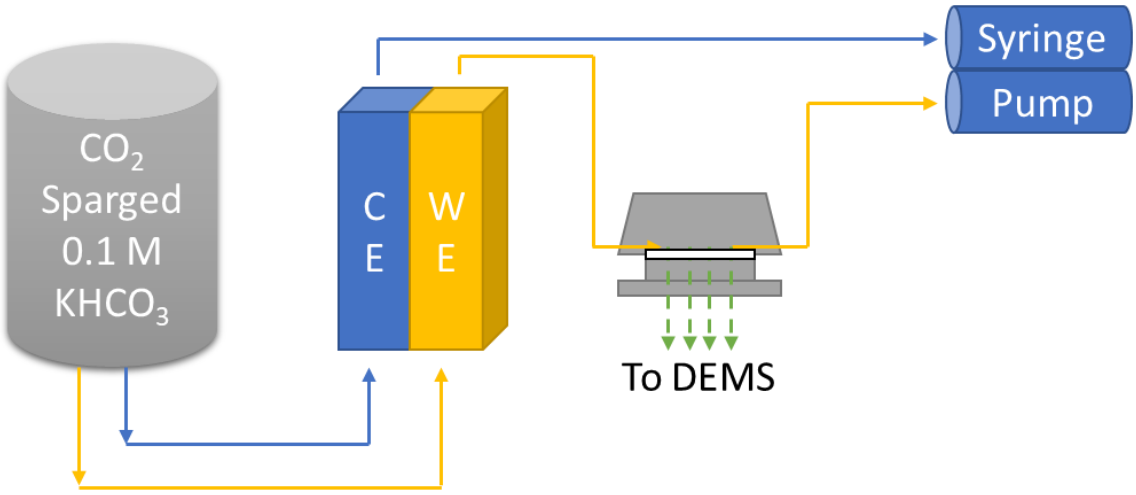

Figure 5.6.9 – Simplified diagram to show set-up used for electrochemical reduction of CO_2 using flow cell and bridge interface. Blue line signifies CO_2 sparged $KHCO_3$ anodic electrolyte flow, yellow line signifies CO_2 sparged $KHCO_3$ cathodic electrolyte flow, both at 1 ml/min, negative system regulated by syringe pump. Electrolyte reservoir above cell to deliver electrolyte through gravity feed. Cathodic flow through spacer, interacting with Cu working electrode (WE), then out with products to interface bridge for DEMS before being collected into syringe. Anodic flow through flow field and Pt mesh (CE), then directly to syringe pump. Connections to potentiostat not shown in figure.

The Microfluidic Bridge (which will be simplified to 'bridge' in this document onwards) consisted of the supplied 'Hiden Single thin layer DEMS Type A-cell' adapted to integrate a flow cell (Figure 5.6.10) sequentially. Adapting this cell enabled an external flow cell to be used with the DEMS system. To reduce confusion, the term OLEMS was adopted (On-Line Electrochemical Mass Spectrometry), however still using the DEMS system as it is still a differentially pumped mass spectrometer. The flow cell design was inspired by a design created for redox flow batteries as well as CO_2 electrolysis by the Brushett group in MIT [149, 150]. This cell design is shown detailed in the Cell Design chapter; however, use with OLEMS is covered here.

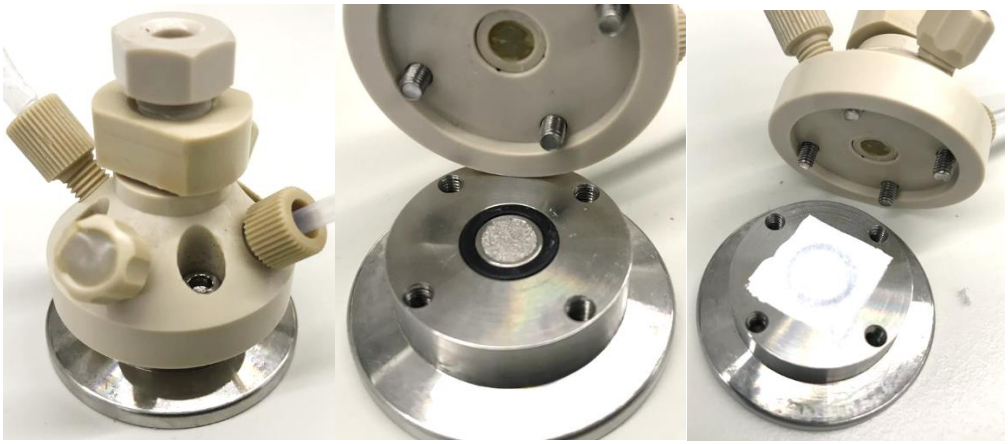

Figure 5.6.10 – 'Hiden Single thin layer DEMS Type A-cell' adapted for use as a microfluidic bridge (and pervaporation chamber) to interface the flow cell with the MS inlet. Inside of bridge (middle) shows metal frit MS inlet and sealing gasket. Inside of bridge (right) shows the small chamber for electrolyte flow through and PTFE membrane interface atop the metal frit. Chamber volume 5.5 µL. [147]

The electrochemical flow cell catholyte outflow was introduced to the DEMS inlet inside this bridge (volume approx. 5.5 μL) at a defined flow rate. The electrolyte then continued through and was collected in the syringe pump. A syringe pump governed the defined electrolyte flow rate (1 mL/min) at the end of the setup. Pulling the electrolyte through the system to create a negative system pressure ensured linearity of flow, prevented pressure issues inside the cell or at the DEMS inlet (pervaporation membrane breach from pressure) and avoided artefacts in the voltammetry typically observed when using a peristaltic pump system. The flow rate was defined to ensure sufficient residence time within the electrolysis cell as well as at the DEMS inlet inside the bridge.

With the electrochemical cell not directly attached to the DEMS inlet, there is an inherent delay in the products flowing out of the cell and into the bridge. To minimise this, the space and the tubing between the cell and the bridge was kept as minimal as possible, with a smaller I.D. tubing used for the cell outlet. Typically, that temporal delay was of the order of 2.3 seconds, due to the microfluidic tubing (I.D. 0.5 mm ∅) and minimal bridging distance of 20 cm (internal volume 0.0392 cm^3).

The advantages of decoupling the processes outweighed the advantage of a minimal time delay between electrode polarisation and product analysis. The cell being separate from the inlet enabled working with the cell without disturbing the inlet. It also enabled the use of non-specialist electrodes, as the cell design uses square plates instead of precision-machined rings. Furthermore, this cell design was more adaptable as well as scalable. This cell set up does comprise more parts than that of the original commercial DEMS cell, especially as it does not attach directly to the MS inlet, however the flexibility in the use of this set up makes it considerably more accessible.

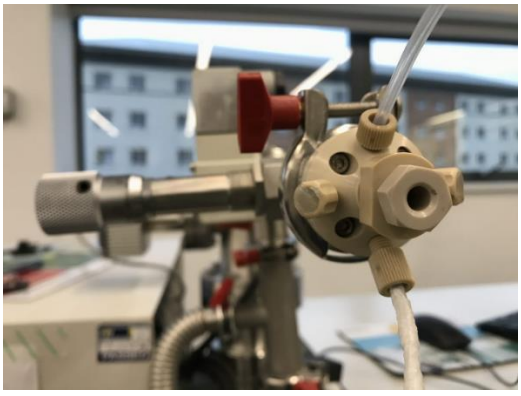

Figure 5.6.11 - Bridge placed at MS inlet. Cathodic electrolyte inflow pipes attached.

5.6.3 CO_2 Electrolysis Results – Dual Stage Flow Cell Design

To evaluate the performance of the dual-stage OLEMS arrangement, the conditions of the electrolysis study with the commercial DEMS cell were repeated. The main difference being the use of a copper plate electrode in place of the copper ring used in the Commercial DEMS cell, however preparation of the electrode was the same. The MS-LSV profiles in Figure 5.6.12 show the current response during the LSV overlaid with the MS response for methane and ethylene. Compared to Figure 5.5.1 there appears to be very little difference from the Commercial DEMS dual cell results. The onset potential for both methane and ethylene is ca. -1.4 V vs Ag/AgCl, with almost no response observed prior to this. Hydrogen and CO were also detected, as with the Commercial DEMS Cell. When analysing the faradaic efficiencies, overall performance matches or slightly exceeds those of the Dual Cell, with 99% total FE accounted for compared to 97% in Commercial DEMS Cell, as observed in Table 5.5.1. A notable difference is the improvement in the voltammetric trace, with a smoother polarisation observed in the Dual Stage data. Noise is observed in the current response which can be attributed to the bubbles on the surface of the electrode. Bubble hold-up in this cell was minimal, however as more products were formed and hydrogen evolution took place, bubbles were somewhat retained on the surface of the electrode. The design of the spacer included curved corners to prevent bubbles being held up inside the chamber.

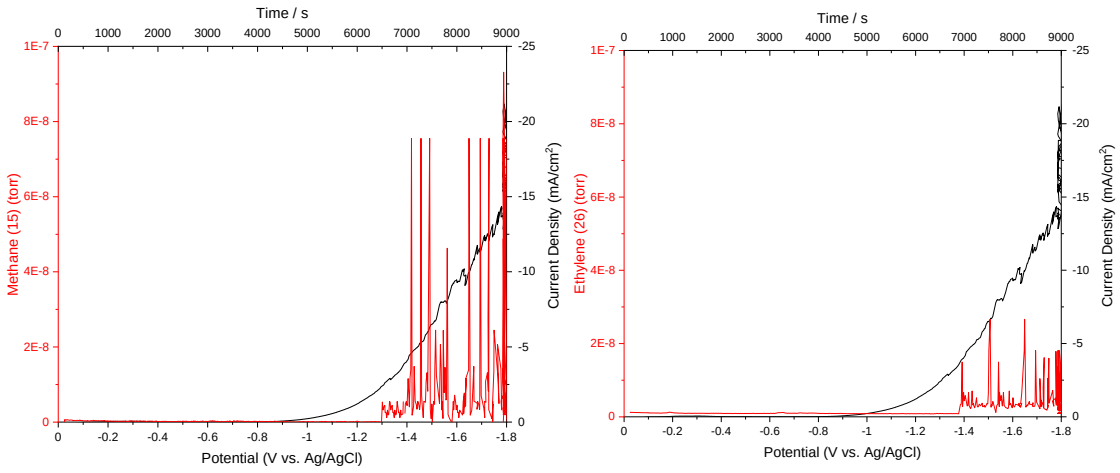

Figure 5.6.12 - MS-LSV overlay of methane (A) and ethylene (B) formed during CO_2 reduction using the flow cell method. Copper plate working electrode, Pt mesh counter electrode, Ag/AgCl reference electrode, LSV from 0V to 1.8V vs Ag/AgCl, 0.2 mVs^{-1}

The overall faradaic efficiencies displayed by this cell are similar to those displayed by the Commercial DEMS cell. Table 5.5.1 displays a comparison of faradaic efficiencies for both cells when tested under similar conditions, with the exception of an Autolab potentiostat being used for the Dual Stage Flow Cell experiments, the use of a standard Ag/AgCl electrode, and a PTFE pervaporation membrane from a different supplier (PALL EMFLON® PTFE PTF002LH0P, 20 nm pore size, 0.5 cm^2 surface area, Pall Corporation, UK).

5.6.4 **Discussion on the effectiveness of the Dual Stage Flow Cell**

Comparing both cells with experiments conducted using the method stated in the Commercial DEMS publication, [147] the faradaic efficiencies for each gaseous product of interest and overall are very similar. The increased efficiency of the flow cell may be attributed to the larger working electrode surface area, therefore less resistance to form the higher value hydrocarbon products. The cell resistance of the flow cell was between 40-50 Ω, while the resistance reported for the Commercial DEMS Cell was around 50 Ω [147].

The Commercial DEMS cell is a self-contained unit, which would deliver the products directly to the MS inlet, while the flow cell setup delivers to the MS inlet through tubing. This introduces potential weak zones regarding gas tightness, as the tube connectors require sealing so that they may not leak gasses. Furthermore, the increased amount of fittings and fixtures may also introduce these weak zones. Ideally, a self-contained unit, which attaches to the MS inlet, flexible to different catalysts would resolve this issue; however, attempts to conceptualise this compromised important factors such as user-friendliness.

The critical observation made in this study was that separation of the two cells into distinct sequential stages did not compromise the electrolysis study. This is primarily due to the approach taken in this study to emulate the Commercial DEMS paper, [147] in which the total products formed was determined rather than the evaluation of onset potentials. In the context of studies by the Koper group and other research groups in developing DEMS cells, the focus has been on the temporal resolution of product formation and electrode polarisation to ascertain kinetic mechanisms.

5.7 Membrane Inlet MS Probe concept

An idea formulated to resolve the issues cited above, was to bring the MS inlet into the flow cell. This method would involve using a probe that could be inserted into the flow cell to analyse the products close to the electrode, along with those being dissolved in the spacer. Time-delay between the flow cell and the MS inlet would be negligible, and resolve potential gas leakage issues from the cell, or tubing between reaction cell and MS inlet. The interfacing bridge would also not be required, therefore making the system one-component and more straightforward. Furthermore, this probe could be used in a variety of cells, static or flowing, as there would be freedom in positioning the MS inlet to the catalyst surface. Potentially allowing for variation in catalytic activity across a sizeable planar electrode to be evaluated as well.

This idea was conceptualised into a Membrane Inlet probe for the Mass Spectrometer (MIMS). The idea was to remove the current KF flange from the MS inlet and replace with a flexible line. No other changes would be made to the DEMS system. For the concept, gas-tight PFA tubing was used, which would not collapse under vacuum. The use of the clear PFA tubing also helped observe potential breaches of the pervaporation membrane. The end of the tubing consisted of a probe, which contained a PTFE pervaporation membrane interface.

The design of the probe meant that the tube could be inserted into it. Low tolerances allowed a gas tight fitting; however, some gas-tight PTFE tape was used to ensure this tightness. Prior to insertion, the tube end would be covered by the pervaporation membrane. This meant that the membrane would be inserted with the tube into the probe, resulting in the pervaporation interface.

The conceptual probe was designed in CAD (Autodesk Fusion360) and 3D Printed (Anycubic Photon) for use with a flow cell. The initial design consisted of a screw thread to insert the probe. This was then able to be securely screwed into a flow cell spacer designed to hold this. The electrolyte flow path was also revised, as the gasses could escape the probe interface and exit with the electrolyte.

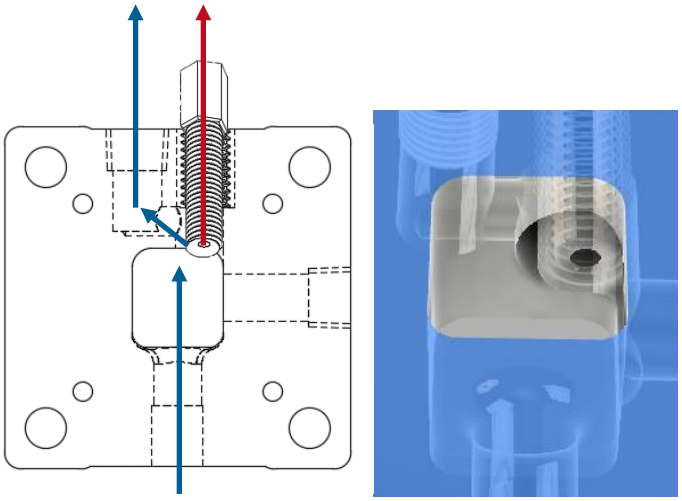

Figure 5.7.1 – Conceptual drawing of probe being held in specially designed spacer. Electrolyte flow (blue) exits via the probe interface, allowing dissolved and evolved gasses (orange) to be collected.

The electrolyte flow was first designed to leave from an outlet beside the probe, after coming in contact with the interface end. This design caused crowding at the top of the spacer and did not address the issue effectively. A second design was then tried with the electrolyte outlet being at the lower end of the spacer. The idea behind this was to try and essentially create a ‘headspace’ inside the cell chamber, where the only outlet for evolved gasses would be through the probe. The electrolyte outlet channel diameter was also reduced, to prevent electrolyte entering the cell and exiting immediately. A drawback to this design was that there was no longer a linear electrolyte flow over the cathode. The cell required ‘filling up’ before flow was started to avoid the upper electrode areas and the PTFE interface from being dry. During testing, the probe's main issues were gas-tightness overall, and from the membrane. The design was manufactured with 3D printing to tight tolerances, to be able to form a seal against the tubing. The membrane was also able to cover the end of the tubing, and the probe inlet hole was smaller to ensure no escape from around the tubing. This however required rectifying with the use of gas-tight PTFE tape, to form a tighter seal.

Furthermore, the PTFE membrane surface area is considerably smaller than that of the bridge cell, therefore for prolonged use, the membrane was not ideal. It was found that there were salt deposits from the electrolyte, which appear to block the pores of the membrane. To confirm this, future work would consist of running the probe with ultrapure water spiked with calibration gas, over a period of time.

In theory, the design would revolutionise working with the DEMS equipment, however due to the challenges faced with designing gas-tight components that can be interfaced with high vacuum, as well as time lost to the global pandemic, further work on this was stopped in favour of bringing other work to completion. Since this concept was initiated, Hiden has commercialised probes that interface with their DEMS system, therefore deducting the need to design the probe. The flow cell spacer may be adapted to and re-designed to house this commercial probe very easily. The aim of the probe and its ease-of-use can also be met, as it would be able to be implemented into static, 3-electrode cells, H-cells, and any other type.

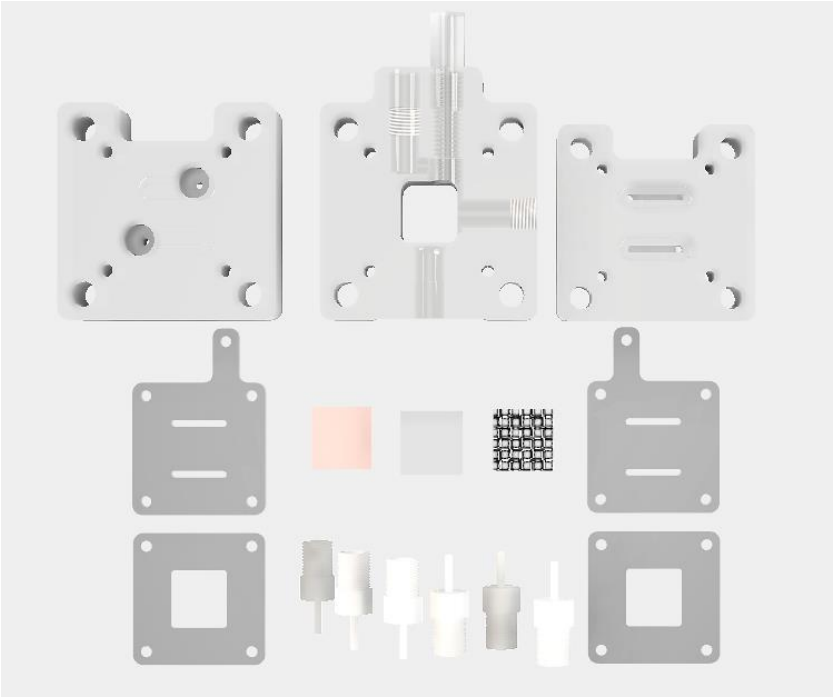

Figure 5.7.2 – MIMS probe Flow cell layout. Top row left to right: Cell body, Spacer with MIMS Screw-in probe, Cell Body. Middle row: Flow-through current collector for Pt Mesh, Pt Mesh, Nafion-115 Membrane, Cu Plate, Current collector for Cu Plate. Lowest row: Gaskets and NPT tube fittings.

Figure 5.7.3 shows preliminary results obtained for hydrogen using the flow cell MIMS probe during cyclic voltammetry from 0 to -2.3 V (*vs.* Ag/AgCl). The current and the MS detector response can be seen to line up reasonably well, with some MS peaks not lining up as well. This may be due to bubble hold up inside the cell, as well as the MS interface. The current response by the third cycle is higher by comparison to the first two, and alongside the MS detection for hydrogen is also increased. This may be also due to surface bubble hold up, or conditioning of Cu working electrode surface and CuO_x layers.

These results shows that it was possible to create a MIMS probe, however in the future, further research into gas tightness, membrane positioning and membrane longevity require strong consideration. The design of the probe to be able to hold the membrane without stretching may consist of building a two-part probe, where the membrane can be essentially clipped into place. For the positioning, the closer to the working electrode the better, therefore a design that can face the working electrode would be advantageous in analysing directly from electrode surface. Membrane longevity may depend on how it is positioned and held by the probe. If undamaged or stretched, it may be able to last longer. Experimentation using ultrapure water first then electrolyte to analyse whether salt deposits were an issue was planned, however due to time constraints were not carried out.

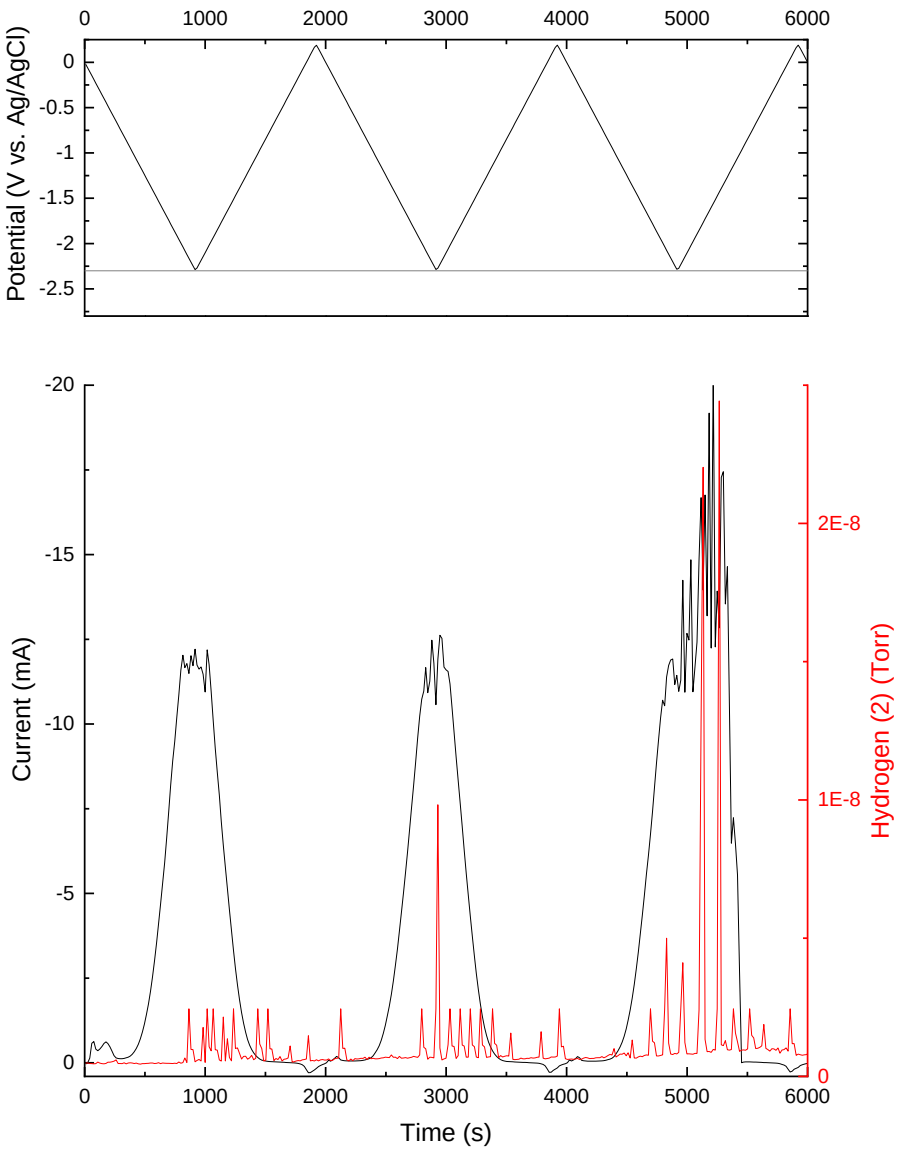

Figure 5.7.3 - Overlaid Mass Spectra-Cyclic Voltammogram (MS-CV) to show response of hydrogen during cyclic voltammetry from 0 to -2.3 V (*vs.* Ag/AgCl). Scan rate 0.0025 V/s, 3 scans, average taken. Cu working electrode, Pt Mesh counter electrode, Ag/AgCl reference electrode. CO_2 saturated 0.1M $KHCO_3$ electrolyte, flowing at 1 mL/min.

5.8 Conclusions

Combining the electrochemical reduction of CO_2 with an on-line analytical technique is challenging for multiple reasons. However, the design of the reaction cell is seen to be one of the main issues. Interfacing a reaction cell for DEMS is possible, but the design of the cell must be accommodating to users and adaptable for analysis outside of certain materials. This chapter discusses the use of on-line mass spectrometry for ECO_2RR, focusing on comparing the design of the supplied reactor cell, the Commercial DEMS Cell, and an alternative Dual Stage Flow Cell developed during this PhD for a user-friendly, adaptable and scalable solution. It was found that the performances were very comparable with both designs achieving near 100% faradaic efficiency for gaseous products on copper electrodes. However, the lack of adaptability, convenience, and a requirement for specialist electrodes and parts made the Commercial DEMS Cell the less desirable option when continuing work on ECO_2RR.

This chapter also outlines a preliminary concept of a new sampling method called Membrane Inlet Mass Spectrometry (MIMS). The DEMS interface is introduced directly to the electrochemical cell by means of a membrane probe. Such a system has potential to circumvent the time delays and product loss that could occur when using a two-stage system. Some preliminary results were demonstrated in which hydrogen production was monitored over a series of cyclic voltammograms, but the design requires further work to be developed fully.

6 Conclusions

6.1 Summary

As the climate crisis evolves and manifests it is becoming more and more important to try to implement methods that can reduce, and potentially reverse the effects of the greenhouse gasses on the planet. As the world takes steps to move towards a greener future, measures also need to be taken to ensure the damage that has already been done can be reversed. Carbon capture and storage (CCS) methods are being developed all over the world to capture the greenhouse gas and waste product, CO_2, however utilisation of this is still seen to be limited. Electrochemical reduction of CO_2 is an up and coming method to convert CO_2 into reusable chemicals and fuels, with the aim of creating circular systems where effluent CO_2 can be captured, and converted to fuels or other chemicals for use. Currently, the efficiency of ECO_2RR is minimal, due to the energy input required to obtain the smallest amount of product, however due to the climate crisis, reactors and catalysts to improve efficiency are being innovated at an exceptional rate. Comparing the research into ECO_2RR from the days of Hori, to now, shows an exponential rise in research. In this thesis, the role of reactor cell design and product analysis is discussed.

Due to the nature of ECO_2RR, there are multitudes of products that can be produced from the reaction. With the use of a copper electrode, at least 16 products in gaseous and liquid phases can be made. An array of analytical methods are therefore required to ensure detection, qualification and quantification of each product. This thesis outlines the process of creating methods with Ion Chromatography, NMR, DEMS and GC-BID, to analyse samples off-line and on-line. Combined on-line analysis using DEMS and GC-BID allows for analysis of products dissolved in electrolyte and evolving through GDE.

The importance of an exemplary reactor design does not only stop at efficiency, but user friendliness, adaptability, scalability, use of non-specific electrodes, the list goes on. Chapter 5 discusses the importance of comparing commonly used cell configurations and developing a flow cell to suit standard solid plate and GDEs, known as the adaptable flow cell (AFC).

A comparison is also made in Chapter 5 between the use of the AFC with an interfacing bridge for on-line mass spectrometry, and an established commercial DEMS cell supplied with Hiden DEMS equipment. In this chapter, the advantages and disadvantages are stated, with particular focus on the user-friendliness, and adaptability of the Commercial DEMS cell. In theory and practice, the Commercial DEMS cell is a great, thin-layer DEMS cell to learn ECO_2RR analysis with DEMS; however, the lack of user friendliness and bespoke nature of tiny components and electrodes, were considerable negatives for this cell. In contrast, interfacing the AFC may introduce some delay, and extra parts to consider, however the user friendliness of the AFC, as well as the adaptability and scalability, shadowed the fact that extra components are required to interface with the DEMS inlet. In attempt to address the lag, eliminate the 'bridge' that interfaced the outflow from the AFC with the MS inlet, and bring the MS inlet closer to the electrode surface, a membrane inlet mass spectrometry (MIMS) type probe was conceptualised. The MIMS probe consisted of a 3D printed probe, which fit into a custom 3D printed AFC spacer. The membrane was the same PTFE pervaporation membrane used in the bridge and DEMS cell.

6.2 Retrospectives and Future Work

The field of electrochemical CO_2 reduction has been ever-growing in the past two decades, allowing for research on all aspects, namely catalysts, cell design and analysis. In research terms however, it can be said that it is still in its infancy, as there are no set techniques to guarantee desirable results. Research into new catalysts on its own is a large field due to the varieties possible. Section 1.3.3 summarises some of the different types possible when working on a single metal, copper. To be able to work on catalyst development, the cell design must not take away from catalytic performance. Flow cells in recent years have seen success in delivering desired results,[76, 84, 146, 149, 151] however there is yet not one standardised flow cell that can be adopted for new ECO_2RR researchers, or commercial use.

The differences in all cell designs are due to the catalyst and the analysis being conducted using them. Some cells are made for direct analysis by attaching at the inlet of the analytical equipment,[140, 146] while others allow for gas diffusion electrodes for purely gaseous analysis[88, 148, 150]. The task of creating a cell design which is essentially the 'jack-of-all-trades' is therefore challenging. This also applies to analytical methods, as historically there has been use of arrays of analytical methods to elucidate the products of ECO_2RR. As technology develops however, there can be more confidence in saying that the goal of reaching a set analytical method or array for ECO_2RR is drawing closer. Being able to know from the start which equipment is required for efficient and accurate product analysis allows for more time to be spent on catalyst development, as to be able to produce quantities of desirable products such as C_{2+}, without the need for high overpotentials is a massive challenge in itself. Therefore this goal must be reached in the near future.

In this thesis, the challenges faced by a new researcher in the world of ECO_2RR are shown, and the processes undertaken to be able to create a basis for future ECO_2RR work. Therefore, future work to build upon this can consist of improvements in the three critical areas; analysis methods, cell design, and catalyst.

Before discussing the three critical areas of future work, it is worth noting that future work would also involve using different electrochemical methods. Differential Pulsed Voltammetry (DPV) was an area briefly explored, incorporating anodic pulses in the voltammetry to assist with electrode longevity. Theoretically, an anodic pulse can strip the electrode surface of contaminants, or any oxidation, allowing for surface chemistry and active sites to remain consistent.[70, 150, 152-154] A study of DPV (once the anodic pulse was optimised) vs LSV vs CA on a copper plate electrode using the on-line analytical methods was planned, however not conducted due to time constraints. In-tandem, a study was also planned to run the experimental conditions with on-line inductively coupled plasma – optical emission spectrometry (ICP-OES) to observe the electrolytic flow for metal dissolution when using these different techniques. It was hypothesised that the DPV technique would help catalytic performance, allowing essentially a 'clean slate' every so often for catalytic reactions, however the anodic and cathodic intervals would have to be carefully adjusted to ensure the desired results.

It was also hypothesised that the DPV technique would cause higher metal dissolution than the others. DPV, or any voltammetry or amperometry with an anodic pulse for the future, is an exciting avenue to explore. However, due to the challenges and time constraints, it is now future work.

Chapter 5 details the construction of an adaptable flow cell (AFC), and a dual-stage analysis setup for OLEMS analysis of ECO_2RR products. This setup is compared directly with a commercial DEMS cell. It was found that the faradaic efficiencies achieved were similar to the commercial cell, however the AFC was much more adaptable, and the dual-stage setup was easier to put together. This therefore questioned the need for such small cell designs, however the choice of design is understood due to the fact that it was manufactured for attachment directly to DEMS inlet. The dual-stage setup also give the freedom to place the AFC anywhere, however this comes at the cost of delay time between reaction and detection. To combat this, a MIMS probe which fits directly to the AFC was conceptualised, however did not come to fruition due to time constraints. Therefore, the development of this MIMS probe will prove advantageous, as it brings the DEMS inlet close to the electrode surface, removing any delay time whatsoever. Another advantage is that a flow system is not required, and this probe can be placed into static cells. Finally, the probe eradicates the need for the spacer, making this a single-stage setup.

Improvements to the AFC design may also be made. The current design uses a spacer to incorporate a reference electrode and a flow chamber for cathodic electrolyte. Minimising this space would bring the working and counter electrodes together, reducing the amount of resistance in between. Attempting to make this microfluidic may also be beneficial as product or bubble holdup may be eradicated, however due to incorporation of full sized Ag/AgCl, this may be difficult. Incorporation of an analytical probe may also constrain the size of this spacer. Regarding the user friendliness of the AFC, the stackable design allows for easy assembly, but a slight particular improvement could be made on screwing it together. The nuts were replaced with wingnuts for ease, however adding springs may allow the cell to be assembled with less likelihood of over-torquing and damaging.

The work presented in this thesis was conducted to build foundations in research for ECO_2RR, therefore further research into this using the cell designs and methods established, with the suggested tweaks, may allow for significant contributions into the ECO_2RR research community.

7 References

1. T. J. Crowley and R. A. Berner, *CO2 and Climate Change*, Science, 2001, **292**, 870-872.

2. W. Cramer, A. Bondeau, F. I. Woodward, I. C. Prentice, R. A. Betts, V. Brovkin, P. M. Cox, V. Fisher, J. A. Foley and A. D. Friend, *Global response of terrestrial ecosystem structure and function to CO2 and climate change: Results from six dynamic global vegetation models*, Global change biology, 2001, **7**, 357-373.

3. J. M. Melillo, A. D. McGuire, D. W. Kicklighter, B. Moore, C. J. Vorosmarty and A. L. Schloss, *Global climate change and terrestrial net primary production* Nature, 1993, **363**, 234-240.

4. J. Qiao, Y. Liu and J. Zhang, *Electrochemical reduction of carbon dioxide: fundamentals and technologies*, CRC Press, 2016.

5. U. Siegenthaler and J. Sarmiento, *Atmospheric carbon dioxide and the ocean. Nature*, 1993 365, 119–125

6. J. M. Hall-Spencer, R. Rodolfo-Metalpa, S. Martin, E. Ransome, M. Fine, S. M. Turner, S. J. Rowley, D. Tedesco and M.-C. Buia, *Nature*, 2008, **454**, 96.

7. J. W. Raich and C. S. Potter, *Global Biogeochemical Cycles*, 1995, **9**, 23-36.

8. M. Masiol and R. M. Harrison, *Atmospheric Environment*, 2014, **95**, 409-455.

9. H. Lindstad, B. E. Asbjørnslett and A. H. Strømman, *Energy Policy*, 2011, **39**, 3456-3464.

10. E. Uherek, T. Halenka, J. Borken-Kleefeld, Y. Balkanski, T. Berntsen, C. Borrego, M. Gauss, P. Hoor, K. Juda-Rezler, J. Lelieveld, D. Melas, K. Rypdal and S. Schmid, *Transport impacts on atmosphere and climate: Land transport*, 2009.

11. Ernst Worrell, Lynn Price, Nathan Martin, Chris Hendriks and L. O. Meida, *Annual Review of Energy and the Environment*, 2001, **26**, 303-329.

12. F. Marken and D. Fermin, *Electrochemical Reduction of Carbon Dioxide: Overcoming the Limitations of Photosynthesis*, Royal Society of Chemistry, 2018.

13. E. Dlugokencky and P. Tans, Trends in Atmospheric Carbon Dioxide, gml.noaa.gov/ccgg/trends/, 2021).

14. CO2.earth, 2100 Projections, https://www.co2.earth/2100-projections, Accessed Nov 2021).

15. Climate and Interactive, Climate Scoreboard - UN Climate Pledge Analysis, https://www.climateinteractive.org/programs/scoreboard/, Accessed Oct 2021).

16. M. Wang, A. Lawal, P. Stephenson, J. Sidders and C. Ramshaw, *Chemical Engineering Research and Design*, 2011, **89**, 1609-1624.

17. P. Lahijani, Z. A. Zainal, M. Mohammadi and A. R. Mohamed, *Renewable and Sustainable Energy Reviews*, 2015, **41**, 615-632.

18. M. Kanniche, R. Gros-Bonnivard, P. Jaud, J. Valle-Marcos, J.-M. Amann and C. Bouallou, *Applied Thermal Engineering*, 2010, **30**, 53-62.

19. P. Broutin, *The Oil and Gas Engineering Guide*, 2010, 111-112.

20. C. Song, in *CO₂ Conversion and Utilization*, American Chemical Society, 2002, vol. 809, ch. 1, pp. 2-30.

21. M. D. Porosoff, B. Yan and J. G. Chen, *Energy & Environmental Science*, 2016, **9**, 62-73.

22. M. Crocker, *Thermochemical Conversion of Biomass to Liquid Fuels and Chemicals*, RSC Publishing, 2010.

23. Y. Yamazaki, H. Takeda and O. Ishitani, *J. Photochem. and Photobio. C, Photochem. Rev.*, 2015, **25**, 106-137.

24. J.-M. Lehn and R. Ziessel, *Proceedings of the National Academy of Sciences*, 1982, **79**, 701-704.

25. T. W. Woolerton, S. Sheard, E. Reisner, E. Pierce, S. W. Ragsdale and F. A. Armstrong, *J. American Chem. Soc.*, 2010, **132**, 2132-2133.

26. E. Karamian and S. Sharifnia, *Journal of CO2 Utilization*, 2016, **16**, 194-203.

27. K. Li, X. An, K. H. Park, M. Khraisheh and J. Tang, *Catalysis Today*, 2014, **224**, 3-12.

28. B. Kumar, M. Llorente, J. Froehlich, T. Dang, A. Sathrum and C. P. Kubiak, *Annual Review of Physical Chemistry*, 2012, **63**, 541-569.

29. Z. Guo, S. Cheng, C. Cometto, E. Anxolabéhère-Mallart, S.-M. Ng, C.-C. Ko, G. Liu, L. Chen, M. Robert and T.-C. Lau, *J. American Chem. Soc.*, 2016, **138**, 9413-9416.

30. H. Takeda, K. Ohashi, A. Sekine and O. Ishitani, *J. American Chem. Soc.*, 2016, **138**, 4354-4357.

31. L. Wang, X. Zhang, L. Yang, C. Wang and H. Wang, *Catalysis Science & Technology*, 2015, **5**, 4800-4805.

32. H. Narayanan, B. Viswanathan and S. Yesodharan, *Photocatalytic Reduction of Carbon Dioxide: Issues and Prospects*, National Centre for Catalysis Research, Indian Institute of Technology Madras, Chennai-600036, India.

33. S. Lee and J. Lee, *ChemSusChem*, 2016, **9**, 333-344.

34. T. Pardal, T. Fernandes, A. Machado and C. Rangel, *Structural Features of Electrodeposited Copper Electrodes for CO2 Conversion*, Materials Science Forum, 2013 239-244.

35. T. E. Teeter and P. V. Rysselberghe, *The Journal of Chemical Physics*, 1954, **22**, 759-760.

36. Y. Hori, K. Kikuchi and S. Suzuki, *Chem. Lett.*, 1985, 1695-1698.

37. K. W. Frese and S. Leach, *J. Electrochem. Soc.*, 1985, **132**, 259-260.

38. R. Kortlever, J. Shen, K. J. P. Schouten, F. Calle-Vallejo and M. T. Koper, *The journal of physical chemistry letters*, 2015, **6**, 4073-4082.

39. J. Tang, X. Zou and F. Hong, in *Electrochemical Reduction of Carbon Dioxide Fundamentals and Technologies*, eds. J. Qiao, Y. Liu and J. Zhang, CRC Press Taylor & Francis Group, 2016, vol. 1, pp. 293-304.

40. Q. Lu, J. Rosen, Y. Zhou, G. S. Hutchings, Y. C. Kimmel, J. G. Chen and F. Jiao, *Nat. Commun.*, 2014, **5**, 4242-4246.

41. Y. Hori, K. Kikuchi and S. Suzuki, *Chemistry Letters*, 1985, **14**, 1695-1698.

42. Y. Hori, A. Murata, S.-y. Ito, Y. Yoshinami and O. Koga, *Chemistry Letters*, 1989, **18**, 1567-1570.

43. Y. Hori, A. Murata and R. Takahashi, *Journal of the Chemical Society, Faraday Transactions 1: Physical Chemistry in Condensed Phases*, 1989, **85**, 2309-2326.

44. S. Nitopi, E. Bertheussen, S. B. Scott, X. Liu, A. K. Engstfeld, S. Horch, B. Seger, I. E. L. Stephens, K. Chan, C. Hahn, J. K. Nørskov, T. F. Jaramillo and I. Chorkendorff, *Chemical Reviews*, 2019, **119**, 7610-7672.

45. Y. Hori, in *Modern Aspects of Electrochemistry*, eds. C. G. Vayenas, R. E. White and M. E. Gamboa-Aldeco, Springer New York, New York, NY, 2008, DOI: 10.1007/978-0-387-49489-0_3, pp. 89-189.

46. A. Bagger, W. Ju, A. S. Varela, P. Strasser and J. Rossmeisl, *ChemPhysChem*, 2017, **18**, 3266-3273.

47. K. P. Kuhl, E. R. Cave, D. N. Abram and T. F. Jaramillo, *Energy & Environmental Science*, 2012, **5**, 7050-7059.

48. J. Zhao, S. Xue, J. Barber, Y. Zhou, J. Meng and X. Ke, *Journal of Materials Chemistry A*, 2020, **8**, 4700-4734.

49. D. Cheng, F. R. Negreiros, E. Aprà and A. Fortunelli, *ChemSusChem*, 2013, **6**, 944-965.

50. J. Rosen, G. S. Hutchings, Q. Lu, S. Rivera, Y. Zhou, D. G. Vlachos and F. Jiao, *Acs Catalysis*, 2015, **5**, 4293-4299.

51. J. Shen, M. J. Kolb, A. J. Gottle and M. T. Koper, *The Journal of Physical Chemistry C*, 2016, **120**, 15714-15721.

52. H. Li and K. Reuter, *Active-Site Computational Screening: Role of Structural and Compositional Diversity for the Electrochemical CO2 Reduction at Mo Carbide Catalysts* ACS catalysis, 2020, **10**, 11814-11821.

53. R. G. Compton and C. E. Banks, *Understanding Voltammetry*, 2018.

54. A. J. Bard and L. R. Faulkner, *Electrochemical methods*, 2001, **2**, 580-632.

55. K. Izutsu, *Electrochemistry in nonaqueous solutions*, John Wiley & Sons, **2** 2009.

56. C.-y. Liu, S. R. Snyder and A. J. Bard, *The Journal of Physical Chemistry B*, 1997, **101**, 1180-1185.

57. S. Kaneco, K. Iiba, H. Katsumata, T. Suzuki and K. Ohta, *Journal of Solid State Electrochemistry*, 2007, **11**, 490-495.

58. J. Tang, X. Zou and F. Hong, in *Electrochemical Reduction of Carbon Dioxide - Fundamentals and Technologies*, eds. J. Qiao, Y. Liu and J. Zhang, CRC Press Taylor & Francis Group, 2016, vol. 1, pp. 293-304.

59. Y. Chen and D. Sun, in *Electrochemical Reduction of Carbon Dioxide*, eds. Q. Jinli, L. Yuyu and Z. Jiujun, CRC Press, 2016, DOI: 10.1201/b20177-6, ch. Electrochemical Methods for CO Electroreduction.

60. K. J. P. Schouten, E. Pérez Gallent and M. T. M. Koper, *ACS Catalysis*, 2013, **3**, 1292-1295.

61. R. Kas, R. Kortlever, A. Milbrat, M. T. M. Koper, G. Mul and J. Baltrusaitis, *Physical Chemistry Chemical Physics*, 2014, **16**, 12194-12201.

62. H. Hashiba, S. Yotsuhashi, M. Deguchi and Y. Yamada, *ACS Combinatorial Science*, 2016, **18**, 203-208.

63. X. Li, W. Bi, M. Chen, Y. Sun, H. Ju, W. Yan, J. Zhu, X. Wu, W. Chu, C. Wu and Y. Xie, *Journal of the American Chemical Society*, 2017, **139**, 14889-14892.

64. J. S. Derrick, M. Loipersberger, R. Chatterjee, D. A. Iovan, P. T. Smith, K. Chakarawet, J. Yano, J. R. Long, M. Head-Gordon and C. J. Chang, *Journal of the American Chemical Society*, 2020, **142**, 20489-20501.

65. A. V. Rayer, E. Reid, A. Kataria, I. Luz, S. J. Thompson, M. Lail, J. Zhou and M. Soukri, *Journal of CO2 Utilization*, 2020, **39**, 101159.

66. M. Zhao, H. Tang, Q. Yang, Y. Gu, H. Zhu, S. Yan and Z. Zou, *ACS Applied Materials & Interfaces*, 2020, **12**, 4565-4571.

67. X.-G. Zhang, Y. Murakami, K. Yahikozawa and Y. Takasu, *Electrochimica Acta*, 1997, **42**, 223-227.

68. R. Zhang, W. Lv, G. Li, M. Mezaal and L. Lei, *RSC Advances*, 2015, **5**, 68662-68667

69. N. Qiao and J. Zheng, *Microchimica Acta*, 2012, **177**, 103-109.

70. R. Shiratsuchi, Y. Aikoh and G. J. J. o. T. E. S. Nogami, 1993, **140**, 3479-3482.

71. W. Guo, K. Shim and Y.-T. Kim, *Applied Surface Science*, 2020, **526**, 146651.

72. P. Deng, H. Wang, R. Qi, J. Zhu, S. Chen, F. Yang, L. Zhou, K. Qi, H. Liu and B. Y. Xia, *ACS Catalysis*, 2020, **10**, 743-750.

73. T.-C. Chou, C.-C. Chang, H.-L. Yu, W.-Y. Yu, C.-L. Dong, J.-J. Velasco-Vélez, C.-H. Chuang, L.-C. Chen, J.-F. Lee, J.-M. Chen and H.-L. Wu, *Journal of the American Chemical Society*, 2020, **142**, 2857-2867.

74. Y. Gang, F. Pan, Y. Fei, Z. Du, Y. H. Hu and Y. Li, *ACS Sustainable Chemistry & Engineering*, 2020, DOI: 10.1021/acssuschemeng.0c03054.

75. S. Chandrashekar, N. T. Nesbitt and W. A. Smith, *The Journal of Physical Chemistry C*, 2020, DOI: 10.1021/acs.jpcc.0c01894.

76. S. Garg, M. Li, T. E. Rufford, L. Ge, V. Rudolph, R. Knibbe, M. Konarova and G. G. X. Wang, 2020, **13**, 304-311.

77. J. Huang, M. Mensi, E. Oveisi, V. Mantella and R. Buonsanti, *Journal of the American Chemical Society*, 2019, **141**, 2490-2499.

78. J. Kim, W. Choi, J. W. Park, C. Kim, M. Kim and H. Song, *Journal of the American Chemical Society*, 2019, **141**, 6986-6994.

79. K. Jiang, R. B. Sandberg, A. J. Akey, X. Liu, D. C. Bell, J. K. Nørskov, K. Chan and H. Wang, *Nature Catalysis*, 2018, **1**, 111-119.

80. S. Sen, D. Liu and G. T. R. Palmore, *ACS Catalysis*, 2014, **4**, 3091-3095.

81. L. Sun, G. K. Ramesha, P. V. Kamat and J. F. Brennecke, *Langmuir*, 2014, **30**, 6302-6308.

82. Q. Lu, J. Rosen, Y. Zhou, G. S. Hutchings, Y. C. Kimmel, J. G. Chen and F. Jiao, *Nature Communications*, 2014, **5**, 3242.

83. C. W. Li, J. Ciston and M. W. Kanan, *Nature*, 2014, **508**, 504-507.

84. D. M. Weekes, D. A. Salvatore, A. Reyes, A. Huang and C. P. Berlinguette, *Accounts of Chemical Research*, 2018, **51**, 910-918.

85. S. Liang, N. Altaf, L. Huang, Y. Gao and Q. Wang, *Journal of CO2 Utilization*, 2020, **35**, 90-105.

86. D. Higgins, C. Hahn, C. Xiang, T. F. Jaramillo and A. Z. Weber, *ACS Energy Letters*, 2019, **4**, 317-324.

87. K. Liu, W. A. Smith and T. Burdyny, *ACS Energy Letters*, 2019, **4**, 639-643.

88. H. Rabiee, L. Ge, X. Zhang, S. Hu, M. Li and Z. Yuan, *Energy & Environmental Science*, 2021, **14**, 1959-2008.

89. J. Hong, W. Zhang, J. Ren and R. Xu, *Analytical Methods*, 2013, **5**, 1086-1097.

90. M. Gattrell, N. Gupta and A. Co, *Journal of Electroanalytical Chemistry*, 2006, **594**, 1-19.

91. A. J. Bard and L. R. Faulkner, *Electrochemical Methods: Fundamentals and Applications*, 1980.

92. Gas Chromatography, http://chem.libretexts.org/Core/Analytical_Chemistry/Instrumental_Analysis/Chromatography/Gas_Chromatography, (accessed December, 2018).

93. Gas Chromatography Theory, http://www.chem.ucla.edu/~bacher/General/30BL/gc/theory.html, (accessed December, 2018).

94. M. Antoniadou, G. A. Zachariadis and E. Rosenberg, *Analytical Letters*, 2019, **52**, 2822-2839.

95. Z. Liu, Z. Zhu, Q. Wu, S. Hu and H. Zheng, *Analyst*, 2011, **136**, 4539-4544.

96. R. Gras, J. Luong, M. Monagle and B. Winniford, *Journal of Chromatographic Science*, 2006, **44**, 101-107.

97. X. Jiang, Y. Chen, C. Zheng and X. Hou, *Analytical Chemistry*, 2014, **86**, 5220-5224.

98. K. Shinada, S. Horiike, S. Uchiyama, R. Takechi and T. Nishimoto, *Shimadzu Hyoron*, 2012, **69**, 255-263.

99. S. Iguchi, K. Teramura, S. Hosokawa and T. Tanaka, *Physical Chemistry Chemical Physics*, 2015, **17**, 17995-18003.

100. J. Qiao, Y. Liu, F. Hong and J. Zhang, *Chemical Society Reviews*, 2014, **43**, 631-675.

101. Y. Hori, K. Kikuchi, A. Murata and S. Suzuki, *Chem. Lett.*, 1986, **6**, 897-898.

102. What is NMR?, http://chem.ch.huji.ac.il/nmr/whatisnmr/whatisnmr.html, (accessed December, 2016).

103. NMR: Introduction, http://chem.libretexts.org/Core/Physical_and_Theoretical_Chemistry/Spectroscopy/Magnetic_Resonance_Spectroscopies/Nuclear_Magnetic_Resonance/Nuclear_Magnetic_Resonance_II, (accessed December, 2016).

104. S. Fregert, I. Dahlquist and B. Gruvberger, *Contact Dermatitis*, 1984, **10**, 132-134.

105. M. Gryllaki-Berger, C. H. Mugny, D. Perrenoud, A. Pannather and E. Frenk, *Contact Dermatitis*, 1992, **26**, 149-154.

106. T. Shimomura, T. Itoh, T. Sumiya, F. Mizukami and M. Ono, *Sensors and Actuators B: Chemical*, 2008, **135**, 268-275.

107. R. G. Liteplo, R. Beauchamp, M. E. Meek and R. Chénier, *Formaldehyde*, Report CICAD 40 World Health Organization, Geneva, 2002.

108. Agency for Toxic Substances and Disease and Registry, *Journal*, 1999. https://doi.org/10.1177/074823379901500809

109. A. Mavropoulos; and D. Newman, Wasted Health: The Tragic Case of. Dumpsites, *International Solid Waste Association (ISWA)*, 2015, 40.

110. J. Hong, W. Zhang, J. Ren and R. Xu, *Analytical methods*, 2013, **5**, 1086-1097.

111. A. Corma and H. Garcia, *Journal of Catalysis*, 2013, **308**, 168-175.

112. P. Russell, N. Kovac, S. Srinivasan and M. Steinberg, *Journal of the Electrochemical Society*, 1977, **124**, 1329-1338.

113. U. S. EPA, Sampling For Selected Aldehyde And Ketone Emissions From Stationary Sources, 1996, 11.

114. Y.-L. Lin, P.-Y. Wang, L.-L. Hsieh, K.-H. Ku, Y.-T. Yeh and C.-H. Wu, *Journal of Chromatography A*, 2009, **1216**, 6377-6381.

115. T. Nash, *Biochemical Journal*, 1953, **55**, 416-421.

116. Z.-L. Zhou, T.-F. Kang, Y. Zhang and S.-Y. Cheng, *Microchimica Acta*, 2009, **164**, 133-138.

117. G.-P. Jin, J. Li and X. Peng, *J. Appl. Electrochem.*, 2009, **39**, 1889-1895.

118. Y. Zhang, M. Zhang, Z. Cai, M. Chen and F. Cheng, *Electrochimica Acta*, 2012, **68**, 172-177.

119. J. P. Metters, F. Tan and C. E. Banks, *Journal of Solid State Electrochemistry*, 2013, **17**, 1553-1562.

120. Q. Yi, F. Niu and W. Yu, *Thin Solid Films*, 2011, **519**, 3155-3161.

121. A. Safavi, N. Maleki, F. Farjami and E. Farjami, *J. Electroanal. Chem.*, 2009, **626**, 75-79.

122. M. R. Baez-Gaxiola, C. Fernandez-Sanchez and E. Mendoza, *Analytical Methods*, 2015, **7**, 538-542.

123. K. E. Toghill, L. Xiao, N. R. Stradiotto and R. G. Compton, *Electroanalysis*, 2010, **22**, 491-500.

124. N. R. Stradiotto, K. E. Toghill, L. Xiao, A. Moshar and R. G. Compton, *Electroanalysis*, 2009, **21**, 2627-2633.

125. J. C. Harfield, K. E. Toghill, C. Batchelor-McAuley, C. Downing and R. G. Compton, *Electroanalysis*, 2011, **23**, 931-938.

126. K. E. Toghill, L. Xiao, M. A. Phillips and R. G. Compton, *Sensors and Actuators B: Chemical*, 2010, **147**, 642-652.

127. H. Nie, Z. Yao, X. Zhou, Z. Yang and S. Huang, *Biosensors and Bioelectronics*, 2011, **30**, 28-34.

128. M. Shamsipur, M. Najafi and M.-R. M. Hosseini, *Bioelectrochemistry*, 2010, **77**, 120-124.

129. F. Miao and B. Tao, *J. Nanosci. Nanotechnol.*, 2013, **13**, 3104-3109.

130. R. Ojani, J. B. Raoof and S. R. H. Zavvarmahalleh, *J. Solid State Electrochem.*, 2009, **13**, 1605-1611.

131. Y. Yu, W. Su, M. Yuan, Y. Fu and J. Hu, *J. Power Sources*, 2015, **286**, 130-135.

132. S. N. Azizi, S. Ghasemi and F. Amiripour, *Sens. Actuators, B*, 2016, **227**, 1-10.

133. J.W. Eichelberger, Determination Of Carbonyl Compounds In Drinking Water By Dinitrophenylhydrazine Derivatization And Highperformance Liquid Chromatography, *U. S. EPA*, 1992, 554.

134. V. Thomsen, D. Schatzlein and D. Mercuro, *Spectroscopy*, 2003, **18**, 112-114.

135. R. Martin, *Australian Journal of Chemistry*, 1954, **7**, 335-347.

136. S. Bruckenstein and R. R. Gadde, *J. American Chem. Soc.*, 1971, **93**, 793-794.

137. O. Wolter and J. Heitbaum, *Berichte der Bunsengesellschaft für physikalische Chemie*, 1984, **88**, 2-6.

138. A. Abd-El-Latif, C. J. Bondue, S. Ernst, M. Hegemann, J. Kaul, M. Khodayari, E. Mostafa, A. Stefanova and H. Baltruschat, *Insights into electrochemical reactions by differential electrochemical mass spectrometry*, 2015.

139. H. Baltruschat, *Journal of the American Society for Mass Spectrometry*, 2004, **15**, 1693-1706.

140. S. J. Ashton, *Design, Construction and Research Application of a Differential Electrochemical Mass Spectrometer (DEMS)*, Springer Berlin Heidelberg, 2012.

141. M. Duca, M. O. Cucarella, P. Rodriguez and M. T. M. Koper, *Journal of the American Chemical Society*, 2010, **132**, 18042-18044.

142. E. Evenstein, Rosy, S. Haber, H. Sclar, L. Houben, K. Leung, M. Leskes and M. Noked, *Energy Storage Materials*, 2019, **19**, 261-269.

143. Rosy, S. Akabayov, M. Leskes and M. Noked, *ACS Applied Materials & Interfaces*, 2018, **10**, 29622-29629.

144. W. Chen, N. Uwitonze, F. He, M. M. Sartin, J. Cai and Y.-X. Chen, *Journal of Energy Chemistry*, 2021, **56**, 412-419.

145. T. Hartung and H. Baltruschat, *Langmuir*, 1990, **6**, 953-957.

146. C. J. Bondue and M. T. M. Koper, *Journal of Electroanalytical Chemistry*, 2020, DOI: https://doi.org/10.1016/j.jelechem.2020.113842, 113842.

147. E. L. Clark, M. R. Singh, Y. Kwon and A. T. Bell, *Analytical Chemistry*, 2015, **87**, 8013-8020.

148. M. E. Leonard, L. E. Clarke, A. Forner-Cuenca, S. M. Brown and F. R. Brushett, *ChemSusChem*, 2020, **13**, 400-411.

149. S. Sen, S. M. Brown, M. Leonard and F. R. Brushett, *Journal of Applied Electrochemistry*, 2019, **49**, 917-928.

150. S. Sen, B. Skinn, T. Hall, M. Inman, E. J. Taylor and F. R. Brushett, *MRS Advances*, 2017, **2**, 451-458.

151. B. Endrődi, G. Bencsik, F. Darvas, R. Jones, K. Rajeshwar and C. Janáky, *Progress in Energy and Combustion Science*, 2017, **62**, 133-154.

152. A. Engelbrecht, C. Uhlig, O. Stark, M. Hämmerle, G. Schmid, E. Magori, K. Wiesner-Fleischer, M. Fleischer and R. Moos, 2018, **165**, J3059-J3068.

153. S. Ishimaru, R. Shiratsuchi and G. J. J. o. T. E. S. Nogami, 2000, **147**, 1864-1867.

154. C. S. Le Duff, M. J. Lawrence and P. Rodriguez, 2017, **56**, 12919-12924.

8 Appendices

Appendix A: Analysis Methods..... 135

Appendix B: Cell Design 143

Appendix A: Analysis Methods

Ion Chromatography

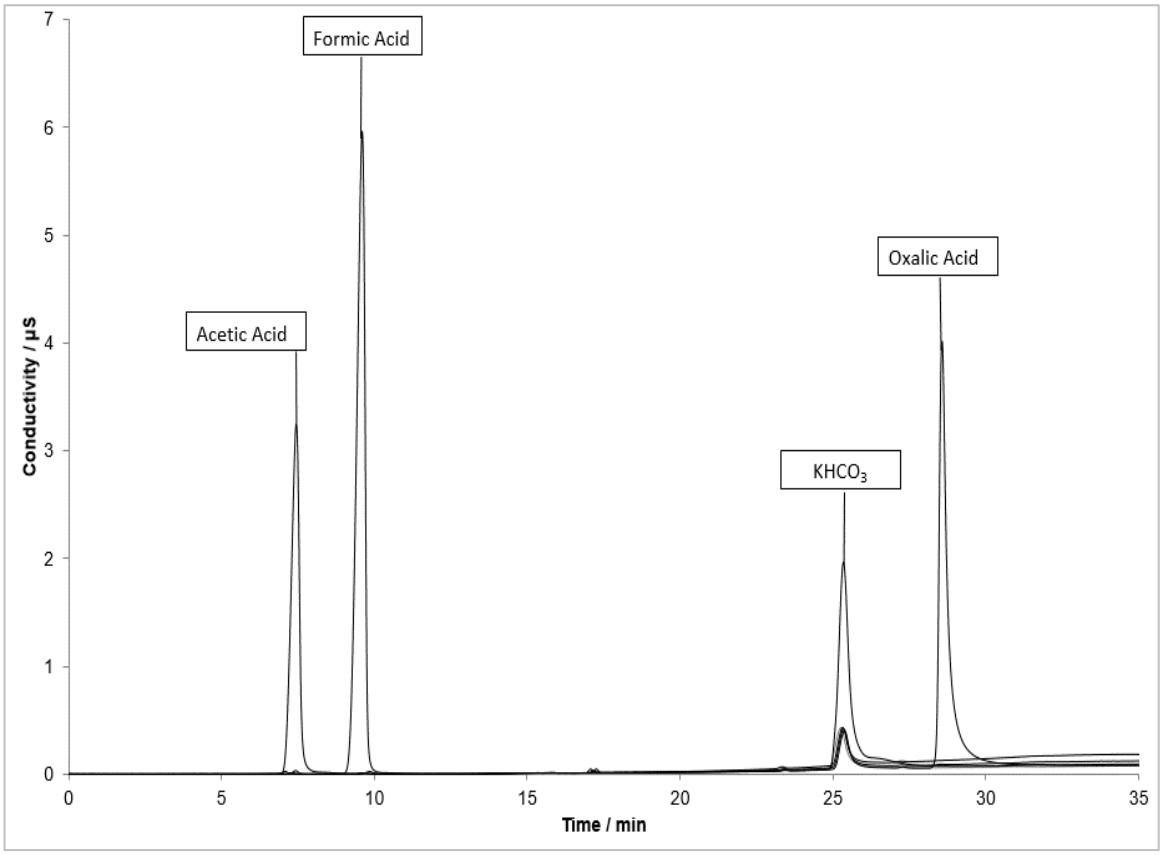

Figure 6.2.1 Ion Chromatography results of the mixed solution after the ramping method was applied

1 to 30 mM Gradient Elution (KOH), 29 mA suppression, 0.38 mL/min flow, 60 minutes run time

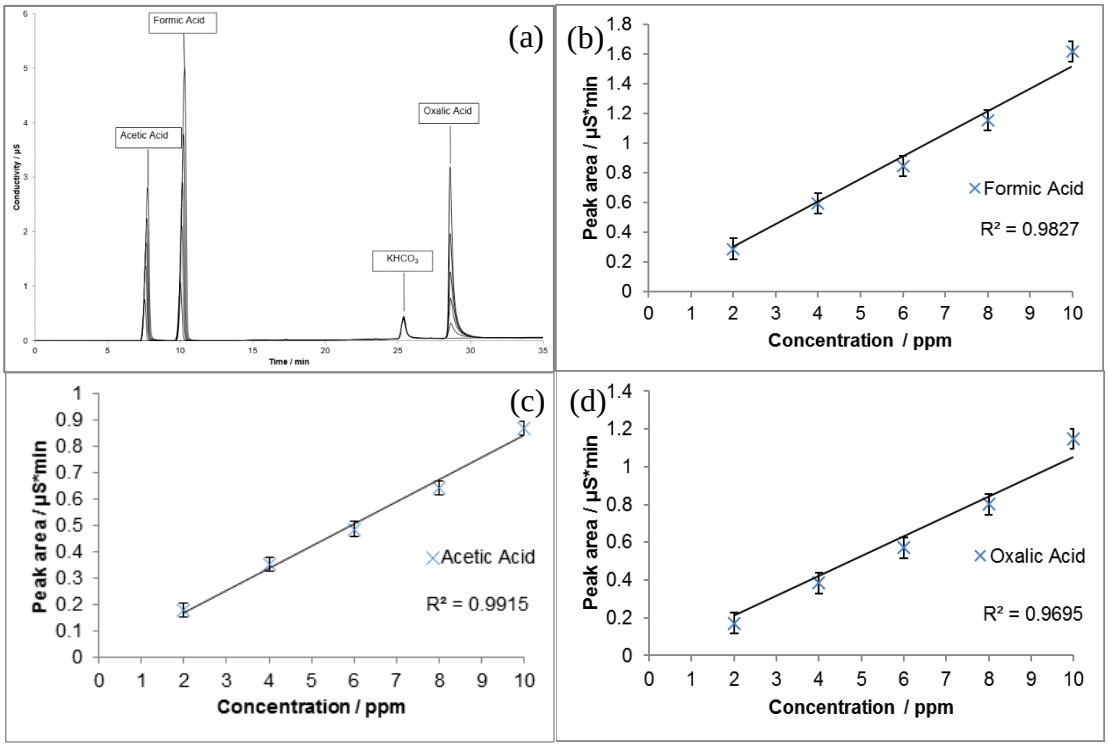

Figure 6.2.2 - Overlaid results of 0 to 10 ppm solutions of acetic, formic and oxalic acid (increments of 2 ppm) (a) and the corresponding calibration plots for (b) formic acid (c) acetic acid (d) oxalic acid

Table 6.2.1 Ion Chromatography limit of detection at the lower concentration range

Acid	Limit of Detection (ppm)
Acetic	1.106
Formic	1.422
Oxalic	1.526

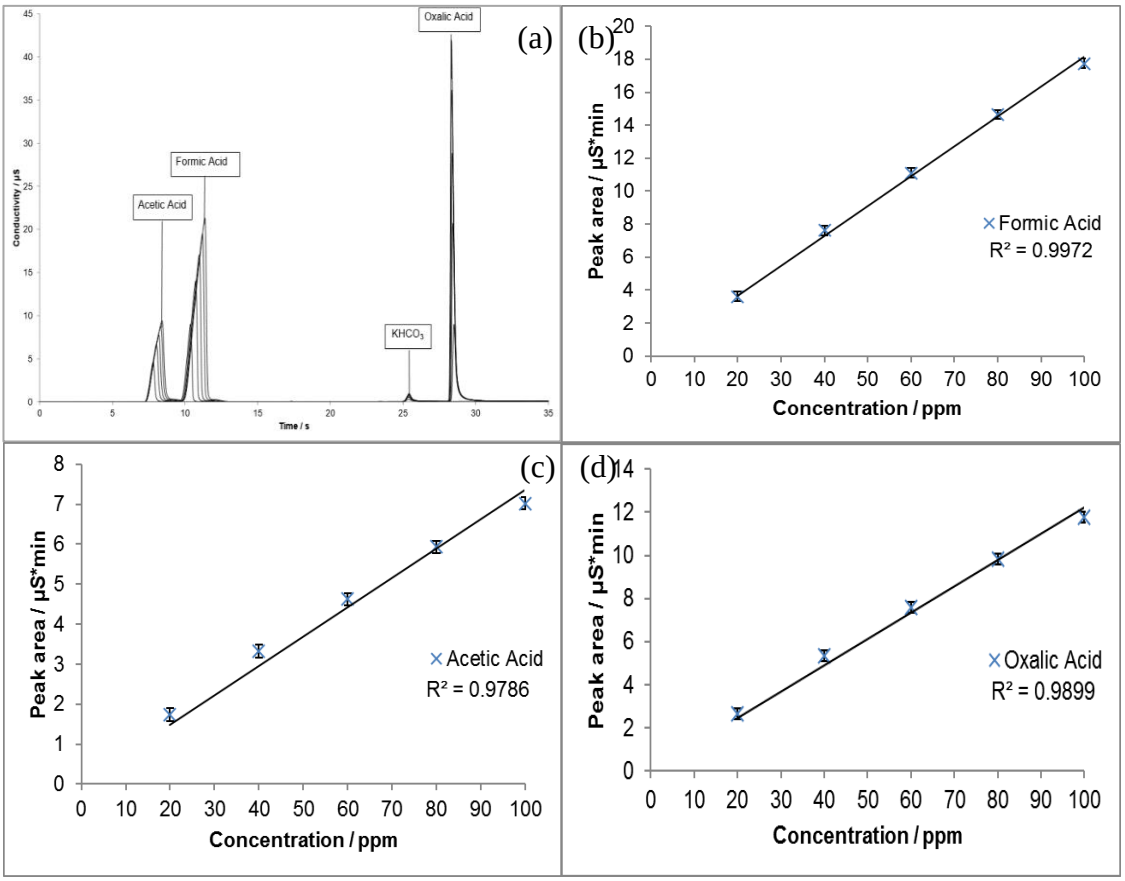

Figure 6.2.3 – Overlaid Ion Chromatography results of 20 to 100 ppm solutions of acetic, formic and oxalic acid (increments of 20 ppm) (a) and the corresponding calibration plots for (b) formic acid (c) acetic acid (d) oxalic acid

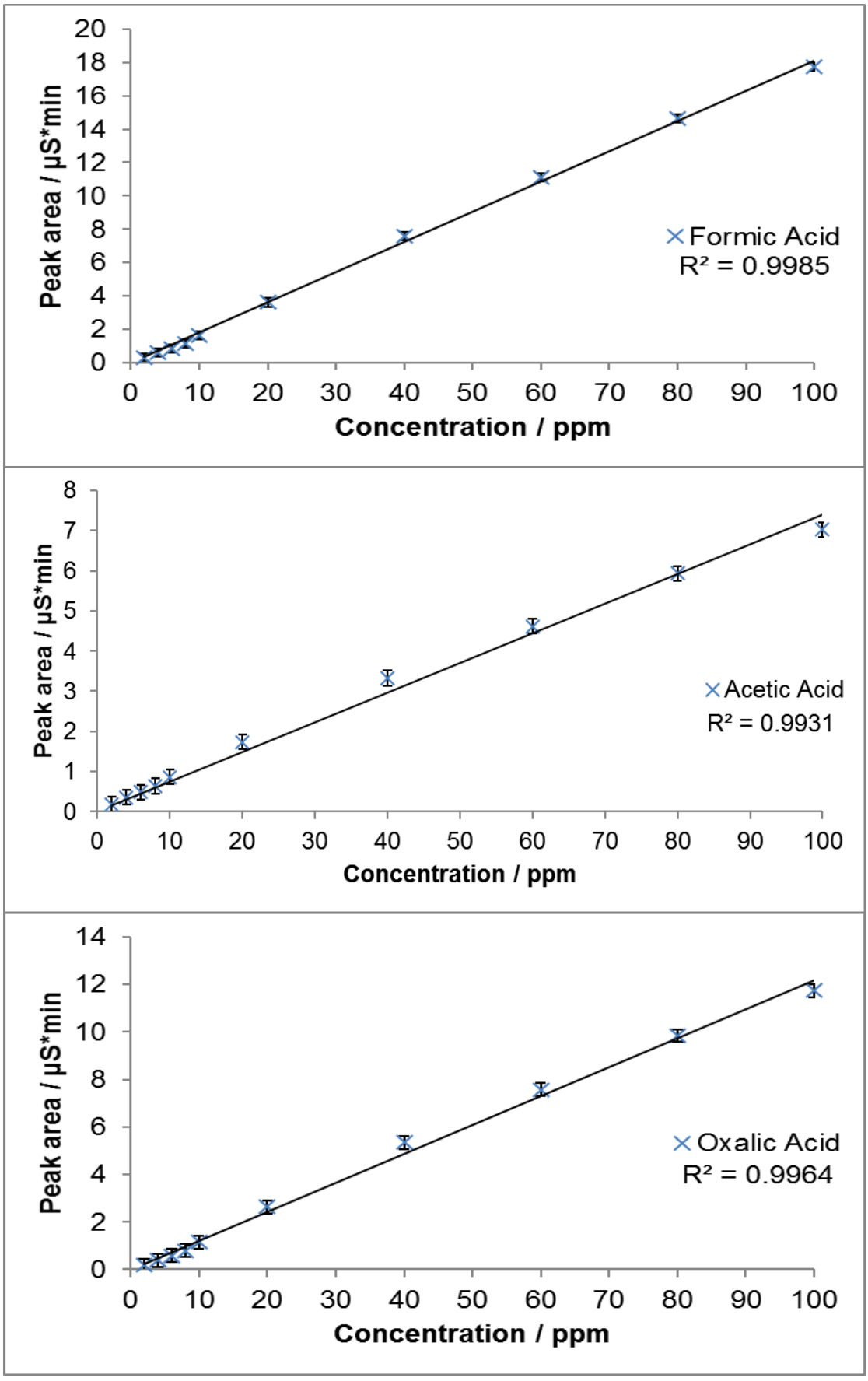

Figure 6.2.4 - Full Range IC calibration plots for all acids.

NMR

Omission of Formaldehyde

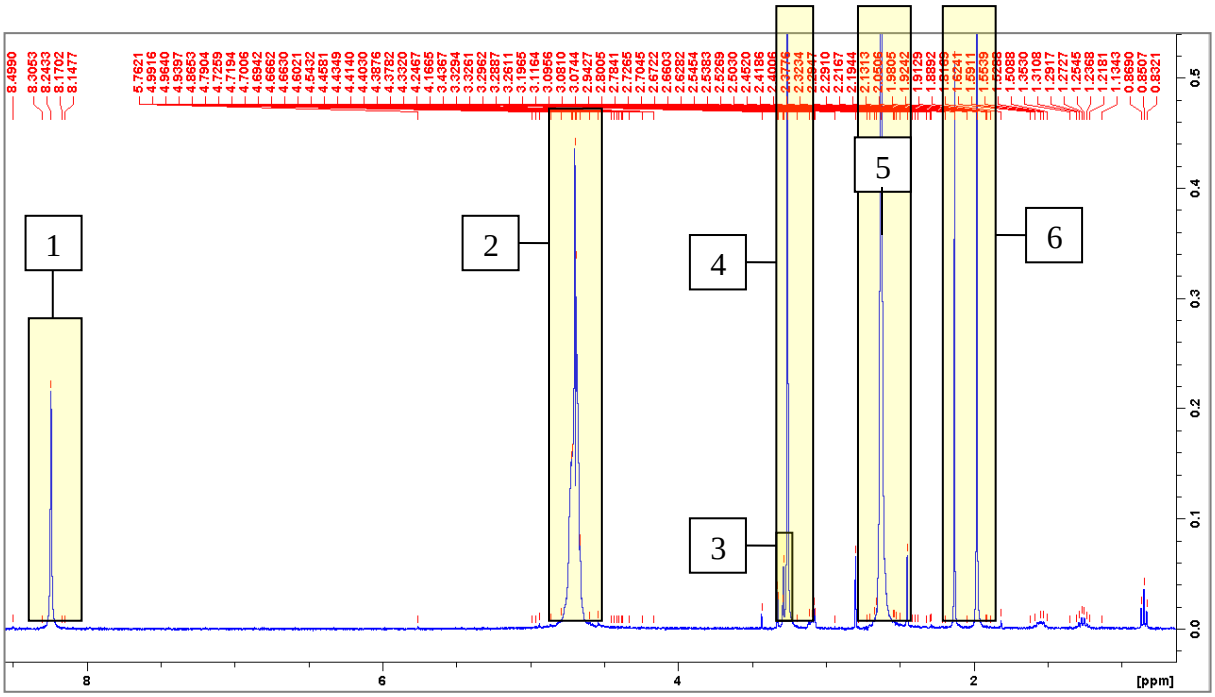

Figure 6.2.5 H^1NMR (H_2O + D_2O 90:10, 400MHz): δ 8.24 (1. formic acid / formaldehyde), δ 4.70 (2. methanol / $KHCO_3$ -OH), δ 3.28 (3. formaldehyde), δ 3.26 (4. methanol), δ 2.62 (5. DMSO), δ 1.98 (6. acetic acid).

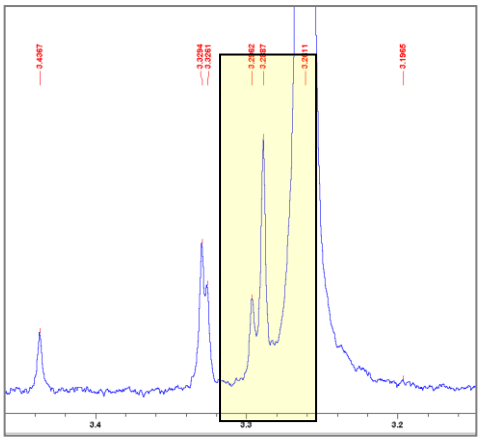

Figure 6.2.6 Methanol peak with interfering formaldehyde peak

Deciding on D1 and NS values

Along with the T_1 analysis, further general suppression analysis was conducted upon the 60 ppm sample. This consisted of altering D1 and NS values in a manner which deliver results in a decent period of time, with the best signal to noise ratio. A total of 7 were carried out at the following D1 and NS values;

Table 6.2.2 - D1 and NS values tested for NMR

D1	NS
1	64
2	54
3	46
4	40
5	36
10	22
15	16

The D1 represents a 'Recycle Delay' - this appears at the beginning of a pulse sequence. This delay time allows the nuclear spins to return to equilibrium. Not allowing enough time for relaxation can cause inaccuracies in the peaks displayed, as they have not had enough time to return to equilibrium before another pulse has been applied. The NS represents the number of scans that can occur after the recycle delay within the time period set. The set time period for each acquisition was approximately 8 minutes. In this test however, it had been neglected that the NS needs to be a multiple of 8 to be able to finish a complete cycle, therefore the results obtained for NS's which were not a multiple of 8 consisted of errors.

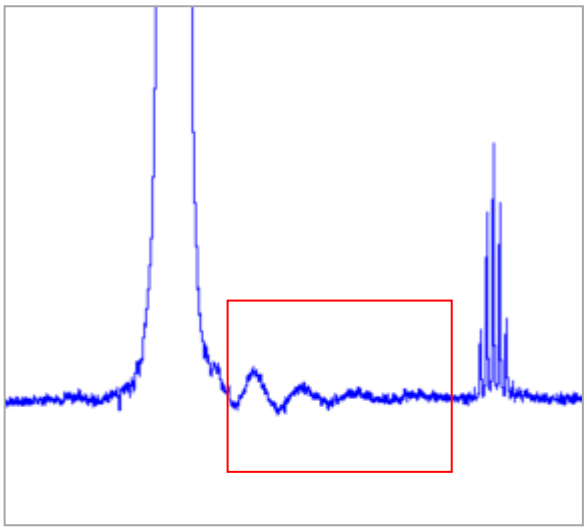

Figure 6.2.7 Error due to NS - incomplete cycle

GC-BID

Table 6.2.3 - GC-BID Parameters

SPL Temperature	250°C
Carrier Gas	He
Flow Control	Linear Velocity
Pressure	144.7 kPa
Total Flow	57.0 ml/min
Column Flow	2.08 ml/min
Linear Velocity	40.0 cm/s
Purge Flow	3.0 ml/min
Split Ratio	25
Column	ShinCarbon micropacked column ST 80/100, 2m, 0.53 mm ID, 0.74 mm OD, Thames Restek UK
Temperature Range and Hold Time	40°C, 5 minutes, 200°C, 3 minutes,
Ramp Rate	25
BID Temperature	250°C
BID Sampling Rate	40 ms
Discharge Gas and Flow	He, 50 ml/min
BID Column Pressure	300.0 kPA

Appendix B: Cell Design

RESIN PRINTER SETTINGS

Table 6.2.4 - Anycubic Photon Resin Printer Settings

Printer	**Anycubic Photon**
CAD Software	Autodesk Fusion360
Slicer	ChiTuBox 64
Resin	Anycubic Clear Methacrylate based
Layer Height (µm)	50
Bottom Layer Count	3
Exposure Time (s)	8
Bottom Exposure Time (s)	30
Lift Distance (mm)	5
Lifting Speed (mm/min)	65
Retract Speed (mm/min)	150
Anti-Aliasing Level	4